DIFFRACTION IN ALICE AND TRIGGER EFFICIENCIES.

by

SPARSH NAVIN

A thesis submitted to

The University of Birmingham

for the degree of

DOCTOR OF PHILOSOPHY

Supervisors:

Cristina Lazzeroni

Roman Lietava

Particle Physics Group

School of Physics and Astronomy

The University of Birmingham

July, 2011

Abstract

ALICE is built to measure the properties of strongly interacting matter created in heavy-ion collisions. In addition, taking advantage of the low p_T acceptance in the central barrel, ALICE is playing an important role in understanding pp collisions with minimum bias triggers at LHC energies. The work presented in this thesis is based on pp data simulated by the ALICE collaboration and early data collected at a center-of-mass energy of 7 TeV.

A procedure to calculate trigger efficiencies and an estimate of the systematic uncertainty due to the limited acceptance of the detector are shown. A kinematic comparison between Monte Carlo event generators, PYTHIA 6, PYTHIA 8 and PHOJET is also presented. To improve the description of diffraction in PYTHIA, a hard diffractive component was added to PYTHIA 8 in 2009, which is described. Finally a trigger with a high efficiency for picking diffractive events is used to select a sample with an enhanced diffractive component from pp data. These data are compared to Monte Carlo models, and the results are summarized with an estimate of the systematic uncertainty.

This thesis is dedicated to the most important people in my life

- Momma, Poppa, Patty and Mano.

Acknowledgments

The first two people I should thank are my supervisors, Roman Lietava and Cristina Lazzeroni, who have helped me with work and otherwise over the last 4 years. Without the two of you, I would not have come this far and finished my thesis. Then, I should thank my supervisor in Lund for 4 months, Torbjörn Sjöstrand, who spent many hours teaching me everything I know about PYTHIA.

I have learnt a lot about physics and work from the three of you.

I would like to thank David, Lee, Peter, Gron, Anju, Anton, Pedja and Marian for help with various things like coding, proof-reading and understanding the ALICE trigger. I would like to make a special mention of Orlando who has read many versions of my thesis at very short notice, and Marek who is always willing to help.

Others at Birmingham who have helped me are Pete, both Pauls, Nigel, Chris, Norma, Maria and Anna. Paul Newman has answered my many questions on diffraction and provided a PDF set included in PYTHIA 8. I definitely cannot forget Lawrie, who has always helped solve computing issues with a smile. For keeping me sane and some good humour, thanks to everyone I've shared office space with especially Plamen, Arvinder, Ravjeet, Zoe, Angela, Chris, Tim, Dave, Owen, Patrick and Dan. Plamen, thanks for the many installations of AliROOT. I also thank everyone who danced and played badminton with me.

Contents

List of Figures

List of Tables

Acronyms

ACORDE	Alice COsmic Ray DEtector
ALICE	A Large Ion Collider Experiment
ATLAS	A Toroidal Lhc ApparatuS
BG	Beam Gas
CDF	Collider Detector at Fermilab
CD	Central Diffraction (or Diffractive)
CERN	Conseil Européen pour la Recherche Nucléaire
	(known as 'European organisation for nuclear research' today)
CM	Centre-of-Mass
CMS	Compact Muon Solenoid
CP	Charge conjugation and Parity
CTP	Central Trigger Processor
DAQ	Data AcQuisition
DD	Double Diffraction (or Diffractive)
EMCAL	Electro Magnetic CALorimeter
FMD	Forward Multiplicity Detector
FsR	Final State Radiation
GFO	Global Fast-Or
HLT	High Level Trigger
HMPID	High Momentum PID
ISR	Intersecting Storage Rings
IsR	Initial State Radiation
ITS	Inner Tracking System
L(0,1,2)	Level (0,1,2)
LEP	Large Electron-Positron collider
LEIR	Low Energy Ions Ring
LHC	Large Hadron Collider
LHCb	LHC beauty

MB	Minimum Bias
MI	Multiple Interactions
MC	Monte Carlo
NDF	Number of Degrees of Freedom
NSD	Non-Single Diffractive
Pb-Pb	lead-lead
PHOS	PHOton Spectrometer
PID	Particle IDentification
PMD	Photon Multiplicity Detector
pp	proton-proton
p-value	probability value
RF	Radio Frequency
RHIC	Relativistic Heavy-Ion Collider
SD	Single Diffraction (or Diffractive)
SDD	Silicon Drift Detector
SPD	Silicon Pixel Detector
SSD	Silicon Strip Detector
STAR	Solenoid Tracker At the RHIC
T0	Time 0
TOF	Time Of Flight
TPC	Time Projection Chamber
TRD	Transition Radiation Detector
UA(1,5)	Underground Area (1,5)
V0	Vertex 0
ZDC	Zero Degree Calorimeter

INTRODUCTION

The LHC (Large Hadron Collider) [1] is currently the world's largest and most energetic particle accelerator, colliding beams of protons or lead ions. ALICE (A Large Ion Collider Experiment) [2] is one of the four large experiments of the LHC. A major challenge faced by the ALICE collaboration from 2007 to 2010 was to understand the detector and results obtained from data collected in the first few months of running of the LHC. These studies were called "first physics". The work in this thesis focuses on the efficiencies of triggers used to take data and on diffraction, the largest source of systematic uncertainty in the "first physics" results in ALICE.

1.1 First LHC Physics

This section describes the quantities measured first, in every new detector at a new energy regime. Measurements of charged particle pseudorapidity density ($dN_{ch}/d\eta$), charged particle multiplicity (dN_{ev}/dN_{ch}) and transverse momentum (dN_{ch}/dp_T) spectra give us useful information to tune Monte Carlo (MC) models. A description of MC models is presented in chapter 3.

The main purpose of the ALICE experiment, described in chapter 2, is to measure the properties of strongly interacting matter created in heavy-ion collisions. However, the ALICE detector is capable of making many interesting measurements (detailed in the next paragraph) with proton-proton (pp) collisions as well, and a number of them were made during the initial pp run at luminosity $2 \times 10^{27}\,\mathrm{cm}^{-2}\mathrm{s}^{-1}$. Soft and semi-hard pp collisions at the LHC, besides serving as comparison

data for the heavy-ion programme, also are themselves important. ALICE has several features that make it an important contributor to pp physics at the LHC. Its design allows particle identification (PID) over a broad range of momenta, and also allows good tracking resolution for momenta from 100 MeV/c to 30 GeV/c. The low material thickness and low magnetic field of ALICE allow the study of low p_T phenomena in pp collisions at the LHC [3]. These studies help us understand the underlying event and also minimum-bias event (described in section 1.2) properties, which form a major part of the background in searches for rare high p_T processes.

The first samples of minimum-bias pp events were used to align tracking detectors. These data were used also for the determination of the charged particle pseudorapidity density at various centre-of-mass (CM) energies [4, 5, 6], multiplicity distributions [5, 6], transverse momentum distribution and mean-p_T dependence of multiplicity [7]. Data from the following months of running of the LHC were used for calibration of PID systems and to measure the momentum spectra of different particle species [8], strange particle production [9] and baryon-antibaryon asymmetry at mid-rapidity [1]. Lead-lead (Pb-Pb) measurements can be compared to pp measurements of the same observables. This helps in the identification and separation of genuine novel effects in Pb-Pb collisions from those already present in pp collisions [10].

Figure 1.1 shows the pseudorapidity distribution of inelastic and non-single diffractive (NSD) event classes at a CM energy of 900 GeV. These measurements provide information on the mechanism of multi-particle production, and are used in tuning the relevant MC parameters. Figure 1.2 shows the multiplicity distribution which is the frequency distribution of the number of charged primary tracks per event for ALICE data and the MC models PYTHIA 6 [11] and PHOJET [12]. D6T, ATLAS-CSC and Perugia-0 are different tunes of PYTHIA 6. The lower part of the figure shows the ratio of data and MC. This figure shows that none of the tunes of PYTHIA 6 describes data as well as PHOJET does. The p_T spectrum in figure 1.3 is obtained by counting the number of tracks in each p_T bin and then correcting for detector and reconstruction efficiencies and trigger bias.

---

[1]Rapidity (y) and pseudorapidity (η) are special co-ordinates used in particle physics to describe the momentum and angle of a particle relative to the beam axis. More information on this can be found in Appendix A.
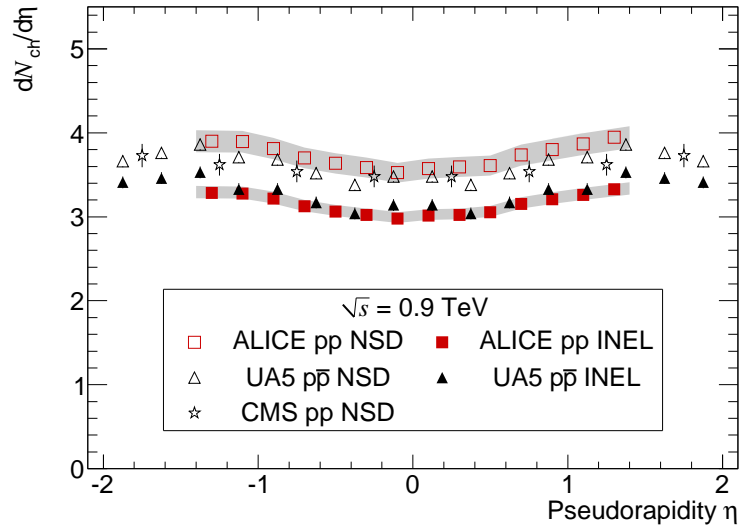
Figure 1.1: $dN_{ch}/d\eta$ distribution at ALICE, CMS and UA5 at 900 GeV [5].
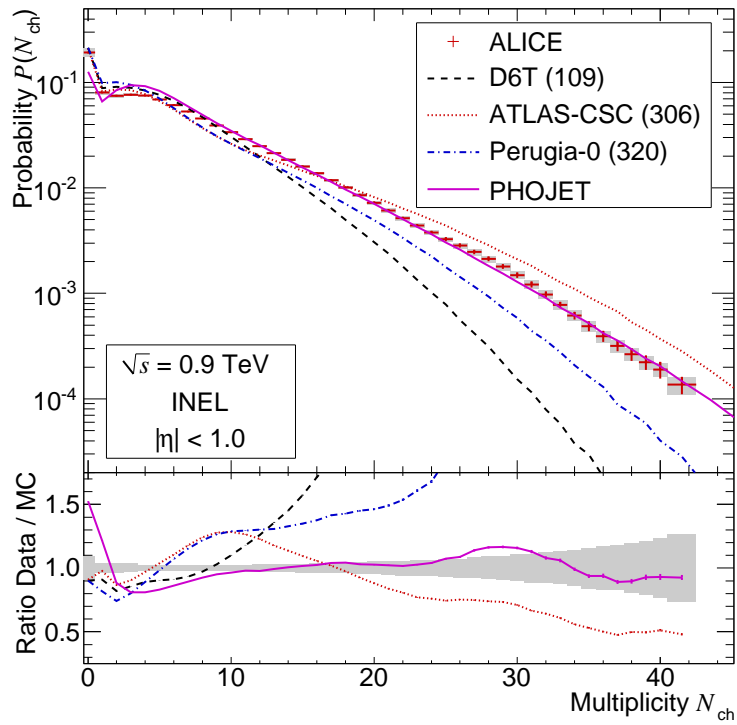
Figure 1.2: Multiplicity distribution at ALICE compared to different tunes of MC generators at 900 GeV [5].
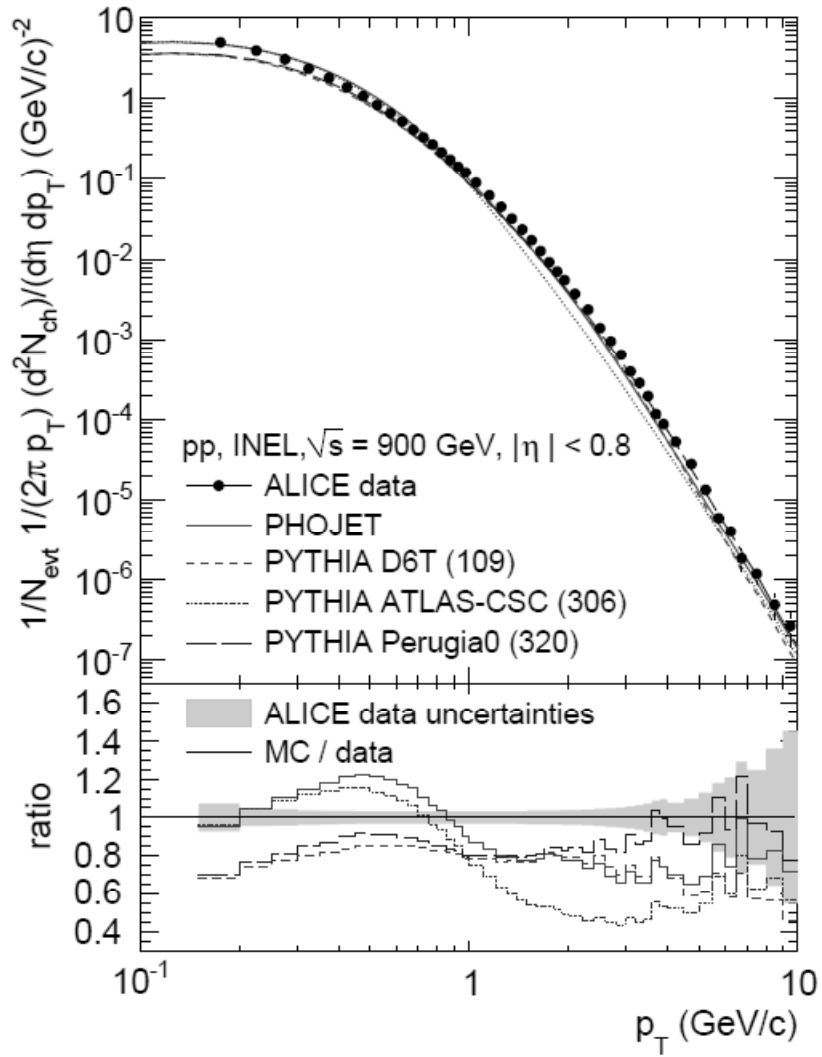
Figure 1.3: p_T distribution of inelastic events in ALICE compared to different tunes of MC generators at 900 GeV [7]. The bottom panel shows the ratio between MC and data.

1.2   Minimum Bias trigger and Efficiency

Trigger systems use a set of selection criteria defined in order to choose only the interesting events from the vast number of events produced in collisions. Minimum bias (MB) events are those events selected by a trigger with the least bias, or least rejection, among other possible trigger configurations. The definition of a MB trigger is detector dependent. A MB trigger should combine high efficiencies for all events, and in particular for low multiplicity and diffractive events, with a good beam gas (BG) [1] rejection.

As with any form of selection, this selection is subject to an efficiency of picking events of a particular physics process. The efficiency for a trigger of a particular process type gives the fraction of events of that process type selected by the trigger in question to the total number of events of that process type in the sample being analysed. The efficiency of a trigger depends on the physics process being studied and reflects the efficiency of the hardware and electronics in the detector. This topic is dealt with more extensively in chapter 5.

1.3   Importance of diffraction

As trigger efficiencies are not 100%, some of the events are lost. In a detector with good coverage, most of the lost events have products travelling down the beam pipe with a small scattering angle and low momentum transfer. Such events are mostly diffractive events. Diffractive events can be single diffractive (SD) or double diffractive (DD) if they have activity on one or both sides respectively. Owing to the difficulty in detecting difractive events, some experiments produce results for the NSD event class, excluding SD events from the sample of inelastic events. Figure 1.4 [5] shows results on average multiplicity as a function of CM energy from the ISR (Intersecting Storage Rings) [13] energies (63 GeV) to LHC start-up energies of (7 TeV). The experimental results shown are from CMS (Compact Muon Solenoid) [14], ALICE [5], UA5 [15], UA1 [16], PHOBOS [17], CDF (Collider Detector at Fermilab) [18] and STAR (The Solenoid Tracker at

---

[1]One of the sources of background is from protons in the beam interacting with some residual gas particle in the vacuum of the beam pipe. Such interactions are called "beam gas" interactions.

the Relativistic heavy ion collider) [19]. Results are presented for two different event classes - NSD, represented by the hollow symbols and solid line; and all inelastic events, represented by the solid symbols and dashed lines. Due to its importance in understanding the underlying event, diffraction will be explained in more detail in this thesis, in chapters 4 and 6.
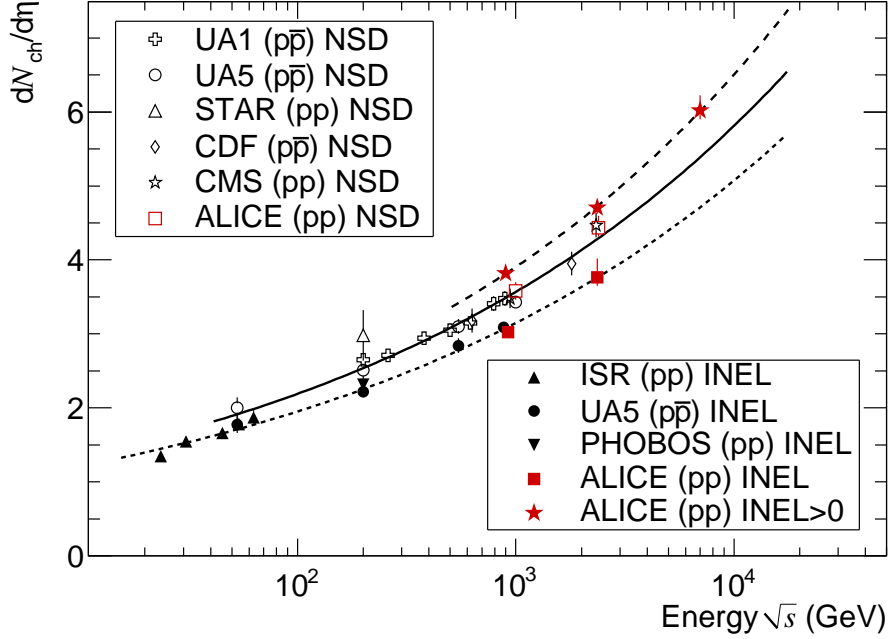
Figure 1.4: Experimental results of mean multiplicity as a function of CM energy for pp and p$\bar{\text{p}}$ [6].

1.4   Thesis Organisation

The thesis starts off with a description of the sub-detectors in ALICE. A brief mention of all detectors is made, while the detectors used in the analyses presented here are explained in further detail in chapter 2. The next chapter deals with different types of hadronic interactions, how they are classified and the Monte Carlo event generators used in the analyses presented here - PYTHIA 6 [11] and PHOJET [12].

Chapter 4 describes the kinematics of diffractive events, the diffractive physics in PYTHIA 8, the parameters used in its description, and the effect of changing these parameters on the average multiplicity. Chapter 5 discusses the calculation of trigger efficiencies using different triggers and the systematic uncertainty on multiplicity measurements. An estimate of the systematic uncertainty

on multiplicity is provided which was used as a cross-check for the first ALICE publications.

Finally, in chapter 6 a trigger with a high efficiency in picking diffractive events is used to obtain a sample of diffractive events from ALICE data. The pseudorapidity density, multiplicity and p_T distributions of this diffractive sample are presented and compared with MC models. Systematic uncertainties in the comparison are discussed.

The coordinate system used in ALICE is a right-handed coordinate system with its origin in the center of the detector; the positive x direction points towards the Salève; the positive z direction (A side) points towards Bellegarde. The negative z direction is the C side of the detector.

ALICE AT THE LHC

Founded in 1954, by 12 countries in Western Europe, CERN [1] (the European Organisation for Nuclear Research) stretches across the French-Swiss border near Geneva. Its current flagship project is the LHC, the world's largest and highest-energy particle accelerator, colliding beams of protons or lead ions moving almost at the speed of light. CERN houses a complex of interconnected accelerators, each feeding the next in the chain until the last and biggest link, the LHC [1].

2.1 The LHC

The LHC project was approved in 1994 after a 10-year discussion period. The LHC [1] is a two-ring-superconducting-hadron accelerator and collider built in the existing tunnel that hosted the CERN LEP (Large Electron-Positron collider) machine [20]. This tunnel is 26.7 km in circumference and is about 45-170 m underground on a plane inclined at 1.4%. The LHC is a synchrotron that accelerates, focuses and bends two counter-rotating beams in separate beam-pipes.

The LHC ring is segmented into 8 *sectors* (*octants*) as seen in figure 2.1, each with a straight section at its centre called an interaction *point*. The LHC tunnel is interrupted by four experimental halls that house the experiments: ALICE [21] at point 2, ATLAS (A Toroidal Lhc ApparatuS) [22] at point 1, CMS [23] at point 5 and LHCb (LHC beauty) [24] at point 8, shown in figure 2.1.

---

[1]The acronym CERN originally stood, in French for, Conseil Européen pour la Recherche Nucléaire which was a provisional council established by 11 European governments in 1952, for setting up the laboratory. The acronym was retained even after the provisional council was dissolved.
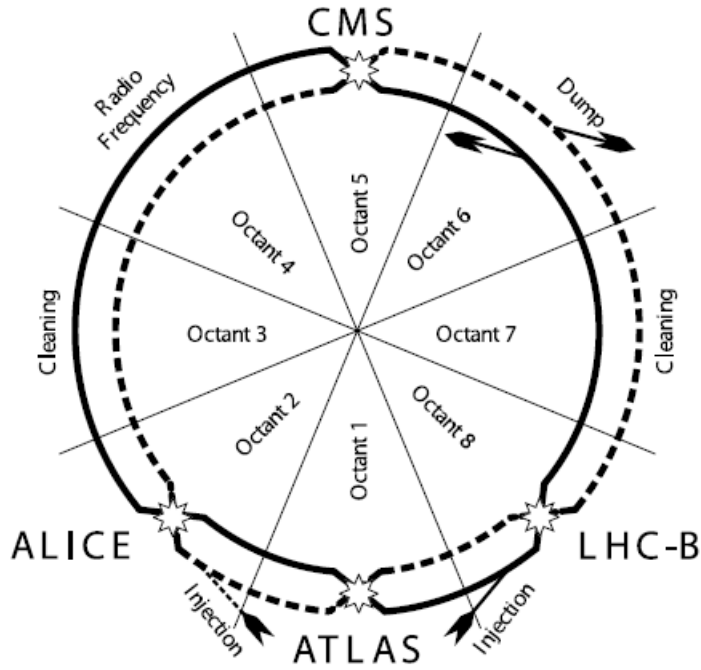
Figure 2.1: The LHC ring with its sectors and four experiments.

ATLAS and CMS are aimed at studying new particles at high-energies, while LHCb is built to study Charge Parity (CP) violation in b-quark systems. ALICE is a dedicated heavy-ion experiment intended to study strongly-interacting matter, phase transitions into the quark-gluon plasma and its properties. ALICE has a pp physics programme as well. The analyses described in this thesis are on data obtained from the ALICE experiment taken with pp collisions. Two smaller experiments called LHCf (Large Hadron Collider forward experiment) [25] and TOTEM (TOTal Elastic and diffractive cross-section Measurement) [26] measure forward particles created during LHC collisions. LHCf is located near the ATLAS experiment while TOTEM is located near the CMS experiment.

Hydrogen atoms are stripped of their electron leaving a proton. These protons are accelerated to 50 MeV in the LINAC2 (linear accelerator), injected into the PS (Proton Synchrotron) booster and the SPS (Super Proton Synchrotron). They are grouped into bunches in the PS and are accelerated to the LHC injection energy of 450 GeV in the SPS. Figure 2.2 shows the layout of the rings. Two transfer tunnels, TI 2 (2.6 km) and TI 8 (2.5 km), link the LHC to the CERN accelerator complex and act as injectors of the beams to be collided. Two counter-rotating beams that consist

of a maximum of 3564 bunches of 100 billion particles are injected into the LHC just before points 2 and 8. 1232 dipoles, each of length 14.3 m, bend the beams. The magnetic field provided by the dipoles is 0.535 T at the LHC injection energy, going up to 8.33 T at a maximum beam energy of 7 TeV. The magnets are cooled to 1.9 K, using super-fluid helium, to make them superconducting. Guided by these magnets, the bunches go round the LHC ring over a hundred million times, picking up a small amount of energy on each lap. Radio frequency (RF) accelerator cavities located at point 4 accelerate the beams to reach the desired collision energy and also compensate for the energy loss due to synchrotron radiation. Points 3 and 7 have collimators to remove particles with a large spatial distance from their bunch, giving rise to *beam halo*, and also for momentum cleaning. This ensures that particles are kept within bunches and have the same momentum. Finally, in point 6 the beam dump system [1] safely extracts both beams through transfer tunnels. An extracted beam is dumped onto large blocks of granite surrounded by steel and concrete.
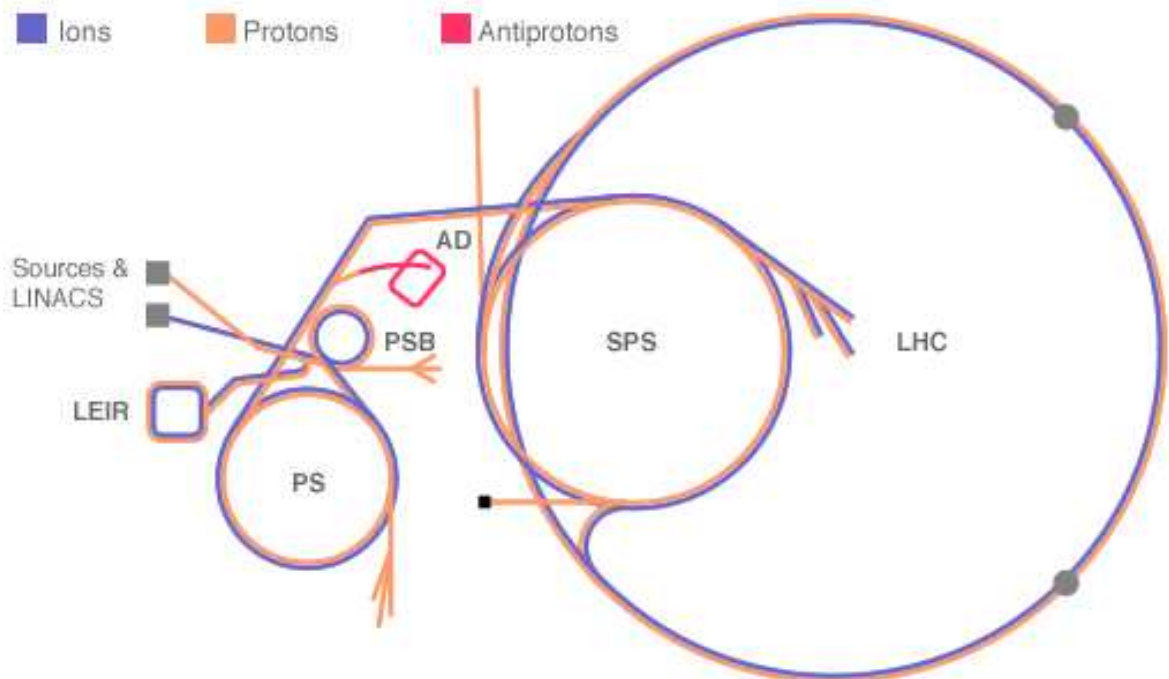
Figure 2.2: The various rings used in the preparation of beams for the LHC.

Once the beams have picked up the intended energy for collision, they are guided towards each other inside the detectors where they collide. Each time the beams intersect at the maximum de-

sign luminosity [1] of $10^{34}\,\mathrm{cm}^{-2}\mathrm{s}^{-1}$, on average, 20 particles per bunch collide but, because bunches collide every 25 ns and only a fraction of bunches are filled, altogether about 800 million collisions will take place every second.

Lead ions are produced using a source of vapourised lead. These ions are sent into LINAC3, followed by the Low Energy Ions Ring (LEIR) and then take the same route as the protons. Lead ions collide with an energy of 2.76 TeV per nucleon resulting in $\sqrt{(s_{\mathrm{NN}})} = 5.5$ TeV. The design luminosity for Pb-Pb collisions is $10^{27}\,\mathrm{cm}^{-2}\mathrm{s}^{-1}$.

2.2 ALICE

ALICE, located at Point 2 on the LHC, is a general-purpose heavy-ion experiment designed to study the physics of strongly interacting matter in nucleus-nucleus and pp collisions. The ALICE pp physics programme is the basis of this thesis. The experiment was approved in 1997 and is built by a collaboration of over 1000 physicists and engineers from 30 countries. The ALICE detector is 26 m long, 16 m high and 16 m wide, and weighs 10,000 tonnes. It has 18 sub-detector systems, each with their own technology choice and design constraints.

The ALICE [21] detector, seen in figure 2.3, has two main components: the central barrel and the forward muon spectrometer. The central barrel is enclosed by a large solenoid magnet reused from the L3 experiment at LEP [20] with a field of 0.5 T. It covers polar angles from $45°$ to $135°$. Wrapped around the interaction point from innermost to outermost are the Inner Tracking System (ITS), the Time Projection Chamber (TPC), the Transition Radiation Detector (TRD), Time of Flight (TOF), High Momentum PID (HMPID), PHOton Spectrometer (PHOS) and the Electro Magnetic CALorimeter (EMCAL).

Figure 2.4 shows the η coverage of various detectors. All detectors in the central barrel except HMPID, PHOS and EMCal cover the full azimuthal angle. Other small angle (θ) detectors are the

---

[1]Luminosity is given by $L = fn\frac{N_1 N_2}{A}$, where n is the number of bunches in each beam revolving with frequency f. There are N_1 and N_2 particles in the colliding bunches, which have an overlapping area of A.
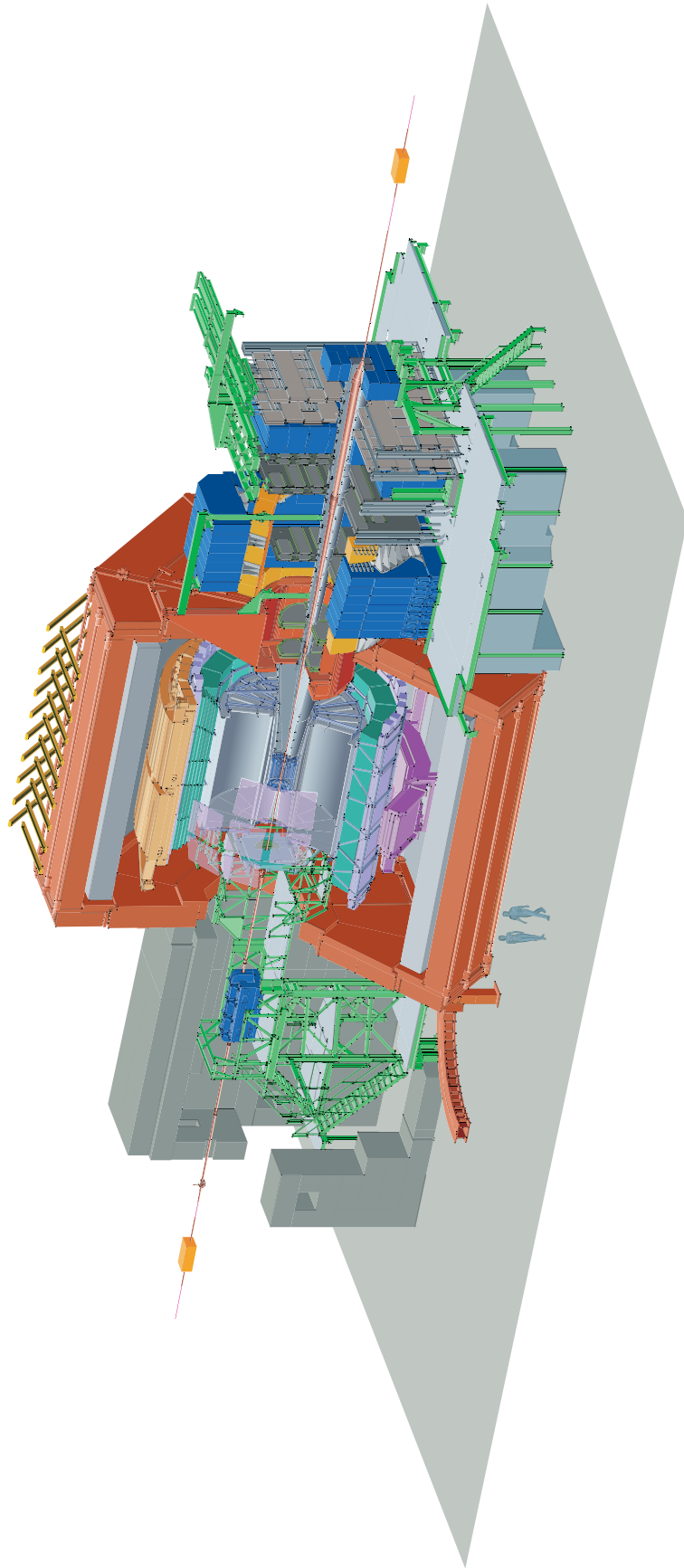
Figure 2.3: The ALICE detector [2].
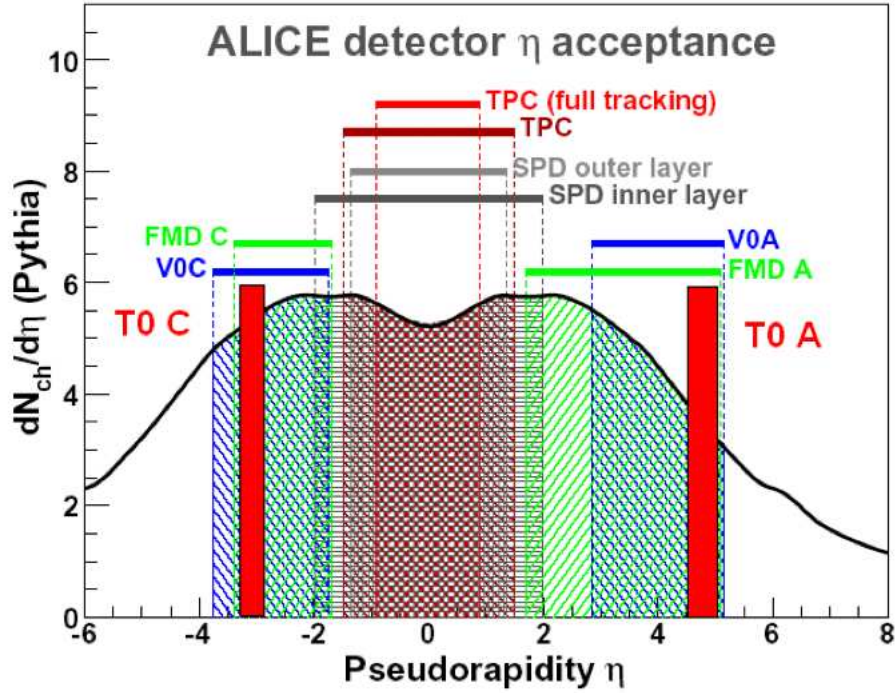
Figure 2.4: Pseudorapidity coverage of the ALICE detector [27].

Zero-Degree Calorimeters (ZDC), the Photon Multiplicity Detector (PMD), Forward Multiplicity Detector (FMD), the T0 and the V0 detectors. The forward muon arm consists of a complex arrangement of absorbers, a large dipole magnet (with field 0.67 T) and fourteen planes of tracking and triggering chambers. An array of scintillators called Alice COsmic Ray DEtector (ACORDE) is located on top of the ALICE solenoid magnet.

The design of the detector has been based on the highest expected value of multiplicity of charged particles produced in a central Pb-Pb collision (8000 per unit rapidity for $|\eta| \leq 0.9$). This multiplicity dictates the granularity of the detectors and their optimal distance from the colliding beams. The ITS, TPC, TRD and TOF are supported inside the solenoid magnet by the space-frame. The space-frame is a cylindrical stainless steel construction 7 m long and 8.5 m in diameter.

The detectors used in analyses presented in this thesis are described in more detail in the following sections. More information on other detectors can be found in reference [2].

13

2.2.1 Tracking Detectors

Tracking is the act of measuring the direction and magnitude of a charged particle's momentum. Charged particles entering a tracker cause a trail of ionisation by releasing a part of their energy in the device. The finely segmented tracker then identifies the path of the particle. An almost homogeneous magnetic field is present in the region which makes charged particles follow a helical path. The direction of the charged particle determines its charge and the curvature of its path gives its momentum.

Track finding at the LHC (especially in heavy-ion collisions) presents a huge challenge, because of the extremely high track density. The main tracking detectors used for the first physics measurements were the ITS and the TPC.

ITS

The ITS is made of six cylindrical layers of silicon detectors surrounding the beam pipe as seen in figure 2.5. The layers are located at radii between 4 cm and 43 cm. There are two layers each of pixel, drift and strip detectors. They surround the collision point and are used primarily to determine the positions of primary vertices with a resolution better than $100\,\mu$m [2]. The ITS also helps in reconstructing secondary vertices and to track and identify particles with momentum above 200 MeV/c. It can be used for stand-alone tracking for particles that do not reach the TPC as the p_T cut-off for the inner two pixel layers at nominal field is 35 MeV/c. However, absorption limits the momentum to 50 MeV/c. The rapidity coverage of the ITS is $|\eta| < 0.9$ [2] for all vertices located within the length of the interaction diamond. The interaction diamond is the region around the interaction point with length $z = \pm 5.3$ cm ($\pm 1\sigma$) [2] along the direction of the beam and height 1 cm in the transverse direction. This diamond shaped surface in the $z - x$ plane is rotated about the z axis by $180°$ to form a diamond shaped volume.

The Silicon Pixel Detector (SPD) comprises the two innermost layers of the ITS placed at 3.9 cm and 7.6 cm, with an acceptance of $|\eta| < 2$ and $|\eta| < 1.4$ respectively. Its primary purpose is to determine the position of the primary vertex. It is designed to deal with the high particle density at
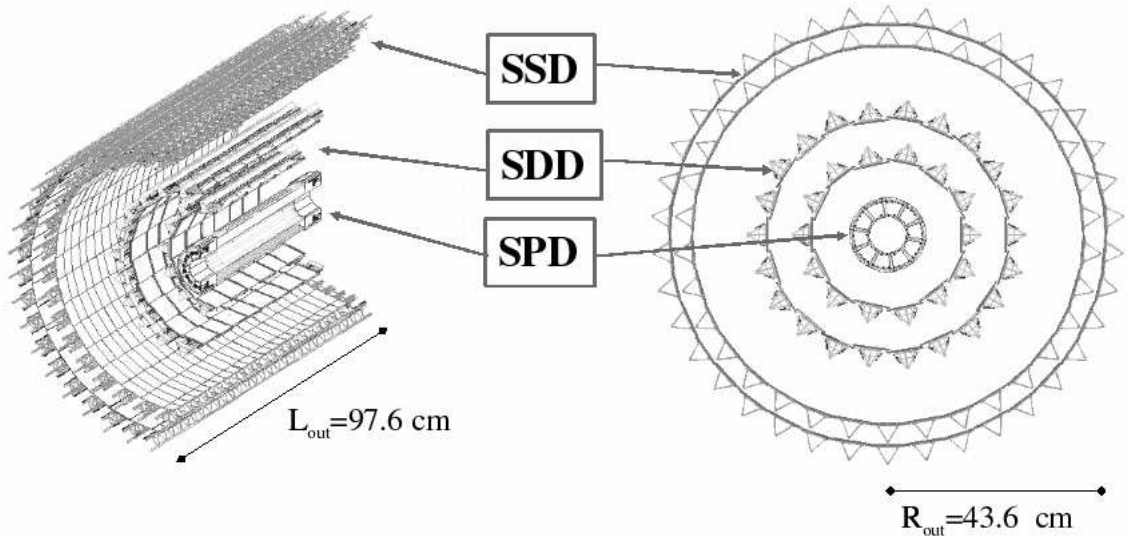
Figure 2.5: Layout of the ITS detector [2].

the LHC (as many as $50 \, cm^{-2}$ in Pb-Pb). The interaction vertex is reconstructed using information only from the SPD. The SPD is based on hybrid silicon pixels in a two-dimensional matrix of read-out chips. Each chip contains 8192 readout cells [2]. Chips are arranged on ladders. In total there are 240 ladders and 1200 chips giving a total of 9.8×10^{6} pixels [2]. These channels are read out in binary mode: a signal above a threshold implies a change in the digital output level. Since no energy-loss information is recorded, the SPD does not help in Particle Identification (PID). Each pixel cell measures $50 \, \mu m$ in the $r\phi$ direction and $425 \, \mu m$ in z giving the SPD a spatial precision of $\sim 12 \, \mu m$ along the $r\phi$-axis and $100 \, \mu m$ along the z-axis. The two track resolution is $100 \, \mu m$ along the $r\phi$-axis and $850 \, \mu m$ along the z-axis.

The Silicon Drift Detector (SDD), produced from a homogeneous high-resistivity $300 \, \mu m$ silicon wafer, makes up the two intermediate layers of the ITS. The analogue readout through 133000 channels provides energy-loss information useful in PID. Each drift cell measures $202 \, \mu m$ in the $r\phi$ direction and $294 \, \mu m$ in z giving the SDD a spatial precision of $35 \, \mu m$ along the $r\phi$-axis and $25 \, \mu m$ along the z-axis. The two track resolution is $200 \, \mu m$ along the $r\phi$-axis and $600 \, \mu m$ along the z-axis.

The outer two layers of the ITS form the Silicon Strip Detector (SSD). They consist of sensors with silicon micro-strips on both sides. They provide a two dimensional measurement of the track

15

position and are crucial in matching tracks from the TPC and ITS. Since they also provide information on energy loss (dE/dx), they assist in PID for low-momentum particles. Each strip cell measures $95\,\mu m$ in the $r\phi$ direction and $40\,mm$ in z giving the SDD a spatial precision of $20\,\mu m$ along the $r\phi$-axis and $830\,\mu m$ along the z-axis. The two track resolution is $300\,\mu m$ along the $r\phi$-axis and $2400\,\mu m$ along the z-axis.

TPC

Particle tracking continues in a large, gas-filled detector called the TPC. The TPC is the main tracking detector of the central barrel. Along with other central barrel detectors, it is optimised to provide charged particle momentum measurements with good two-track separation, PID and vertex determination.

The TPC, shown in figure 2.6, is cylindrical in shape and 5 m in length. Its inner and outer radii are 85 cm and 250 cm respectively. The detector is made of a large field cage, weighing about 8 tonnes and filled with $90\,m^3$ of Ne, CO_2 and N_2 [2]. The voltage gradient in the TPC is $\sim$ $400\,V/cm$, with a high voltage of $100\,kV$ at the central electrode at $z = 0$. The two read-out planes are at $z = \pm 2.5\,m$. Following ionisation, electrons are transported from either side of the central electrode to the end plates, where there are readout pads. The maximum drift time of electrons is $\sim 90\,\mu s$ [2], making it the detector in ALICE with the longest sensitive window, and thus limiting the luminosity. Up to 16,000 tracks can be reconstructed and identified in one event.

The phase space covered by the TPC is $|\eta| < 0.9$ for tracks reaching the outer wall of the TPC with full radial track length and $|\eta| < 1.5$ for reduced track length (no matching with other detectors). Except for the dead zones between the readout chambers, the TPC covers the full azimuth with a p_T range of about $0.1\,GeV/c \leq p_T \leq 100\,GeV/c$. For $p_T > 0.5\,GeV/c$, the tracking efficiency of the TPC is above 90% [2].

The TPC, SSD and the SDD provide PID via ionization measurements. The gas in the TPC is ionized by charged particles travelling through it. These charged particles deposit energy along

16

their path. The Bethe-Bloch equation relates the energy deposit to the velocity of the particle. From the velocity and momentum measurements, one can determine the mass and hence, the PID of the particle. In the TPC, the PID procedure is applied to all reconstructed tracks that have been associated to the TPC.

2.2.2 Triggering Detectors

The trigger system uses a set of selection criteria defined in order to select and record events of different types. It is used in high-energy physics as a means to choose only the interesting events from the vast number of events produced in collisions. For the analysis presented in this thesis, signals from two different detectors, V0 and SPD, are used to define triggers.

V0

The V0 detector is a forward detector. It consists of two arrays of scintillator counters, the V0A and V0C, which are installed on either side of the interaction point. The V0A is located 340 cm from the vertex on the opposite side of the muon spectrometer, whereas the V0C is fixed to the front face of the muon arm absorber (which absorbs photons and hadrons from the interaction vertex), 90 cm from the vertex [2]. Each disk has 32 elementary counters arranged in four rings and eight sectors. The pseudorapidity range of V0A is $2.8 < \eta < 5.1$ and that of V0C is $-3.7 < \eta < -1.7$ [2]. The time resolution of individual counters is better than 1 ns. In pp collisions, the efficiency for the detection of at least one charged particle detected in both sides is about 75% [2] when no secondary particle is taken into account, and increases to 84% when secondaries are included.

The V0 detector has several functions. It provides minimum bias triggers for the central barrel detectors. The timing difference between the two V0 disks (V0A and V0C) acts as an indicator of the position of the interaction point. The V0 also provides trigger background corrections in the form of beam gas suppression ($\overline{\text{BG}}$). The V0 trigger uses the fact that particles from pp and BG interactions arrive at the two disks of scintillators at different times. The time difference between

SERVICE SUPPORT WHEEL

END PLATE

GLIDER FEET

INNER CONTAINMENT VESSEL

OUTER CONTAINMENT VESSEL

GLIDER FEET

END PLATE

SERVICE SUPPORT WHEEL
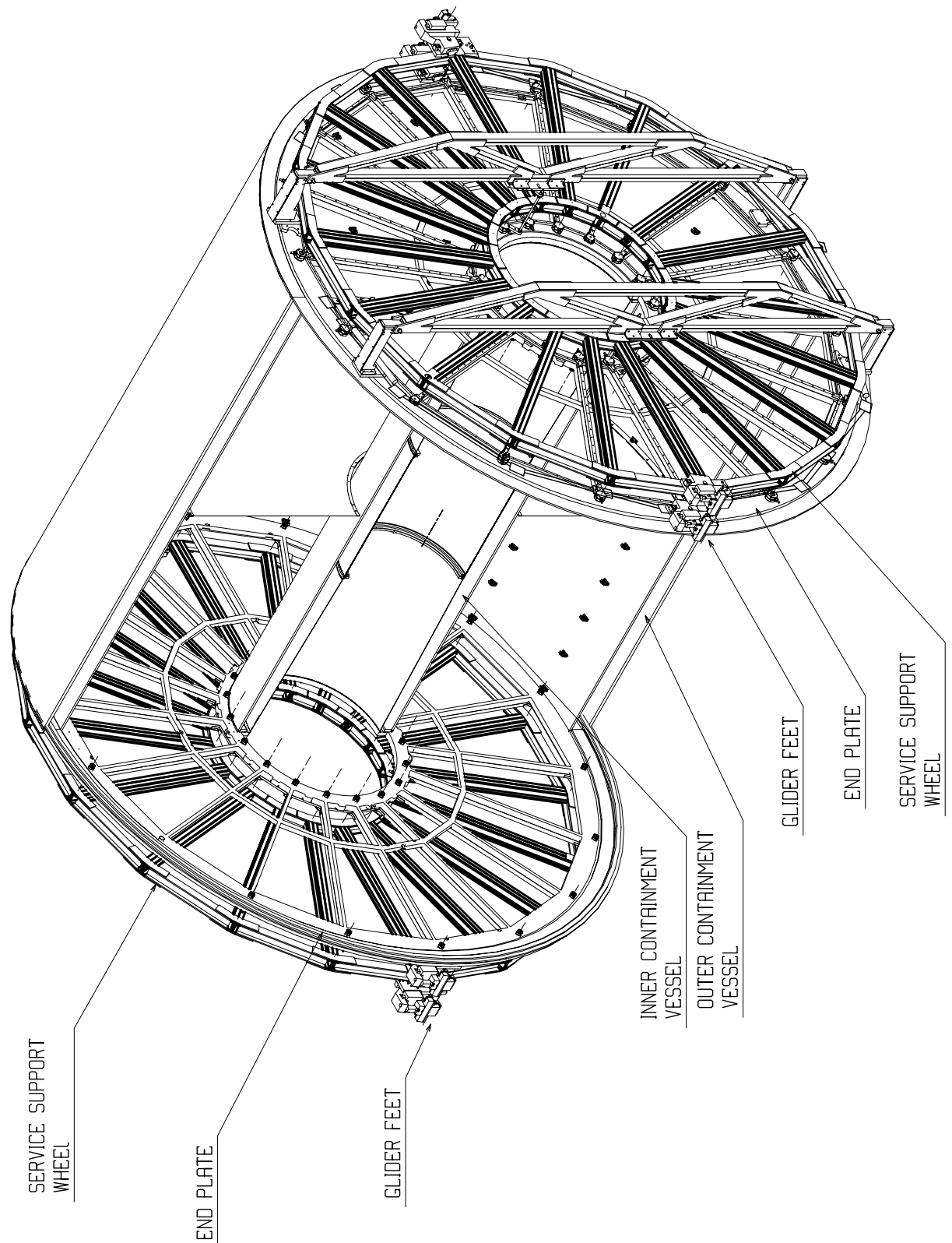
Figure 2.6: Layout of the TPC detector [2].

the hits on the two disks for a pp interaction is different from the time difference between hits for a BG interaction [28].

SPD

The SPD also acts as a triggering detector. Each pixel chip generates a pulse whenever at least one pixel cell receives a particle signal above a threshold. This produces the "Fast-OR" digital pulse that allows a prompt trigger at the Level 0 (described in section 2.3). The Global Fast-OR (GFO) signal is the "or" of all the pixel chips, i.e., it sends a signal if any one of the pixel chips fires. The SPD can also be used with more complex trigger patterns involving hits in both layers to identify tracks and trigger on multiplicity. The SPD complements the V0 detector in providing minimum bias triggers because its geometrical acceptance is in the central rapidity region. The GFO output is integrated over 100 ns corresponding to 4 bunch crossings in pp collisions. The coincidence between the pixel trigger and the V0 signal is necessary to identify the bunch crossing that caused the trigger.

2.3   The ALICE Trigger

The ALICE trigger [21] is designed to select events with a variety of different features at a rate which can be scaled down to suit physics requirements. Restrictions imposed by the bandwidth of the Data Acquisition (DAQ) system also determine the trigger rate. The hardware trigger system in ALICE is called the Central Trigger Processor (CTP). The CTP receives inputs from a subset of (triggering) detectors and issues trigger signals by combining these inputs by logical operators. Data that pass the CTP trigger are read out.

In addition, the CTP takes care of downscaling (reducing the rate of signals), pile-up (multiple interactions) protection in different bunch crossings and busy status of detectors (inability to process an event). Trigger signals are sent to a group of readout detectors called a "cluster". Trigger classes are defined in terms of the logical condition demanded for the inputs. Each trigger class is associated to a cluster of detectors.

The detectors in ALICE have been chosen principally to cope with very high multiplicities and use a variety of different techniques. In some cases, the electronics associated with these detectors requires a fast response ($\sim 1\,\mu s$) and therefore the first trigger must reach the readout detectors in this time. Hence, trigger decisions are split into three levels: a Level 0 (L0) signal, which reaches detectors at $1.2\,\mu s$, and a Level 1 (L1) signal arriving at $6.5\,\mu s$. The L0 signal is too fast to receive all trigger inputs; the ones not picked up by L0 are picked up by L1. The third step, the Level 2 (L2) decision, comes after the end of the drift time in the TPC at about $96\,\mu s$ [2]. In order to deliver the L0 signal $1.2\,\mu s$ after an interaction, the CTP must make the L0 decision within $100\,ns$ of receiving a signal. Among others, the V0 and SPD signals arrive at the L0 level. An event is read out to the DAQ only after the L2 trigger.

2.4   ALICE offline and the Aliroot framework

Once an event is recorded, analyses are performed "offline". The ALICE offline framework is called AliROOT [29]. It implements Object-Oriented techniques based on the ROOT framework [30] for analyses and AliEn [31], a grid framework, to access the computing Grid [32]. Being in continuous development since 1998, this C++ based framework is used for simulation, alignment, calibration, reconstruction, visualisation and analysis of experimental data.

AliROOT is used to reconstruct events that took place inside the real detector as well as simulated data; the main concepts and their relations are shown schematically in figure 2.7. In the case of simulated events, the first step involves an event generator such as PYTHIA 6 [11] or PHOJET [12]. The event generator is interfaced with AliROOT to produce a *kinematics tree* containing all information like type, charge and momentum of the generated particles and their decay products. These particles are transported through the detector and the response of the detector to a passing particle is simulated. When there is some energy deposition in a detector, a *hit* is recorded along with the position and time of the hit. Along with this information, a *track reference* is also stored to follow the path of the particles. Each detector's response function and noise are taken into ac-
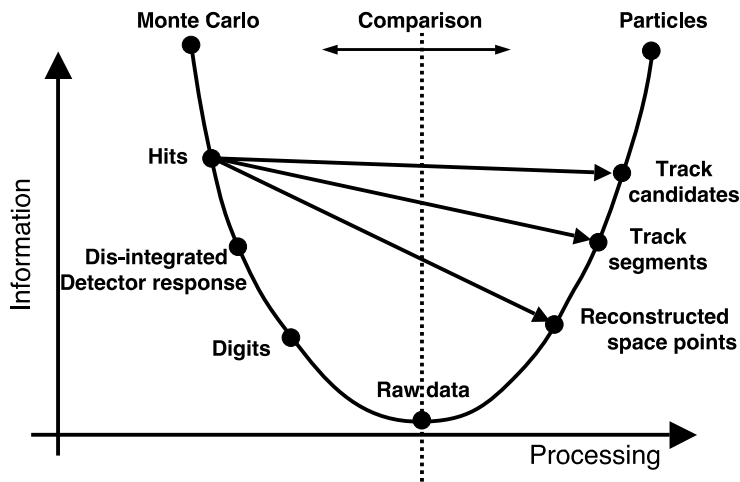
Figure 2.7: Data processing framework in ALICE [2].

count and hits are stored and converted to *digits*. These digits are stored as *raw data*, in a hardware format specific to each detector.

At this stage raw data from simulation are similar to raw data produced by interactions within the detector. All subsequent steps of the reconstruction chain are identical for raw data from either source.

The first step in reconstruction is a local reconstruction within the detectors called *clusterisation*. Particles traversing a detector leave energy deposits and timing information in more than one detecting element. Signals from adjacent elements are combined to form a *cluster*, to determine the exact position and time of the particle, to reduce noise and also to unfold signals from overlapping particles.

2.4.1 Track reconstruction

Clusters in different layers are combined to form *tracks*. The curvature and energy loss along the track are used to determine the momentum and PID. Track finding in ALICE employs the Kalman filter method [33]. The first step in this method is the determination of the initial seed for track parameters. Track seeds are found by combining information from the outer layers of the TPC, where the track density is minimal, assuming that the tracks originate from the primary vertex. Then the track is followed inwards towards the inner radius of the TPC. At each stage, clusters that fit the track are added to the track. When all seeds are extrapolated to the inner radius of the TPC, the ITS continues the track reconstruction towards the primary vertex.

When more than one space-point candidate is found to prolong the track in the ITS, all candidates are followed as different hypotheses towards the inner ITS layers. A decision is made in the end based on the sum of the χ^2 along the track's path. Following ITS tracking, the Kalman filter is reversed and tracks are followed outwards, starting from the inner ITS layers, with more precise track parameters. Improperly assigned points are eliminated and tracks are followed beyond the TPC. Finally, the Kalman filter is reversed one last time to refit tracks from outside, inwards. Secondaries are found in a similar way without imposing the constraint that the tracks originate from the primary vertex.

Global ESD tracks are produced with information from the TPC along with information from other detectors including the ITS when the track is within their acceptance. Those tracks with only information from the TPC are called *TPC-only* tracks. The ITS on its own can also be used to reconstruct tracks once all space-points already assigned to tracks have been removed. Tracks that have not been seeded in the TPC can be found in this way. The SPD on its own can reconstruct *tracklets*. Tracklets are reconstructed by drawing straight lines from a cluster in each of the two SPD layers. An event vertex is found where most of these lines intersect. Then, lines that point to the vertex are identified as tracklets.

2.4.2   Vertex Reconstruction

A vertex is a point of collision or decay. The primary vertex is the origin for all particles produced in a single pp interaction when the two (proton) beams collide. Subsequently, some of the produced particles may decay to more particles. Such a topological structure leads to a secondary vertex, the origin of decay tracks. Particles may also interact with the detector material, giving rise to a secondary vertex and a set of associated tracks.

The primary vertex position is determined from the information provided by the SPD. Pairs of reconstructed points in the two layers of the SPD, that are close in the azimuthal (ϕ) and polar (θ) angles are chosen. Their intersection determines the vertex position. A vertex can also be found with information from tracks in the TPC and global tracks. The resolution on the position of the primary vertex depends on the charged track multiplicity of the event.

The secondary vertex position is found by combining tracks that originate sufficiently far away from the primary vertex. If the calculated distance of closest approach (DCA) of the two opposite sign tracks that we combine, is below some pre-determined value and the point of closest approach is before the first measured points of either of the tracks, this point is considered as a potential candidate for a secondary vertex. Additional cuts are imposed in the analysis phase depending on the type of analysis being carried out.

HADRON INTERACTIONS AND MONTE CARLO GENERATORS

The Standard Model [34] of particle physics is a model that contains a description of the elementary particles and their interactions. Elementary particles are grouped into fermions with half-integer spin and bosons that have integer spin. Fermions make up matter while bosons are the force carriers that mediate interactions. Elementary fermions can either be quarks or leptons. There are three generations of fermions with two quarks and two leptons in each generation. Each of these particles has a corresponding anti-particle. Anti-particles have the same mass and spin as their respective particles, but other properties, for example, electric charge and colour, are opposite.

Quarks carry a colour charge and interact via the strong force. They are held together by gluons (the strong force carriers) to form hadronic matter such as protons and neutrons. Gluons also carry a colour charge and have two units of colour. They can interact independently and can self-interact forming gluon loops. The theory of strong interactions is called Quantum Chromodynamics (QCD) [34]. As a consequence of the gluon carrying a colour charge, QCD has the properties of asymptotic freedom and confinement [34].

This chapter outlines some of the main features of strong interactions. Based on the scale of momentum transfer, interactions are classified as either hard or soft. Perturbative QCD is used to describe hard interactions. Due to the lack of knowledge in performing non-perturbative cal-

24

culations, phenomenological models are used to describe soft interactions. A description of one such phenomenological model based on Regge theory is discussed. Interactions are also classified based on the characteristics of the final states. A detailed description of this classification is provided.

The next section of this chapter describes Monte Carlo event generators. In particular, the most important features of two event generators, PYTHIA 6 and PHOJET are discussed, with most emphasis on the modelling of diffraction. Finally, some kinematic distributions from the two generators PYTHIA 6 and PHOJET are compared.

3.1 Strong interactions

Confinement restricts the observed strongly interacting matter to colourless combinations of quarks and gluons. Quarks are never observed unbound in normal hadronic matter. They are either seen as a bound state of three quarks (or anti-quarks) called a baryon (or anti-baryon) or as a bound state of a quark and an anti-quark called a meson. Hadrons (baryons and mesons) are colour singlets.

The potential between two heavy quarks in a vacuum is given by

$$V(r) = -\frac{\alpha_s}{r} + kr, \qquad (3.1)$$

where α_s is the strong coupling constant between the two quarks, k is the string tension and r is the separation between the two quarks. The first term is the Coulombic potential term and dominates at small r, making the system behave similarly to the electromagnetic case. The second term dominates at large r. The energy binding the two quarks stretches the colour lines into a tube and increases with separation r until it is energetically more favourable to form a new quark-antiquark pair.

The coupling constant α_s depends on the momentum transfer in an interaction and is not constant,

as shown in figure 3.1. The existence of self-interacting gluon loops is responsible for α_s decreasing rather than increasing with increasing energy scale Q^2 or decreasing r. At large Q^2, α_s tends to zero making the quarks' interactions weaker. In the limit $r \rightarrow 0$, quarks may behave as free or non-interacting particles. This phenomenon is called asymptotic freedom. Although the value of α_s is determined from experiment, its energy dependence can be predicted from QCD.
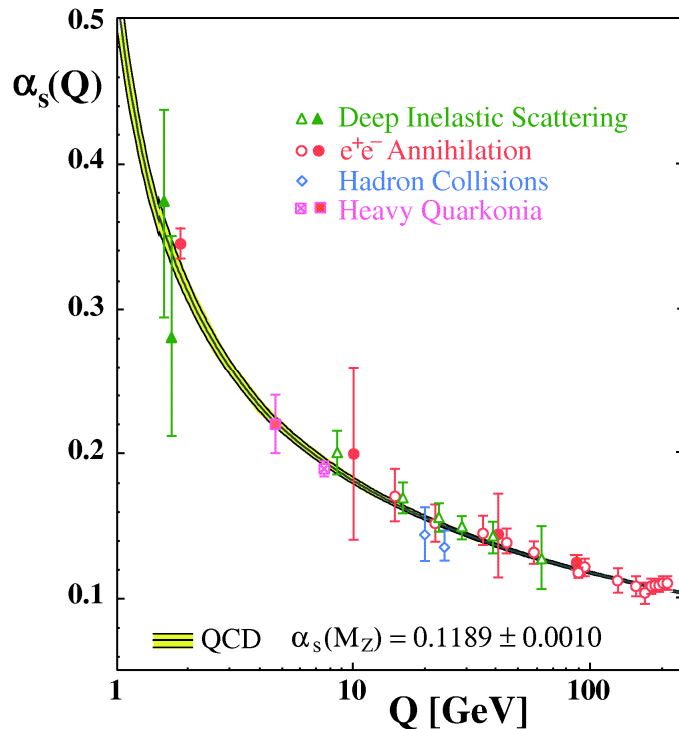
Figure 3.1: Strong coupling constant (α_s) as a function of energy scale Q. Open symbols indicate NLO, and filled symbols NNLO QCD calculations used in the respective analysis. The curves are the QCD predictions for the combined world average value of $\alpha_s(M_{Z^0})$. For details see [35].

At high Q^2, α_s is significantly smaller than 1. In this region, a perturbative approach has been adopted to describe experimental results. However, at low Q^2, α_s is not small enough for higher order diagrams to have a smaller contribution than lower order ones and one cannot use a perturbative approach. In this low Q^2 region, the behaviour and interactions of quarks is qualitatively different and it is here that confinement is observed. The energy scale before α_s approaches 1 is the scale at which the theory becomes non-perturbative. This scale is given by Λ_{QCD}, known as the QCD scale and experimentally determined to be $\sim 200\,\text{MeV}$, which is comparable to the mass of the pion (m_π).

Hadronic processes can be classified as being either soft or hard based on the magnitude of the transverse momentum scale involved compared to Λ_{QCD}. Soft processes, that dominate hadronic scattering cross-sections, are characterised by an energy scale of the order of the hadron size ($\sim 1\,\mathrm{fm} \approx (200\,\mathrm{MeV})^{-1} \approx \Lambda_{QCD}$) [36]. The hard sector is described very well by perturbative QCD (pQCD).

3.1.1 Deep Inelastic Scattering

Although quarks cannot be isolated from hadrons, they can be observed in experiments. Deep Inelastic Scattering (DIS) is the first process in which point-like partons (quarks and gluons) were observed inside hadrons. In DIS the structure of an individual proton is probed by scattering electrons with an energy of a few GeV. In fixed target electron scattering data, the cross-section as a function of the energy of the electrons after scattering shows a large elastic scattering peak where the proton recoils as a whole, a few subsidiary peaks due to proton excitation to higher-mass resonant states and a continuum distribution of electrons that have been scattered by the proton's constituent quarks. Such a spectrum is observed if the scattering is due to free, point-like, charged particles. At energies of a few hundreds of GeV (at HERA [37]), struck quarks are not observed as free particles due to confinement, and are observed as 'jets' of hadrons travelling in the same direction as the quark. Similarly in hadron-hadron collisions, partons scatter and hadronize to manifest themselves as 'jets' of hadrons travelling in the same direction as the struck parton.

The production of high momentum hadrons can be described by the *parton model*, in which a hadron is composed of a collection of quarks and gluons. Distributions of partons in particles are characterised by Parton Distribution Functions (PDFs). A PDF $f_i(x, Q^2)$ gives the probability of finding a parton i with a fraction x of the momentum of the parent beam particle, when probed at a scale Q^2. Because of confinement, p-QCD cannot be used to obtain PDFs. The known PDFs are extracted from experimental data. The cross-section for a hadron-hadron (for example pp) scattering into two jets is given by

$$\frac{d^3\sigma(pp \to klX)}{dx_1 dx_2 d\hat{t}} = \sum_{i,j} f_{p_i/p_1}(x_1, Q_1^2) f_{p_j/p_2}(x_2, Q_2^2) \frac{d\sigma_{(ij \to kl)}}{d\hat{t}} \tag{3.2}$$

where $f_{p_i/p_1}(x_1, Q_1^2)$ and $f_{p_j/p_2}(x_2, Q_2^2)$ are the PDFs of the protons 1 and 2. They give the density of partons of type i and j in the protons with fractional momenta x_1 and x_2. $d\sigma_{ij}/d\hat{t}$ is the parton-parton cross-section and $\hat{t}$ is the momentum transfer between the colliding partons. X is the proton remnant after the scattering. The observed final state hadrons in the two jets are a result of the fragmentation of partons after the scattering. Fragmentation functions give the probability for a parton to fragment into a particular hadron carrying a certain fraction (z) of the parton's energy. Fragmentation functions cannot be calculated in p-QCD and are extracted from experimental data.

3.1.2 Regge Theory

p-QCD is inadequate to describe soft processes, as a small momentum scale makes the coupling constant (α_s) large enough to make the higher order terms non-negligible, thus making the process intrinsically non-perturbative. Regge theory [38] is often used instead. The basic concept of Regge theory is that the amplitude of the hadron-hadron scattering is the sum of the contributions from all possible exchange particles with the appropriate quantum numbers. All such particles are said to lie on a *Regge trajectory* and obey the relation

$$J = \alpha_0 + \alpha' M_J^2, \tag{3.3}$$

where J and M_J are the spin and mass of the exchanged particle, α_0 is the *Regge intercept* and α' is the *Regge slope*. In Regge theory, the angular momentum is treated as a continuous complex variable $\alpha(t)$. However, resonances are only observed at physical values of spin, such that $\mathcal{R}e[\alpha(t)]$ is either an integer or a half-integer. An example of integer values of spin is seen in figure 3.2. The scattering amplitude behaves as if the hadrons had exchanged a single fictitious particle with an effective spin J given in [39] by

$$J = \alpha(t) = \alpha_0 + \alpha' t. \tag{3.4}$$

28

$\alpha(t)$ can be extracted from experimental data for negative values of t. This smoothly joins $\alpha(t)$ determined from masses of resonances (m^2) for positive values of t.
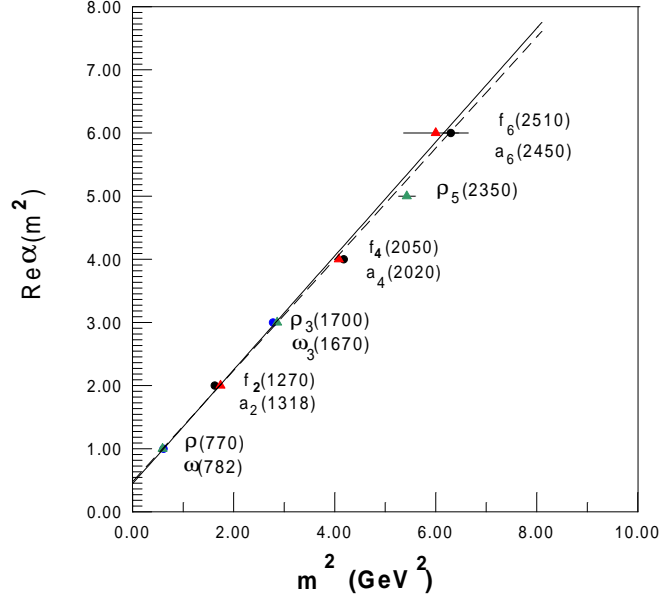
Figure 3.2: The spin J versus m^2 plot for various mesons and resonances taken from [40].

It can be shown in Regge theory that the total cross-section (σ_{tot}) for a hadron hadron collision depends on the CM energy $\sqrt{s}$ as

$$\sigma_{tot} \propto s^{\alpha_0 - 1}. \tag{3.5}$$

It was predicted in [41] and observed experimentally [42] that at very high energy the total cross-section in hadronic reactions approaches a constant value. This implies that the Regge intercept $\alpha_0 = 1$. It was also observed that the reactions were dominated by inelastic processes with no quantum number flow. The Regge trajectory with intercept $\alpha_0 = 1$ and with exchange particles that have vacuum quantum numbers is called the *Pomeranchuk trajectory* [1] [43]. The effective summation of particles on this trajectory is known as the *Pomeron* ($\mathbb{P}$). The particles on this trajectory are virtual and have the same internal quantum numbers as the vacuum. In QCD, the Pomeron is regarded as a colourless and flavourless multiple gluon state [44] or a glueball exchange.

---

[1] Named after Ukranian Soviet physicist Isaak Pomeranchuk.

Another type of exchange mediator, called the Reggeon $\mathbb{R}$ [45], is needed to successfully reproduce experimental data below the ISR [13] (introduced in section 1.3) energy ($\sqrt{s} = 63\,\text{GeV}$), as seen in figure 3.3. Thus, there are two types of exchange mediators: Reggeons and Pomerons. Reggeon exchange fits data at relatively low energies, while Pomeron exchange fits the data only at higher energies. Reggeons couple to the valence quarks of a proton, which carry a large fraction of the proton's momentum. At high energies, the incoming protons "pass by" so quickly that it is mainly the sea quarks that interact. The Pomeron couples to gluons (and sea quarks) which carry a small fraction of the proton's momentum. Already at ISR energies, the exchange mediator was predominantly the Pomeron. Thus, the higher the collision energy, the more important is the role of the Pomeron. The sum of these two trajectories describes the total pp cross-section.
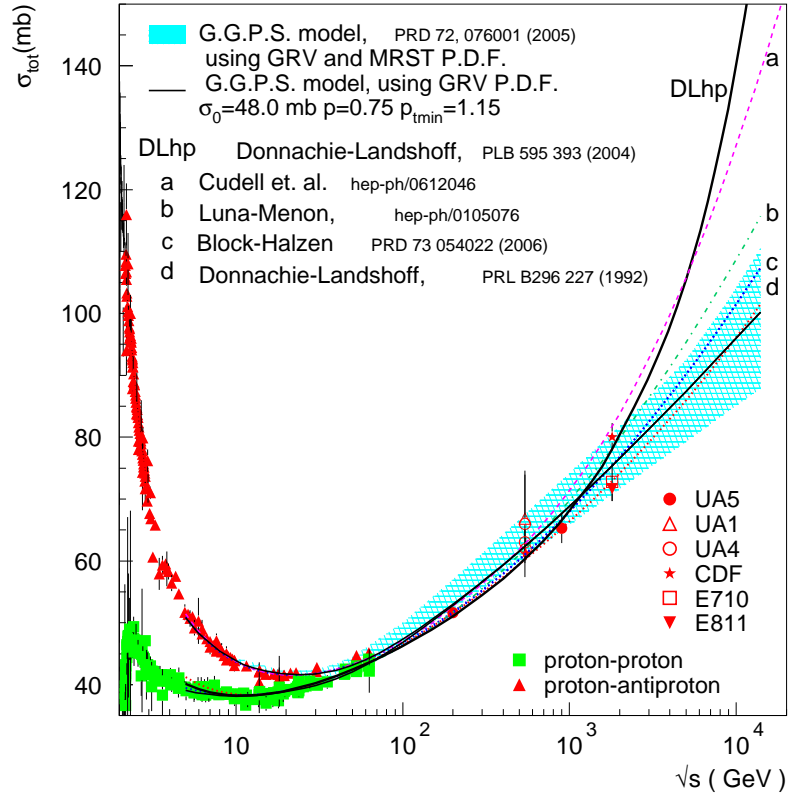
Figure 3.3: Data and model predictions for the total cross-section in pp and p$\bar{\text{p}}$ interactions taken from [42]. The Reggeon exchange corresponds to a power law with negative slope and describes data at low energies, while the Pomeron exchange leads to the power law with with positive slope and is needed to describe data at high energies.

3.1.3 Classification of hadron-hadron interactions

Colliding hadrons are colour singlets. As they approach each other, they may exchange a colour octet gluon, making each hadronic cluster a colour octet. To be able to separate into two separate

systems, they need to exchange another gluon and become colourless. As they move apart, colour lines that connect them are stretched. Given time, this system gets complex and multi-particle production occurs. In proton-proton (pp) (or more generally hadron-hadron) scattering, interactions are classified by the characteristics of the final states. Interactions can either be elastic or inelastic. In elastic scattering ($p_1 + p_2 \rightarrow p_1' + p_2'$), both protons emerge intact and no other particles are produced. The outgoing protons change direction but still appear in the forward [1] region as shown by the pink dots in figure 3.4. In figures 3.4 to 3.8, on the *x*-axis is pseudorapidity (η) and on the *y*-axis is ϕ, the angle made by the p_T vector with the vertical axis, shown in figure A1 in Appendix A. Elastic scattering can be achieved via the exchange of a glueball-like Pomeron. The LHC cross-section (at $\sqrt{s} = 14\,\text{TeV}$) for elastic scattering is estimated to be $\sim 30\,\text{mb}$ [46].
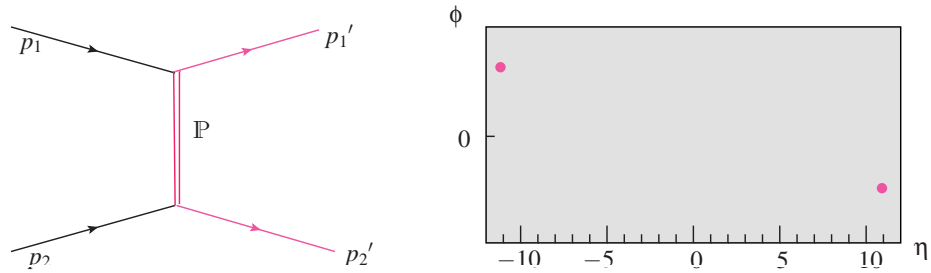
Figure 3.4: Diagram for elastic scattering and ϕ vs η plot showing the distribution of products after the interaction.

The exchange of gluons can excite a hadron. This can result in the outgoing state preserving the internal quantum numbers of the incoming particles but having a higher mass. This is known as quasi-elastic scattering. Interactions where the final state is not identical to the initial state are called inelastic.

Inelastic collisions can be diffractive or non-diffractive (ND). There are several possible descriptions of diffraction, allowing several alternative approaches. The approach discussed in this thesis is one described by Regge theory [38] in terms of the exchange of a Pomeron.

---

[1] Perpendicular to the beam axis the value of pseudorapidity (η) is equal to zero, increasing as the angle of the particle relative to the beam axis decreases. The "forward" direction refers to the regions of a detector close to the beam axis.

A diffractive reaction is one in which no internal quantum numbers (e.g. colour or charge) are exchanged between the colliding particles. Diffraction occurs when the exchanged Pomeron interacts with the proton to produce a system of particles referred to as the diffractive system (X). In diffractive scattering, the energy transfer between the two interacting protons remains small, but one or both protons dissociate into multi-particle final states with the same internal quantum numbers of the colliding protons.

If only one of the protons dissociates then the interaction is Single Diffractive (SD) ($p_1 + p_2 \rightarrow p'_1 + X_2$ or $p_1 + p_2 \rightarrow X_1 + p'_2$). The dissociated proton forms the diffractive system (X_1 or X_2) and is shown in figure 3.5 as a spray of blue dots (particles). The non-dissociated proton is shown as the pink dot. The LHC cross-section (at $\sqrt{s} = 14\,\text{TeV}$) for SD on both sides is estimated to be $\sim 10\,\text{mb}$ [46].
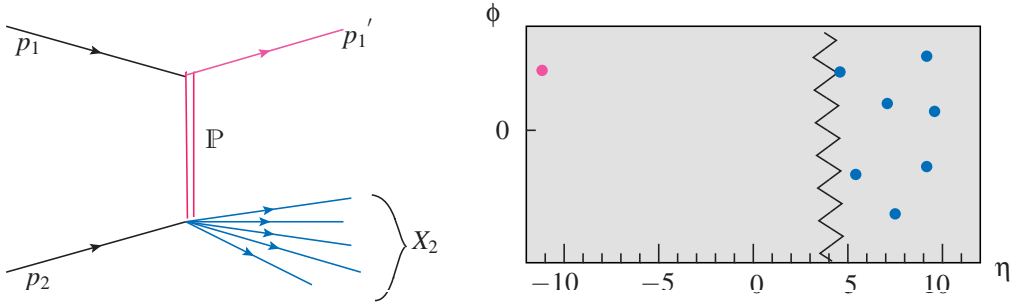
Figure 3.5: SD diagram and a window showing a pseudorapidity gap between $-10 < \eta < 3.5$.

If both the colliding protons dissociate, then the process is Double Diffractive (DD) ($p_1 + p_2 \rightarrow X_1 + X_2$) as seen in figure 3.6. Two diffractive systems X_1 and X_2 populate the forward regions, leaving a central unpopulated region in pseudorapidity. The LHC cross-section (at $\sqrt{s} = 14\,\text{TeV}$) for DD is estimated to be $\sim 7\,\text{mb}$ [46].

A different topology is possible with two Pomerons exchanged, namely Central Diffraction (CD) ($p_1 + p_2 \rightarrow p'_1 + X + p'_2$) or Double Pomeron Exchange. In this process, both the protons are intact and are seen in the final state (as two pink dots seen in figure 3.7). The LHC cross-section for CD is estimated to be $\sim 1\,\text{mb}$ [46]. In addition, there are interactions where many Pomerons
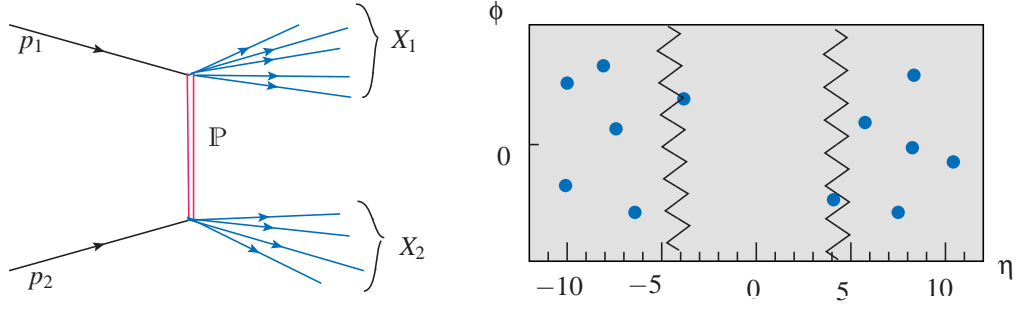
Figure 3.6: DD diagram and window showing a pseudorapidity gap between $-3.5 < \eta < 4$.

are exchanged. Such interactions are discussed again in section 3.2.1. The LHC cross-section for multi-Pomeron exchange is estimated to be $\ll 1\,\mathrm{mb}$ [46].
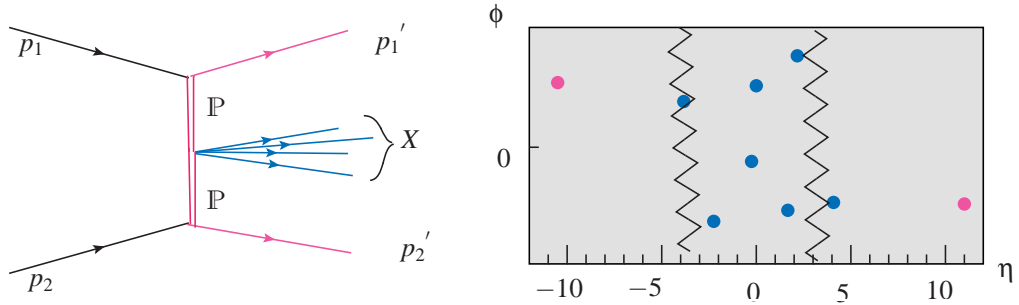
Figure 3.7: CD diagram and window showing two pseudorapidity gaps between $-10 < \eta < -4$ and $3 < \eta < 10$.

In Non-Diffractive (ND) interactions there is an exchange of colour charge and subsequently more hadrons are produced. This is shown in figure 3.8. ND interactions are the dominant process in pp interactions and are expected to be $\sim$58% of all interactions at the LHC with a cross-section estimated to be $\sim$65 mb (at $\sqrt{s} = 14\,\mathrm{TeV}$) [46].

Diffractive reactions are characterised by a large (non exponentially-suppressed) pseudorapidity gap in the final state. In other words, there is a large phase space separation between the outgoing proton and the diffractive system (or between the two diffractive systems in the case of DD) in which no particles are detected. A few ND events may also display a large pseudorapidity gap due to multiplicity fluctuations but their number is exponentially suppressed with increasing gap size. The probability density of a pseudorapidity gap $\Delta\eta$ is given by $\exp^{-\Delta\eta \frac{dN}{d\eta}}$, where $\frac{dN}{d\eta}$ is the pseudorapidity density. Those with $\Delta\eta > 3$ are mainly diffractive events [36].
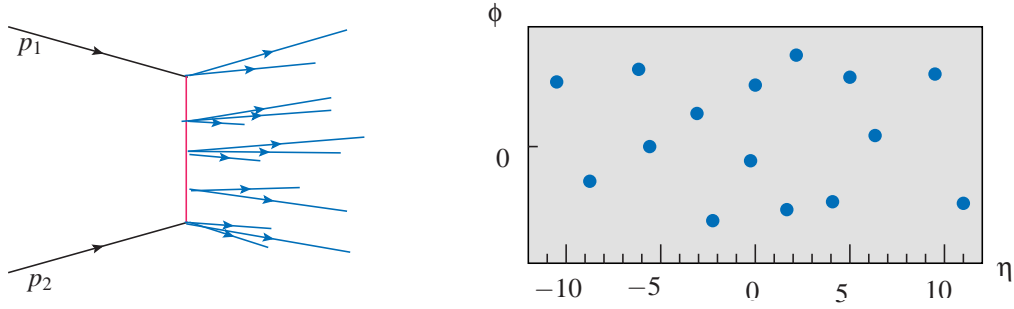
Figure 3.8: The diagram for an ND process. There are no pseudorapidity gaps.

To summarise, the total pp cross-section is given by

$$\sigma_{tot} = \sigma_{el} + \sigma_{inel} = \sigma_{el} + \sigma_{diff} + \sigma_{ND} \qquad (3.6)$$

where σ_{el}, σ_{inel}, σ_{diff} and σ_{ND} are the elastic, inelastic, diffractive and ND cross-sections respectively.

3.2 Monte Carlo Event Generators

The Monte Carlo (MC) [1] technique uses random numbers to solve problems. In a definition given by Halton [48], "the Monte Carlo method represents the solution of a problem as a parameter of a hypothetical population, using a random sequence of numbers to construct a sample of the population, from which statistical estimates of the parameter can be obtained". One of the main applications of MC calculations in high-energy physics is the integration of the relativistic phase space of multi-particle reactions.

Event generators produce hypothetical events in a simulated world with distributions predicted by theory to resemble real collisions. The objective is to provide, as accurately as possible, a representation of event properties in a wide range of reactions. Event generators in particle physics simulate particle collisions as they would be seen by a perfect detector. They are limited by our current understanding of the underlying physics and generally make use of both perturbative and

---

[1]The term Monte Carlo was coined in the 1940s by physicists working on the Manhattan project in the Los Alamos National Laboratory [47].

phenomenological approaches. By understanding how the original physics input is distorted at every stage in the better controlled simulated world, event generators help us understand the detector, trigger, data and background in the real world. Due to their extensive use of MC techniques, they are called MC event generators.

In an event generator the event is built in steps. For example, in a hadron-hadron interaction, the incoming hadrons have a partonic structure given by their PDF. A collision of partons from the incoming hadrons results in one of many processes. The randomised selection of process is governed by the cross-sections of various processes. The type of process selected determines the next steps. As an example, the following steps occur in a hard process.

When a collision occurs, the exchange of colour and charges can result in gluon or electromagnetic bremsstrahlung radiation. Emissions that are associated with the two incoming and colliding partons are called Initial-State Radiation (IsR). These are modelled by space-like parton showers. Those emissions associated with the outgoing partons after the collision are called Final-State Radiation (FsR). These are approximated by time-like parton showers.

In a collision of two hadrons, there is a possibility that more than one pair of partons could collide, giving rise to multiple interactions (MI), each associated with its own IsR and FsR. Those partons that do not collide form the beam remnants. While a fraction of the energy of the incoming hadrons is taken away by the colliding partons, most of the incoming energy remains in the beam remnants. The beam remnants continue to travel in their original direction, and carry colour to compensate for that taken away by the colliding partons.

With time of the order of fm/c, partons move away from each other and QCD confinement forces begin to act. The time evolution of confinement forces is not known from first principles, and, often, models are used. One such approach is called the Lund model [49], in which confinement fields are modelled as strings that are stretched between each colour and its anti-colour. As the partons move apart, the potential energy in the string increases, eventually breaking the string and producing a new quark-antiquark pair (or a diquark-antidiquark pair) at the point of break-

age. The two resulting strings continue to fragment until the energy of the string is too small for further fragmentation. The resulting pieces of strings are mesons. Similarly, baryons are formed by diquark-antidiquark pairs being produced at the point of breakage. Baryons (and sometimes mesons) can also be produced by the *popcorn* mechanism [50] from the successive production of several q$\bar{\text{q}}$ pairs. The formation of hadrons as a result of string fragmentation is called hadronisation. While only some of these hadrons live long enough to be visible in a detector, many are unstable and decay at different time scales. The final products seen in a detector depend on their branching ratios, decay products and life-times.

A broad range of physics processes is described by MC event generators. Only some of them are known from first principles, while others are modelled in different frameworks. Hence, a comparison of different models is necessary. The MC event generators described and used in this thesis are PHOJET [12] and different versions of PYTHIA [11].

3.2.1 PHOJET

PHOJET [12] is a MC event generator that was developed for detailed modelling of minimum bias events with a superposition of various types of diffractive and non-diffractive particle production processes. It uses a physics model that combines the ideas of the Dual Parton Model (DPM) [51, 39] with pQCD. PHOJET is formulated as a two-component model where the dominant soft processes are described by the DPM, and pQCD is applied to generate hard interactions.

Event generation

Hadronic interactions in PHOJET are assumed to be described by the exchange of a single effective Pomeron. Processes are classified as hard and soft based on the transverse momenta of intermediate state partons. Partons in soft processes have momenta $p_T < p_T^{\text{cut-off}}$, while in hard processes at least one large momentum transfer with $p_T > p_T^{\text{cut-off}}$ exists. The transition between the soft and hard regions at this scale is achieved by a unitarisation scheme discussed below. Physical cross-sections are calculated by normalising Born amplitudes, which are the sum of soft and

hard sub-amplitudes. This allows the use of the parton model for hard interactions along with Regge theory for soft interactions. The contribution of each component at a particular energy depends on the value of $p_T^{\text{cut-off}}$. When $p_T^{\text{cut-off}} \gg \Lambda_{\text{QCD}}$, the hard cross-section is calculated within the parton model described in section 3.1.1. The lowest order pQCD process is described by the *hard* part of the Pomeron, while the remaining soft part is described by a *soft* Pomeron and an effective Reggeon. Soft cross-sections are parameterised by

$$\sigma_{A,B}^{\mathbb{P}} = g_{A,\mathbb{P}}(0) g_{B,\mathbb{P}}(0) \left(\frac{s}{s_0} \right)^{\Delta_{\mathbb{P}}} \tag{3.7}$$

and

$$\sigma_{A,B}^{\mathbb{R}} = g_{A,\mathbb{R}}(0) g_{B,\mathbb{R}}(0) \left(\frac{s}{s_0} \right)^{\Delta_{\mathbb{R}}} \tag{3.8}$$

where $\Delta_{\mathbb{P}} = \alpha_{\mathbb{P}}(0) - 1$ and $\Delta_{\mathbb{R}} = \alpha_{\mathbb{R}}(0) - 1$. $\alpha_{\mathbb{P}}(0)$ and $\alpha_{\mathbb{R}}(0)$ are the Pomeron and Reggeon intercepts respectively and s and s_0 are the energy scale and a reference energy scale respectively. $g_{A,\mathbb{P}}(0)$ and $g_{B,\mathbb{P}}(0)$ ($g_{A,\mathbb{R}}(0)$ and $g_{B,\mathbb{R}}(0)$) are the couplings of the Pomeron (Reggeon) to particles A and B respectively. The intercepts are effective parameters that depend on the value of $p_T^{\text{cut-off}}$ and on the PDFs used in the calculation of the hard part. However, the couplings and intercepts are adjusted in such a way that the total cross-section obtained by summing the soft and hard cross-sections is independent of $p_T^{\text{cut-off}}$ for $p_T^{\text{cut-off}} \geq 2\,\text{GeV/c}$.

Unitarisation   While both the soft and hard cross-sections calculated from the Born-graph amplitudes increase like powers of s, the total cross-section σ_{tot} increases slower than $(\ln s)^2$ [52]. At high energies, the soft and hard Born-graph cross-sections exceed the total cross-section making unitarity corrections more important in this region. Within Regge theory unitarity corrections are achieved with multiple Pomeron exchange, allowing more than one soft or hard interaction in the same event. As a consequence average multiplicities of hard and soft interactions increase. Model predictions are compared to cross-section data to determine the unknown parameters of the model.

In ND events below the $p_T^{\text{cut-off}}$ the transverse momentum transfer p_T of partons is sampled from

an exponential distribution given by

$$\frac{dN_{\text{soft}}}{dp_T} \sim p_T \exp(-\beta m_T) \tag{3.9}$$

where $m_T = \sqrt{m_\pi^2 + p_T^2}$, whereas above $p_T^{\text{cut-off}}$ the momentum transfer t is obtained from pQCD. The slope parameter β is fixed in such a way that there is a smooth transition between the soft and hard parts giving

$$\left.\frac{dN_{\text{soft}}}{dp_T}\right|_{p_T=p_T^{\text{cut-off}}} = \left.\frac{dN_{\text{hard}}}{dp_T}\right|_{p_T=p_T^{\text{cut-off}}}. \tag{3.10}$$

Diffractive interactions

In diffractive events the mass of the diffractive system (M_X) is sampled from cross-sections calculated with the triple-Pomeron approximation [53], derived from Regge theory with the assumption that $s \gg M_X^2$ and $M_X^2 \gg t$. The lower limit on the diffractive mass is given by

$$M_{X,\text{min}}^2 = (m_A + m_\pi)^2 \tag{3.11}$$

where m_A is the mass of the diffractively dissociated particle and m_π is the mass of the pion. The upper limit on the diffractive mass is given by the coherence condition

$$M_{X,\text{max}}^2 = (m_\pi/m_B)s \tag{3.12}$$

where m_B is the mass of the elastically deflected particle. Momentum transfer is sampled from an exponential slope that depends on the masses of the incoming and outgoing particles and the diffractive system.

The multi-particle final state in diffraction is generated by simulating Pomeron-hadron and Pomeron-Pomeron (in the case of CD) interactions within the framework of the DPM used in ND scattering, with $\sqrt{s} = M_X$, by assigning the Pomeron a PDF.

PHOJET allows initial and final state parton showers, described in section 3.2. Fragmentation of soft chains by cutting of Pomerons and of hard scattered partons is as prescribed by the Lund

string model [49]. Only a few parameters including the $p_T^{\text{cut}-\text{off}}$ and the proton-Pomeron and proton-Reggeon couplings are tunable by fits to experimental data. The version of PHOJET used in this thesis is PHOJET1.12 tuned to the minimum bias data from CDF at 1800 GeV [54].

3.2.2 PYTHIA 6

PYTHIA 6 [11] is a MC event generator frequently used in high-energy physics. It combines pQCD to describe hard processes with phenomenological models to describe soft processes. A tunable cut-off parameter $p_{\text{T,min}}$, similar to PHOJET, connects the two components. Hard inter-actions are those with a momentum transfer greater than $p_{\text{T,min}}$.

PYTHIA 6, as we see it today, is a product of nearly 33 years of development that includes several components of JETSET [55]. The development of series 6 of PYTHIA, written in Fortran 77, began in 1997. Although there was significant development from one version to the next, the description of diffraction remained the same in the two versions 6.2 and 6.4.

In this section a description of the diffractive processes in PYTHIA 6 is presented.

Event Generation

The total hadronic cross-section for $AB \rightarrow$ anything, $\sigma_{\text{tot}}^{\text{AB}}$ is calculated using the Donnachie and Landshoff parameterisation [56]. In this approach, the total cross-section appears as a sum of a Pomeron term and a Reggeon term given by

$$\sigma_{\text{tot}}^{\text{AB}}(s) = X^{\text{AB}} s^{\varepsilon} + Y^{\text{AB}} s^{-\eta} \tag{3.13}$$

where X^{AB} and Y^{AB} are the Pomeron and Reggeon couplings to the incoming hadrons. The powers ε for the Pomeron term and η for the Reggeon term are expected to be universal with $\varepsilon = 0.0808$ and $\eta = 0.4525$ [56], while the coefficients X^{AB} and Y^{AB} are specific to each initial state. In the case of pp and p$\bar{\text{p}}$ interactions, $X^{\text{pp}} = X^{\text{p}\bar{\text{p}}} = 21.70$ mb, while $Y^{\text{pp}} = 56.08$ mb and $Y^{\text{p}\bar{\text{p}}} = 98.39$ mb [56] and s is in GeV^2.

$$\sigma_{\text{tot}}^{\text{pp}} = 21.70 s^{0.0808} + 56.08 s^{-0.4525} \tag{3.14}$$

$$\sigma_{\text{tot}}^{\text{p}\bar{\text{p}}} = 21.70 s^{0.0808} + 98.39 s^{-0.4525}. \tag{3.15}$$

The Pomeron couplings to the proton and antiproton are identical because the Pomeron carries vacuum quantum numbers. Hence $\sigma_{\text{tot}}^{\text{pp}}$ and $\sigma_{\text{tot}}^{\text{p}\bar{\text{p}}}$ have the same coefficient for the Pomeron term in equations (3.14) and (3.15) [56]. A consequence of the Pomeron hypothesis is that the cross-sections of pp and p$\bar{\text{p}}$ diffractive scattering should be equal at high enough energies [56].

Cross-sections for elastic, single and double diffractive events are included, but higher diffractive topologies like central diffraction are neglected. The diffractive cross-sections and event characteristics are described by a model of Schuler and Sjöstrand [57, 58]. The elastic cross-section is obtained from the optical theorem and the ND cross-section is given by "whatever is left" as shown in equation (3.16), where σ_{tot} is given by equation (3.13):

$$\sigma_{\text{ND}} = \sigma_{\text{tot}} - \sigma_{\text{el}} - \sigma_{\text{SD}} - \sigma_{\text{DD}}. \tag{3.16}$$

In the Schuler-Sjöstrand model, diffractive cross-sections have an inverse dependence on the square of the diffractive mass (M_X^2) and an exponential dependence on t. Diffractive cross-sections are given by

$$\frac{d^2\sigma_{\text{sd(AB}\to\text{XB)}}(s)}{dtdM_X^2} = \frac{g_{3\mathbb{P}}}{16\pi}\beta_{\text{A}\mathbb{P}}\beta_{\text{B}\mathbb{P}}^2\frac{1}{M_X^2}\exp(B_{\text{sd(XB)}}t)F_{\text{sd}} \tag{3.17}$$

$$\frac{d^3\sigma_{\text{dd}}(s)}{dtdM_{X_1}^2 dM_{X_2}^2} = \frac{g_{3\mathbb{P}}^2}{16\pi}\beta_{\text{A}\mathbb{P}}\beta_{\text{B}\mathbb{P}}\frac{1}{M_{X_1}^2}\frac{1}{M_{X_2}^2}\exp(B_{\text{dd}}t)F_{\text{dd}}. \tag{3.18}$$

The couplings β are related to the Pomeron term of equation (3.13). The triple Pomeron coupling $g_{3\mathbb{P}}$ is determined from single diffractive data. The exponential slope parameters $B_{\text{sd or dd}}$ are assumed to have a logarithmic dependence on $1/M^2$. The diffractive mass spectrum M ranges from $0.28\,\text{GeV}$ ($\approx 2m_\pi$) above the mass of the diffracted hadron, to the kinematic limit. The

kinematic range of t depends on the masses of all incoming and outgoing systems involved. Diffractive cross-sections in PYTHIA 6 are integrated for a set of CM energies, starting at 10 GeV. The results have been parameterised in section 4 of the PYTHIA 6 manual [58]. Once the process is selected using this parameterisation, M and t are generated using equations (3.17) and (3.18). These Regge formulae for diffraction are supposed to hold in certain asymptotic regions of the full phase space. Due to the lack of a theory that predicts differential cross-sections at arbitrary t and M^2 values, the Regge formulae above are used everywhere along with factors F_{sd} and F_{dd} in equations (3.17) and (3.18) to give a sensible behaviour in the full phase space. These factors suppress production close to the kinematical limit and in the case of double diffraction, also suppress configurations where the two diffractive systems overlap in rapidity space. These factors also give a broad enhancement in the production rate in the resonance region up to about 2 GeV as seen in figure 4.2. This gives a smeared-out version of exclusive states, rather than listing them all out individually.

Particle Production

Once the process is selected and the kinematic variables are determined, the products of the collision are generated. The handling of this production depends on the value of the diffractive mass M_X. If $M_X - M_A \leq 1$ GeV, where M_A is the mass of the incoming particle, the system is allowed to decay isotropically to a two-body system. For a more massive diffractive state, the system is treated as a string with the quantum numbers of the original hadron. Two alternative ways of stretching the string are considered.

There is both a gluonic and a quark contribution. When an incoming hadron is diffractively excited, either a valence quark or a gluon is "kicked out" of it. If the Pomeron couples to a valence quark from the non-diffracted proton, the string (the pink dashed lines in figure 3.9) is stretched between the struck quark and the remnant diquark (or antiquark) of the diffractive system, seen in figure 3.9(a). This configuration dominates at small M_X. The alternative is when the interaction is with a gluon from the non-diffracted proton. The string is stretched from a quark in the diffractive state to a gluon, and then back to a diquark (or antiquark). This gives rise to a "hair-pin" structure as seen in figure 3.9(b). In PYTHIA 6 the ratio of the two contributions can be changed.

41
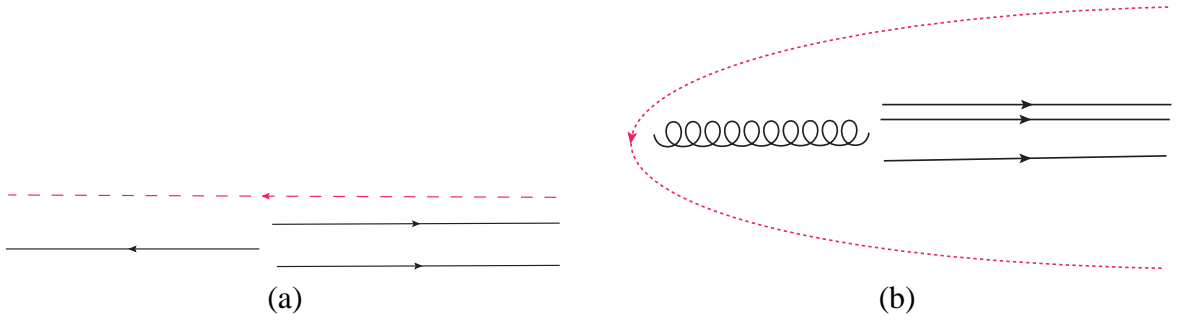
Figure 3.9: String being stretched in diffractive processes - (a) $\mathbb{P}$ couples to a valence quark and (b) $\mathbb{P}$ couples to a gluon.

3.2.3 PYTHIA 6.214 vs PHOJET 1.12

PYTHIA 6 and PHOJET, as described, have some similarities and differences, especially in modelling diffraction. While both the generators combine pQCD to describe hard interactions, and phenomenological models for soft interactions, the models they employ are different. PHOJET relies on the dual parton model [51], while PYTHIA 6 is based on the Schuler-Sjöstrand model [57, 58]. PHOJET models interactions with multiple Pomerons being exchanged. This is one of the reasons for the difference in the SD and DD cross-section values predicted by PHOJET and PYTHIA 6. In addition, unlike in PYTHIA 6, CD with double Pomeron exchange is included in PHOJET. Another important difference in the modelling of diffractive events is that, in PYTHIA 6, hard collisions between Pomerons and protons are not permitted. These differences in modelling lead to the difference seen in properties of the final state particles.

A study comparing the pseudorapidity (η), charged particle density ($dN_{ch}/d\eta$) and transverse momentum (p_T) distributions in PYTHIA 6.214 and PHOJET 1.12 at CM energy 7 TeV is shown below. ND and SD spectra are compared to analyse the difference in the diffractive part.

A comparison of figures 3.10(a) with 3.10(b) and 3.11(a) with 3.11(b) shows that although the multiplicity spectra for ND events in PYTHIA 6 and PHOJET are similar, high multiplicity SD events are not generated by PYTHIA 6. The average multiplicity of SD events produced
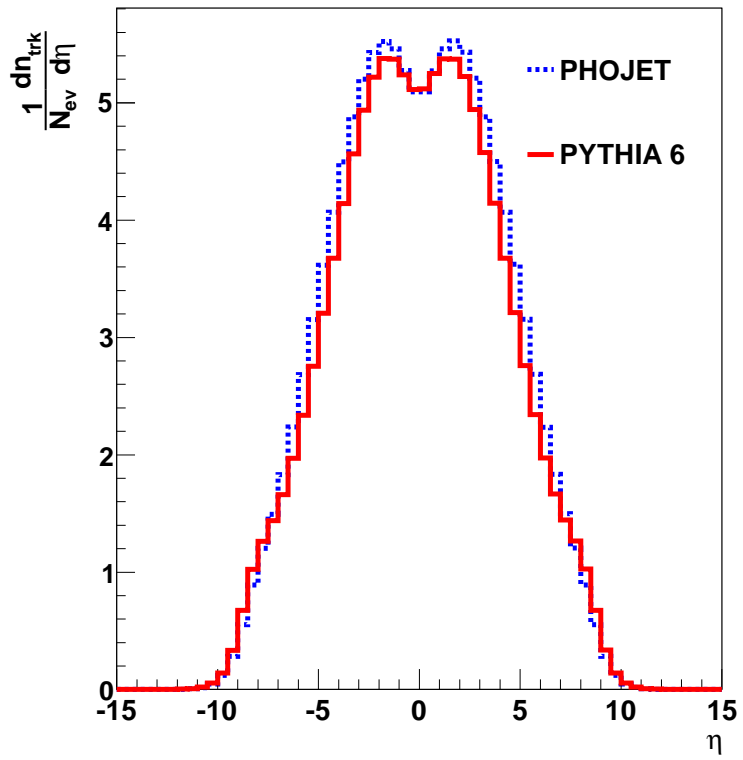
(a)

(b)
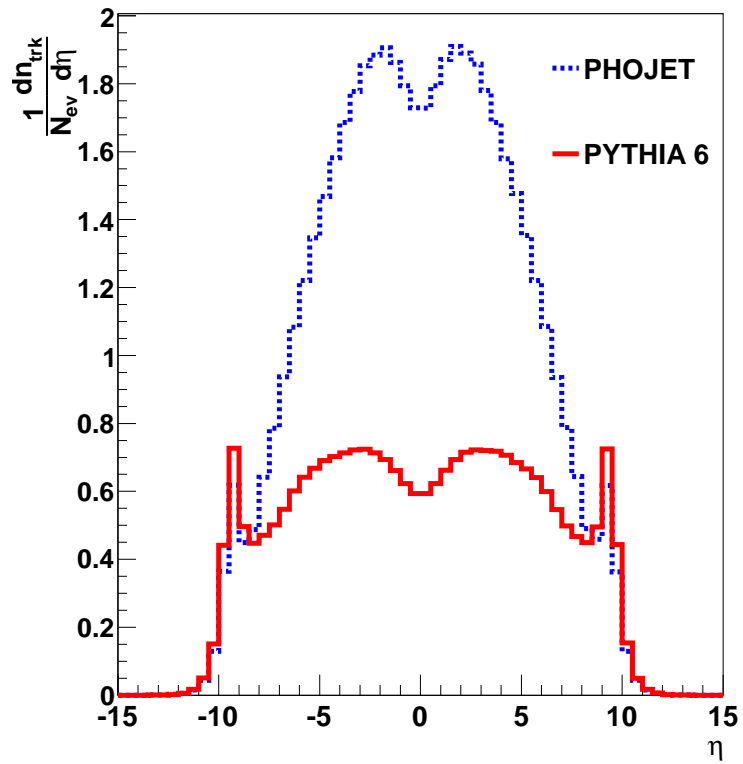
Figure 3.10: η distributions for (a) ND and (b) SD events at 7 TeV comparing PYTHIA 6 and PHOJET. The plot shows events where either one of the incoming protons dissociates.
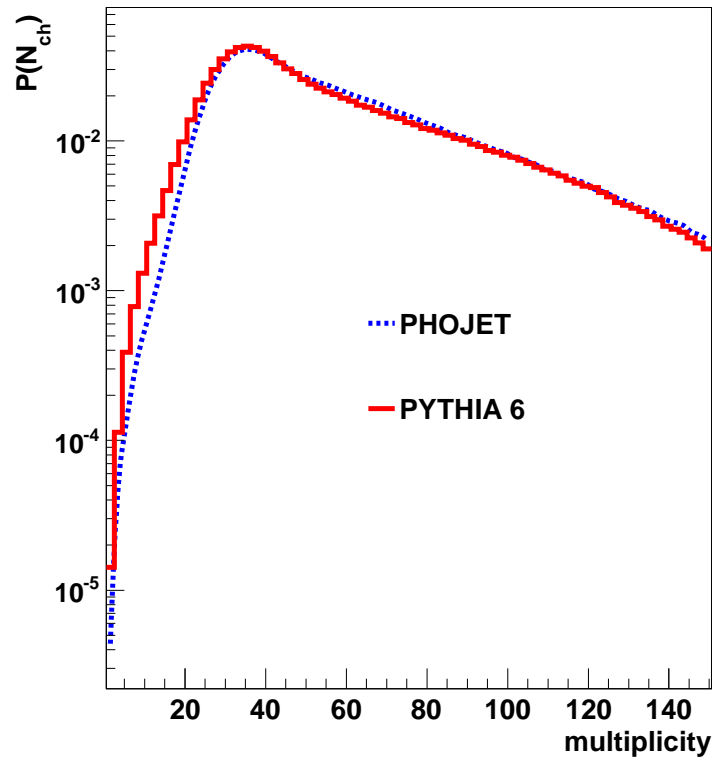
(a)
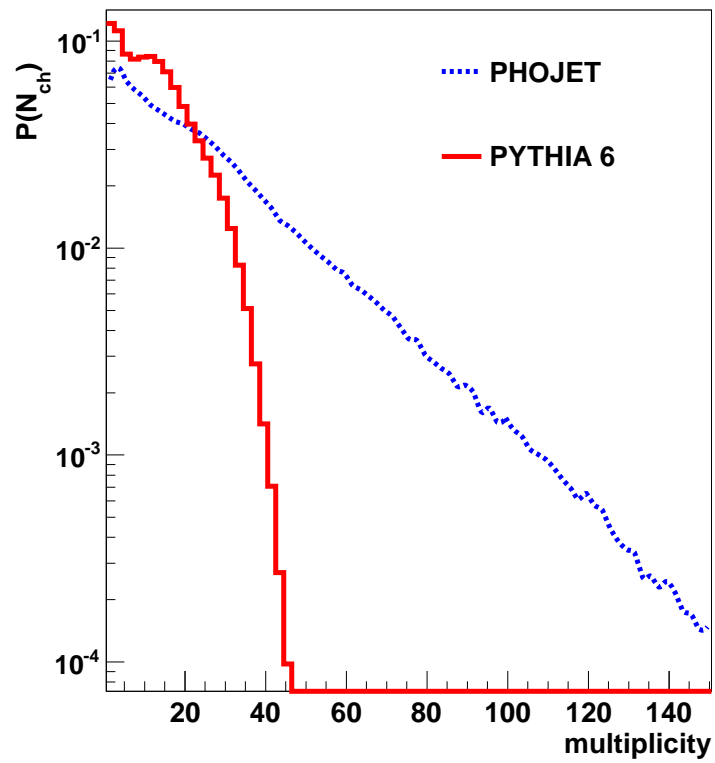
(b)

Figure 3.11: Multiplicity distributions for (a) ND and (b) SD events at 7 TeV comparing PYTHIA 6 and PHOJET in all phase space.
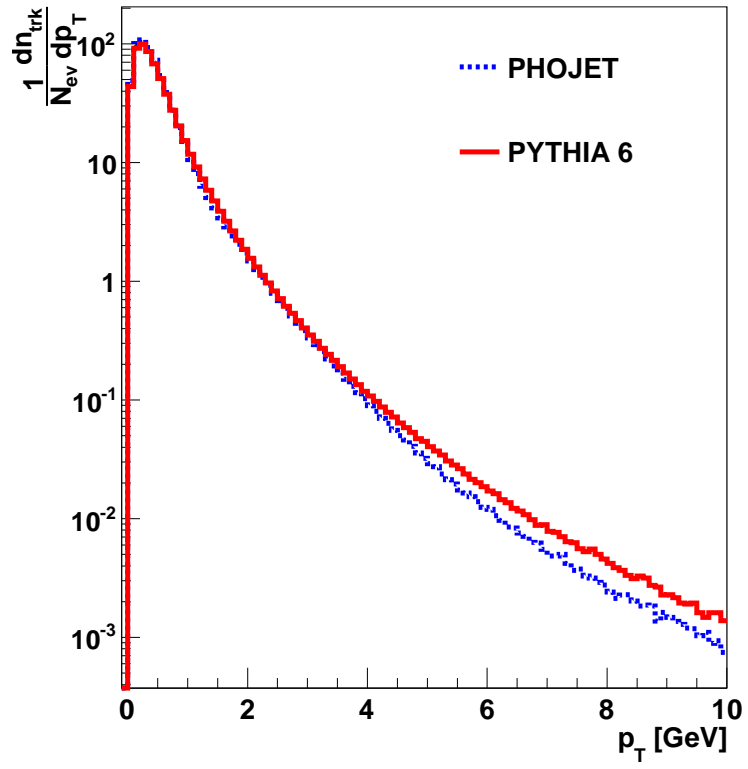
(a)
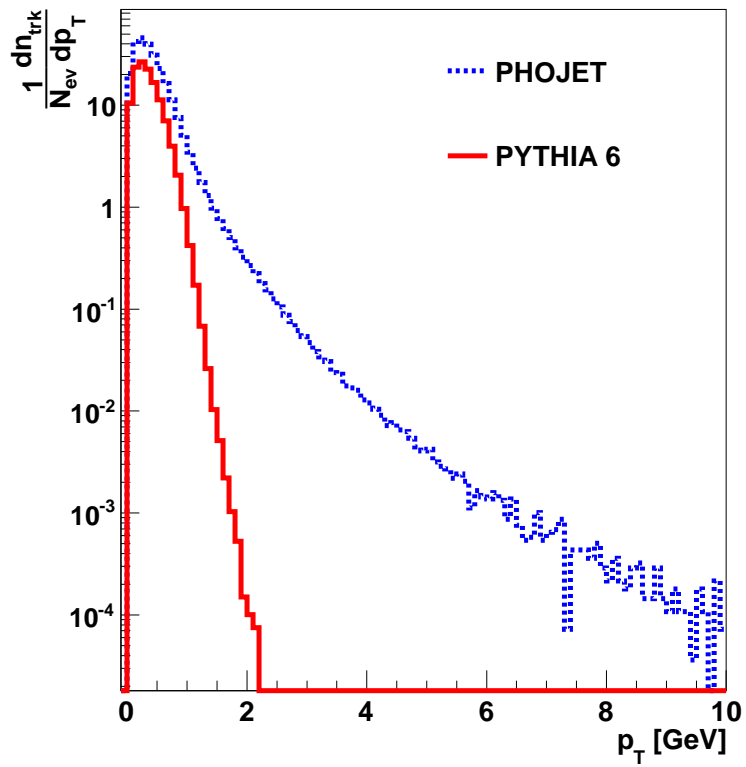
(b)

Figure 3.12: p_T distributions for (a) ND and (b) SD events at 7 TeV comparing PYTHIA 6 and PHOJET.

in PYTHIA 6 is lower than that in PHOJET, seen in both figures 3.10 and 3.11. Similarly, the p_T spectra in figures 3.12(a) and 3.12(b) show that PYTHIA 6 lacks a hard diffractive part.

3.3 Summary

The standard model of particle physics describes elementary particles and their interactions. Strong interactions are mediated by gluons, which can self-interact. This feature is what differentiates the theory of strong interactions from electromagnetism. As a consequence of self-interaction of the gluon, quarks are always observed as colourless combinations. However, when the distance between two quarks approaches zero, quarks behave like free non-interacting particles. The scale at which this behaviour is observed is called the QCD scale.

For interactions having a momentum transfer above the QCD scale, perturbative QCD can be used to factorise a hadron-hadron scattering cross-section as the product of the parton density functions of the incoming hadrons and the parton-parton interaction cross-section. For interactions with a momentum transfer below the QCD scale, phenomenological models are used. One such model is based on Regge theory which says that all possible exchange particles in a hadron-hadron scattering lie on a Regge trajectory given by the spin and mass of the exchange particle. Observed particles are those particles on the Regge trajectory with physical values of spin. The Pomeron is the Regge trajectory with intercept 1. The particles on this trajectory would have vacuum quantum numbers. In order to describe the total cross-section, a Pomeron trajectory is used. Experimental data is successfully described with a Pomeron trajectory and a Reggeon trajectory.

Hadron interactions are also classified, based on their final states, as either elastic or inelastic. Elastic collisions preserve the incoming hadrons while inelastic collisions do not. Inelastic collisions can be diffractive or non-diffractive. Diffractive interactions are those with no exchange of colour. Diffractive interactions can be single diffractive, double diffractive or central diffractive depending on the number of exchanged Pomerons and the topology of the final state. Diffractive events are characterised by a large rapidity gap in the final state. Non-diffractive events are interactions with an exchange of colour charge and subsequently more hadrons are produced.

46

Monte Carlo event generators use the concept of random sampling along with inbuilt theoretical and phenomenological models to provide a representation of event properties in a wide range of reactions. Two Monte Carlo event generators PYTHIA 6 and PHOJET have been described. They both employ a hard and soft component for interactions, and use similar models for hadronisation. However they differ in the way cross-sections are calculated and on the phenomenological models they use. In the description of diffraction, there are several noticable differences. The invariant mass distributions of diffractive system are considerably different (see figure 4.2 in the following chapter). PHOJET encodes central diffraction which PYTHIA 6 lacks. Additionally, diffraction is better described in PHOJET than in PYTHIA 6 because PHOJET models hard diffraction as hard collisions between a Pomeron and a hadron. This explains the low p_T and multiplicity fall-off seen in PYTHIA 6. An improvement in the diffractive part is achieved by adding a hard diffractive component to PYTHIA 8, which is described in the next chapter.

DIFFRACTION IN PYTHIA 8

Experimentally, single diffractive reactions are characterised by a large (non-exponentially-suppressed) rapidity gap in the forward region. In other words, there is a large separation in rapidity between the quasi-elastically scattered proton and the diffractive system, in which no particles are detected. A few ND events may also display a large rapidity gap due to multiplicity fluctuations but their number is exponentially suppressed with increasing rapidity gap.

Based on the description of the Pomeron and its interaction with the proton, a model for diffraction has been constructed and implemented in PYTHIA 8. Pomeron-proton collisions are modelled at a reduced CM energy which is the invariant mass of the diffractive system (M_X^2); then fully integrated into PYTHIA 8 in such a way that the standard PYTHIA 8 machinery for multiple interactions, parton showers and hadronisation is used. This is the approach pioneered in the POMPYT program [59] and has been fully included in PYTHIA 8 [60].

The chapter starts with a description of the framework of hard diffraction, the concept of a Pomeron flux and diffractive PDFs. This is followed by a description of how the choice of hard or soft machinery in diffraction is made in PYTHIA 8 and of particle production. The next section shows a comparison of the p_T, pseudorapidity and multiplicity spectra of diffractive events generated by PYTHIA 6, PYTHIA 8 and PHOJET. Finally, the free parameters in the description of hard diffraction in PYTHIA 8 are varied, and their effect on the average multiplicity is studied.

4.1 Hard Diffraction Kinematics

In a QCD approach, a partonic description of a Pomeron, as described in [61] is commonly used. Different factorisations of the partonic structure of the Pomeron exist. The model for diffractive hard scattering used in this work is described in detail in [62]. In this approach, firstly a Pomeron is emitted from a proton i (at the upper vertex in figure 4.1) in a soft process, with a momentum transfer squared given by

$$t = (p_i - p_i')^2 \tag{4.1}$$

where p_i and p_i' are the 4-momenta of the incoming and the scattered protons. Then this emitted Pomeron interacts with the other proton, j, at the lower vertex, in a hard process, with a transfer of momentum between constituent partons. The system X that is produced in this interaction is called the diffractive system. The invariant mass of the diffractive system X, also known as the diffractive mass, is given in terms of the proton four momenta by

$$M_X^2 = (p_i + p_j - p_i')^2. \tag{4.2}$$
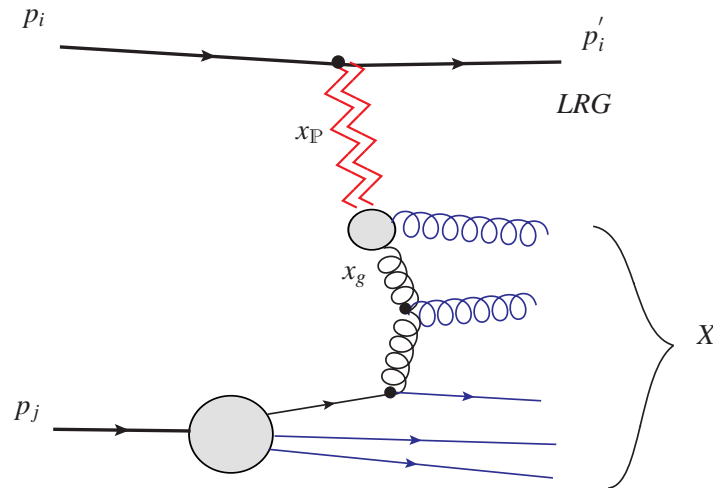
Figure 4.1: Exchange diagram for single diffraction.

There is a large rapidity gap (LRG) between the out-going proton and diffractive system X. The above introduces the concept of a Pomeron flux in a proton $f_{\mathbb{P}/p}(x_{\mathbb{P}}, t)$ (in this case $f_{\mathbb{P}/p_i}(x_{\mathbb{P}}, t)$), where $x_{\mathbb{P}}$ is the fraction of the proton's momentum carried by the emitted Pomeron. The Pomeron

flux describes the probability that a Pomeron with a given value of $x_\mathbb{P}$ and t couples to the proton. In analogy with DIS, described in chapter 3, the concept of diffractive PDFs (DPDFs) is defined (see section 4.2). DPDFs can be interpreted as conditional probabilities to find a parton with a given fraction of the Pomeron's momentum when probed at a given resolution.

In the massless limit (neglecting the proton and Pomeron masses; $t \to 0$),

$$x_\mathbb{P} = \frac{E_\mathbb{P}}{E_p} = \frac{|\vec{p}_\mathbb{P}|}{|\vec{p}_p|} \tag{4.3}$$

where $E_\mathbb{P}$ and E_p are the energy of the Pomeron and of the proton to which it was coupled respectively. In this limit, the fraction $x_\mathbb{P}$ of the proton's momentum carried by the Pomeron can be expressed as

$$x_\mathbb{P} = M_X^2/s. \tag{4.4}$$

The fraction $x_{g(or q)}$ of the Pomeron's momentum carried by its constituent gluon (g) (or quark (q)) is given by

$$x_{g \text{ (or q)}} = \frac{E_{g \text{ (or q)}}}{E_\mathbb{P}}, \tag{4.5}$$

where E_g (E_q) is the energy of the gluon (quark).

The diffractive hard pp scattering cross-section can be written as

$$\frac{d\sigma(pp \to p + X)}{dx_\mathbb{P} dt dx_1 dx_2 d\hat{t}} = \underbrace{f_{\mathbb{P}/p}(x_\mathbb{P}, t)}_{\mathbb{P}\text{flux}} \frac{d\sigma(p\mathbb{P} \to X)}{dx_1 dx_2 d\hat{t}}. \tag{4.6}$$

Here x_1 and x_2 are the fraction of the proton's and Pomeron's momenta carried by a quark (x_q) or a gluon (x_g) and $\hat{t}$ is the momentum transfer between the partons. The second term in equation (4.6) is the proton-Pomeron hard scattering differential cross-section. In analogy with DIS described in section 3.1.1, the Pomeron-proton hard scattering differential cross-section is assumed to factorise as

$$\frac{d\sigma(p\mathbb{P} \to X)}{dx_1 dx_2 d\hat{t}} = f_{p_1/p}(x_1, Q^2) f_{p_2/\mathbb{P}}(x_2, Q^2) \frac{d\hat{\sigma}}{d\hat{t}}. \tag{4.7}$$

Here, $f_{p_1/p}(x_1, Q^2)$ and $f_{p_2/\mathbb{P}}(x_2, Q^2)$ are the proton and Pomeron PDFs with partons p_1 and p_2 having momentum fractions x_1 and x_2 of the proton and Pomeron respectively. $d\hat{\sigma}/d\hat{t}$ is the corresponding hard scattering cross-section for that sub-process. Because of the inherent non-perturbative effect in a QCD binding state, PDFs (and DPDFs) cannot be obtained by perturbative QCD from first principles. The known PDFs (and DPDFs) are instead obtained by using fits to experimental data and extrapolated in Q^2 using the DGLAP equations [63], which describe the evolution of PDFs with scale Q^2.

To describe the dampening of the perturbative jet cross-section at $p_T \to 0$ by colour screening, the actual cross-section ($\frac{d\hat{\sigma}}{d\hat{t}}$) is multiplied by a regularisation factor

$$\frac{d\hat{\sigma}}{d\hat{t}} \to \frac{d\hat{\sigma}}{d\hat{t}} \frac{p_T^4}{(p_{T0}^2 + p_T^2)^2}. \tag{4.8}$$

p_{T0} is a free, tunable parameter of the order 2-4 GeV. The energy dependence of p_{T0} is given by

$$p_{T0}(E_{\mathrm{CM}}) = p_T(E_{\mathrm{CM}}^{Ref}) \left(\frac{E_{\mathrm{CM}}}{E_{\mathrm{CM}}^{Ref}}\right)^{E_{\mathrm{CM}}^{Pow}}, \tag{4.9}$$

where E_{CM} is the current energy scale, E_{CM}^{Ref} is an arbitrary reference energy at which $p_T(E_{\mathrm{CM}}) = p_{T0}(E_{\mathrm{CM}}^{Ref})$ is defined. E_{CM}^{Pow} controls the pace at which $p_{T0}(E_{\mathrm{CM}})$ scales with energy. The larger the value of E_{CM}^{Pow}, the quicker $p_{T0}(E_{\mathrm{CM}})$ scales with energy. Note that this regularisation is common to both the diffractive and the non-diffractive parts of PYTHIA 8.

4.1.1 Pomeron flux parameterisations

Diffractive cross-sections are determined using the Schuler-Sjöstrand model (equation 3.17) in exactly the same way as described in section 3.2.2. Once a diffractive event has been chosen, the Pomeron flux determines the M_X^2 and t distributions. In addition to the Schuler-Sjöstrand model discussed above, three other parameterisations of the Pomeron flux have been implemented in PYTHIA 8. The Schuler-Sjöstrand model is currently the only one which provides a separate t spectrum for DD.

1. Bruni and Ingelman [64] parameterisation: it has a mass spectrum close to $1/M_X^2$. The t dependence of the Pomeron flux distribution is the sum of two exponentials, given by

$$f_{\mathbb{P}/p}(x_\mathbb{P}, t) = \frac{1}{4.6 x_\mathbb{P}} (6.38 e^{-8|t|} + 0.424 e^{-3|t|}). \qquad (4.10)$$

2. Berger *et al.* [65] and Streng [66] parameterisation: it uses a Pomeron description but with values from the RAPGAP manual [67]. This gives a stronger peak towards low-mass diffractive states. The t dependence has two factors, one of which is exponential and the other is a power of $x_\mathbb{P}$. This parameterisation is given by

$$f_{\mathbb{P}/p}(x_\mathbb{P}, t) = \frac{\beta_{\mathbb{P}/p}^2(0)}{16\pi} x_\mathbb{P}^{1 - 2\alpha_\mathbb{P}(t)} e^{-b_0 |t|}. \qquad (4.11)$$

Here $b_0 = 4.7\,\mathrm{GeV}^{-2}$ is the diffractive slope parameter, $\alpha_\mathbb{P}(t) = \alpha_\mathbb{P}(0) + \alpha_\mathbb{P}' t$ describes the Pomeron trajectory, with intercept $\alpha_\mathbb{P}(0) = 1 + \varepsilon$ and slope $\alpha_\mathbb{P}' = 0.25\,\mathrm{GeV}^{-2}$ and $\beta_{\mathbb{P}/p}^2(0) = 58.74\,\mathrm{GeV}^{-2}$ is related to the Pomeron-proton coupling and the total pp cross-section via

$$\sigma_{pp} = \beta_{\mathbb{P}/p}^2(0) \simeq 40\,\mathrm{mb}.$$

The rise in the total cross-section observed in pp scattering is described by setting $\varepsilon = 0.085$.

3. Donnachie and Landshoff [68] parameterisation: it is similar to the Berger-Streng parameterisation, but with a power law distribution for t. This parameterisation is given by equation (4.12) with $\delta^2 = 3.26\,\mathrm{GeV}^{-2}$ and $\alpha(t)$ being identical to the Berger-Streng case, where m_p is the mass of the proton.

$$f_{\mathbb{P}/p}(x_\mathbb{P}, t) = \frac{9\delta^2}{4\pi^2} x_\mathbb{P}^{1 - 2\alpha_\mathbb{P}(t)} \left[\frac{4m_p^2 - 2.8t}{4m_p^2 - t} \frac{1}{(1 - t/0.7)^2} \right]^2 \qquad (4.12)$$

A comparison of the diffractive mass distribution in PHOJET along with 4 different Pomeron fluxes in PYTHIA as a function of M_X^2 is shown in figure 4.2. On the y axis is the logarithmic derivative of the SD cross-section (see equation (4.15)), which is seen as a flat line in the case of $1/M_X^2$, i.e, $\frac{d\sigma}{d\ln M_X^2} = $ constant. It is evident that the Bruni-Ingelman distribution is $1/M_X^2$ and the

Schuler-Sjöstrand is a modified $1/M_X^2$ distribution, while the Donnachie-Landshoff and Berger-Streng distributions enhance low diffractive masses due to the additional term in the exponent of M_X. PHOJET suppresses low diffractive masses.
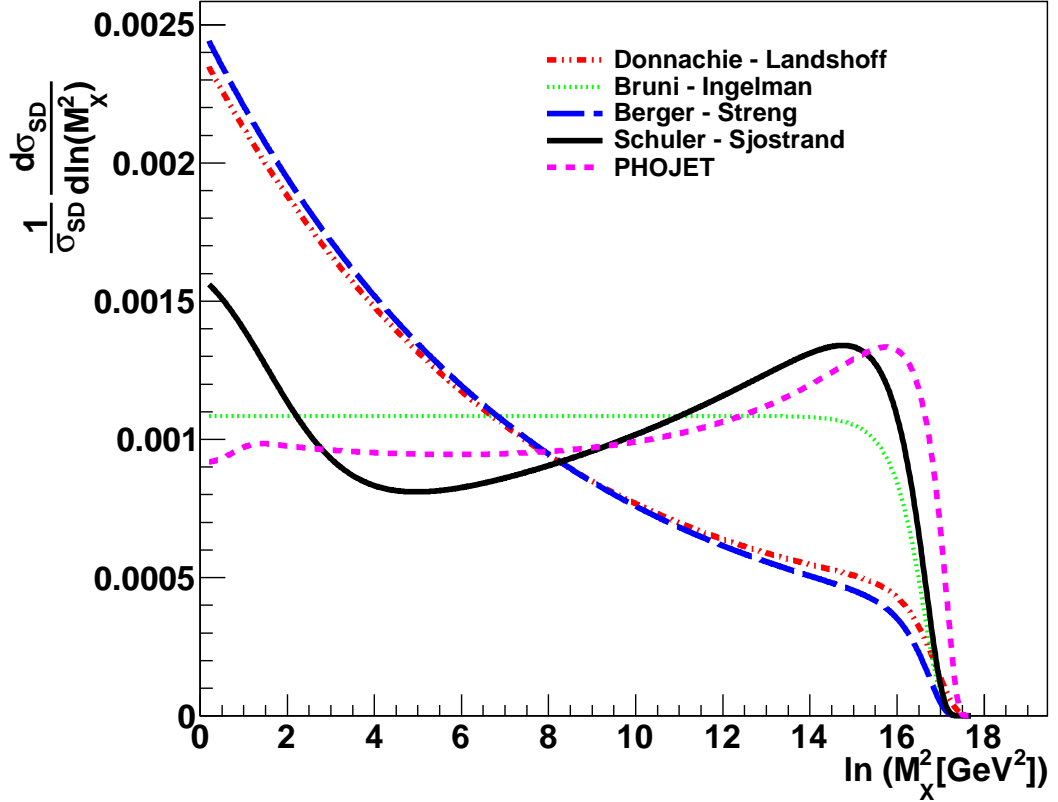
Figure 4.2: Diffractive mass distributions in PHOJET and PYTHIA for different Pomeron fluxes. Distributions are normalized to unit area.

4.1.2 Diffractive PDFs

The perturbative description employed for hard diffraction involves using PDFs for the Pomeron. PYTHIA 8.130 provides a selection of six PDF sets.

1. Q^2-independent parameterisations of the form given by

$$x f_{p_1/\mathbb{P}}(x) = N_{ab} x^a (1-x)^b \tag{4.13}$$

where x is the fraction of the Pomeron's momentum carried by a quark or a gluon. N_{ab} is a normalisation factor that ensures unit momentum sum and a and b can be different for the quark and gluonic content of the Pomeron. In this PDF set, the momentum fraction of gluons and quarks can be freely mixed. Additionally, the production of s quarks can be suppressed relative to u and d quarks, with quarks and anti-quarks being equally likely to be produced.

2. A Pomeron can be described by the PDF for a neutral pion. A few PDF sets exist, one of which is built into PYTHIA 8. The others can be accessed from LHAPDF [69]. (Parameterisations exist for π^+; π^- is obtained by charge conjugation and π^0 by averaging.)

3. The "H1 2006 Fit A" parameterisation is a Q^2-dependent set. This is based on fit A to H1 data of inclusive diffractive cross-section H1P06, collected in 2006, described in section 5.3 of [37].

4. The "H1 2006 Fit B" parameterisation is another Q^2-dependent set based on fit B to the H1 data of inclusive diffractive cross-section H1P06, collected in 2006, described in section 5.3 of [37].

5. The "H1 2007 Jets" parameterisation is a Q^2-dependent set based on fits to H1 data collected in 2007. This fit uses measurements of both the diffractive dijet cross-section H1P07 presented in [70] and the inclusive diffractive cross-section presented in [37].

6. The "H1 2006 Fit B LO" [71] Q^2-dependent parameterisation, based on fit B to H1 data H1P06 was added recently.

HERA PDF sets 3, 4 and 5 above are next to leading order (NLO) sets while PDF set 6 is a LO set. As PYTHIA 8 uses leading order (LO) matrix elements to calculate cross-sections, the LO fit from the H1 collaboration is used as the default PDF.

Generally, parton distributions are normalised so that they obey the momentum sum rule

$$\sum_i \int_0^1 x_i f(x_i) \, dx = 1,$$

where i includes all partons. Here, x is the fraction of the hadron's momentum carried by a quark or gluon and f is the DPDF. The motivation for this to hold is momentum conservation. However, since the Pomeron is not a physical particle, it is not clear if DPDFs should satisfy the momentum sum rule. Those from H1 add up to a momentum sum of roughly 50%. PYTHIA 8 has a free parameter to rescale the four H1 fits above by this uniform factor. To achieve a momentum sum of around unity, a rescaling factor of 2.0 should be used. Only the product of the Pomeron flux and the Pomeron PDF is meaningful, allowing arbitrary separate normalizations of the Pomeron flux and the Pomeron PDF.

4.2   Event generation and particle production

PYTHIA 8 by default only allows collisions with CM energy above $10\,\mathrm{GeV}$. The diffractive mass spectra extend down to about $1.2\,\mathrm{GeV}$, the mass of the Δ resonance. A perturbative description at this scale is not possible, giving rise to a separate handling of low and high masses. For $M_X \leq 10\,\mathrm{GeV}$, the non-perturbative description with longitudinally stretched strings, as described in section 3.2.2 is implemented.

In the mass range $10\,\mathrm{GeV} < M_X < \sqrt{s}$, a perturbative description is implemented. The probability for this description is given by

$$P_{\mathrm{pert}} = 1 - \exp((M_X - m_{\mathrm{min}})/m_{\mathrm{width}}) \tag{4.14}$$

where m_{min} and m_{width} are free parameters. The probability of a perturbative description (P_{pert}) is by definition equal to zero for diffractive masses $M_X < m_{\mathrm{min}}$. The default values of m_{min} and m_{width} are set at $10\,\mathrm{GeV}$ so that P_{pert} vanishes when $M_X < 10\,\mathrm{GeV}$.

The standard perturbative multiple interactions framework for pp collisions provides parton-parton interaction cross-sections at a fixed CM energy. To turn these cross-sections into probabilities, one

needs an ansatz for the Pomeron-proton total cross-section. The single diffractive cross-section is given by

$$\sigma_{\text{SD}} = \int \int dx_{\mathbb{P}} dt \ f_{\mathbb{P}/p}(x_{\mathbb{P}}, t) \sigma_{\mathbb{P}p}(\text{effective}). \tag{4.15}$$

In equation 4.15, $\sigma_{\mathbb{P}p}(\text{effective})$ is a tunable parameter and σ_{SD} is given by Regge parameterisation. The normalisation of the Pomeron flux ($f_{\mathbb{P}/p}(x_{\mathbb{P}}, t)$) is arbitrary and is adjusted accordingly. In PYTHIA 8 the default value of $\sigma_{\mathbb{P}p}(\text{effective})$ is 10 mb, which takes into account screening effects. This value is used for multiple interactions in diffractive systems as described below. $\sigma_{\mathbb{P}p}(\text{effective})$ is the main free tunable parameter in high-mass diffraction, and along with the choice of Pomeron PDF, can be fitted to represent diffractive event-shape data such as average charged multiplicity. $\sigma_{\mathbb{P}p}(\text{effective})$ includes a gap survival probability which depends on the energy of the collision. The higher the energy, the greater the probability of multiple interactions in the same event that suppress the rapidity gap.

Integrating equation (4.7) gives the total cross-section for minijet production ($\sigma_{\mathbb{P}p}(\text{perturbative})$) in a Pomeron-proton interaction. The average number of jet pairs in a Pomeron-proton interaction is given by

$$\frac{\sigma_{\mathbb{P}p}(\text{perturbative})}{\sigma_{\mathbb{P}p}(\text{effective})}.$$

Therefore, increasing the value of $\sigma_{\mathbb{P}p}(\text{effective})$ will reduce the multiple interactions activity per event. This mechanism is similar to that used in generating multiple interactions in inelastic pp collisions.

At a fixed pp CM energy, the diffractive (high) mass spectrum M_{X} can lie anywhere in the range $10 \, \text{GeV} < M_{\text{X}} < \sqrt{s}$, with a varying set of parameters (such as the p_T cut-off parameter (p_{T0})) along the range. Therefore, to speed-up the machinery, multiple interactions are initialised for a few (currently five) different diffractive mass values across the range, and all relevant parameters are interpolated between them to obtain the behaviour at a specific diffractive mass. Additionally, $AB \rightarrow XB$ and $AB \rightarrow AX$ are initialised separately. This allows for different beams (or PDFs) on both sides. This also facilitates double diffraction.

4.3   PYTHIA 8.130 vs PYTHIA 6.214 and PHOJET 1.12

All code until version 8 was written in Fortran 77. PYTHIA 8 [72] is the C++ successor of the older versions in Fortran. PYTHIA 6 and versions of PYTHIA 8 until 8.130 do not contain hard diffraction. It is since PYTHIA 8.130 that hard diffraction, as described in this chapter, has been included.

PYTHIA 8 before 8.130   The mechanism for diffractive scattering works in almost the same way as in PYTHIA 6. The only difference lies in the particle production. In PYTHIA 8.1 the ratio of the probability of the Pomeron ($\mathbb{P}$) coupling to a quark ($P(q)$) and the Pomeron coupling to a gluon ($P(g)$) is given by equation (4.16), where M_X is the mass of the diffractive system. N (default value = 5) and p (default value = 1) are user-defined parameters that control the ratio. These parameters define the way the longitudinal momentum is shared between the two remnant partons when a gluon is kicked out of a hadron. This introduces a diffractive mass dependence on the ratio of the two couplings, enabling the gluonic contribution to dominate at higher diffractive masses.

$$\frac{P(q)}{P(g)} = \frac{N}{M_X^p} \qquad (4.16)$$

A study comparing the pseudorapidity (η), transverse momentum (p_T) and charged particle density ($dN_{ch}/d\eta$) distributions in PYTHIA 8.145, PYTHIA 6.214 and PHOJET 1.12 at CM energy 7 TeV is shown in figures 4.3 to 4.5. Only the SD spectra are compared.

It is clearly seen that the addition of hard diffraction to PYTHIA 8 [60] shows an improvement in the p_T and multiplicity tails, giving a description comparable to PHOJET, which also has hard diffractive scattering.
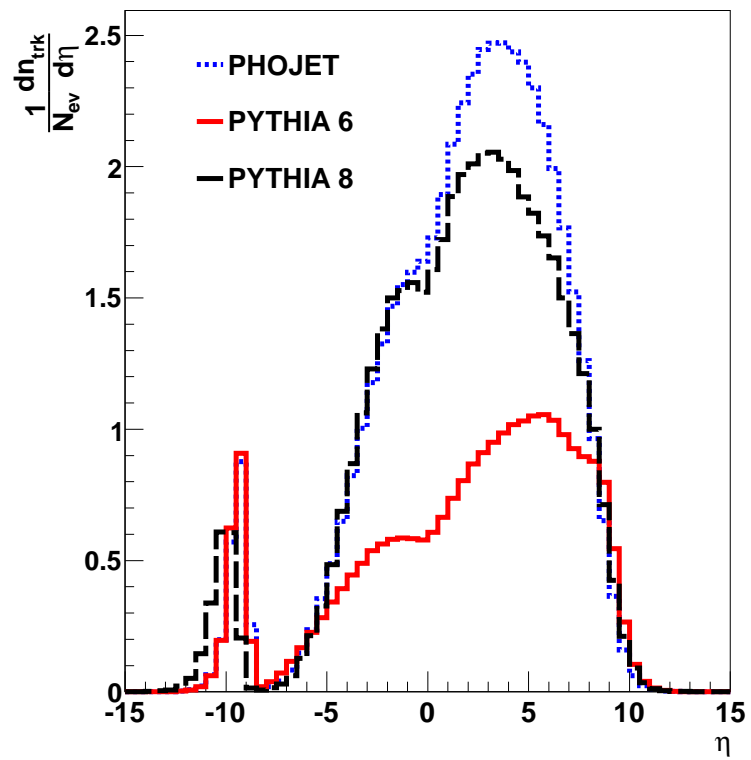
Figure 4.3: η distribution for one side SD events at 7 TeV in PHOJET, PYTHIA 6 and PYTHIA 8. The plot shows events when one of the incoming protons is diffracted.
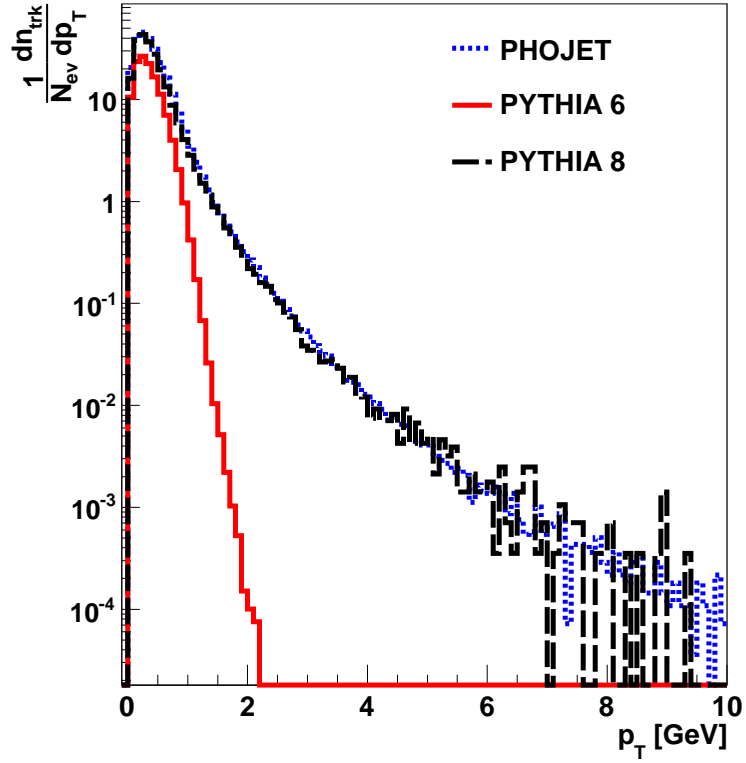
Figure 4.4: p_T distribution for SD events at 7 TeV in PHOJET, PYTHIA 6 and PYTHIA 8.

4.4 Diffractive parameters vs observables

In this section the effect of the free parameters used in the description of the hard diffractive part of PYTHIA 8 on the average charged particle multiplicity measurement of SD events at mid-rapidity ($|\eta| < 0.5$) is studied on a sample of 10000 events.

Table 4.1 lists the average charged particle multiplicity in the pseudorapidity range $|\eta| < 0.5$ for PHOJET, PYTHIA 6.4 and untuned PYTHIA 8.130.

Table 4.1: Average number of charged particles in $|\eta| < 0.5$ given by different generators for the event class SD.

Energy	PHOJET	PYTHIA 6	PYTHIA 8
900 GeV	1.22 ±0.01	0.59 ±0.01	1.03 ±0.01
2.2 TeV	1.44 ±0.01	0.64 ±0.01	1.27 ±0.01
7 TeV	1.73 ±0.01	0.59 ±0.01	1.65 ±0.01
10 TeV	1.79 ±0.01	0.69 ±0.01	1.90 ±0.01
14 TeV	1.90 ±0.01	0.73 ±0.01	2.02 ±0.01

From table 4.1 it is seen that the predictions of PHOJET and PYTHIA 8 are comparable, as seen

59
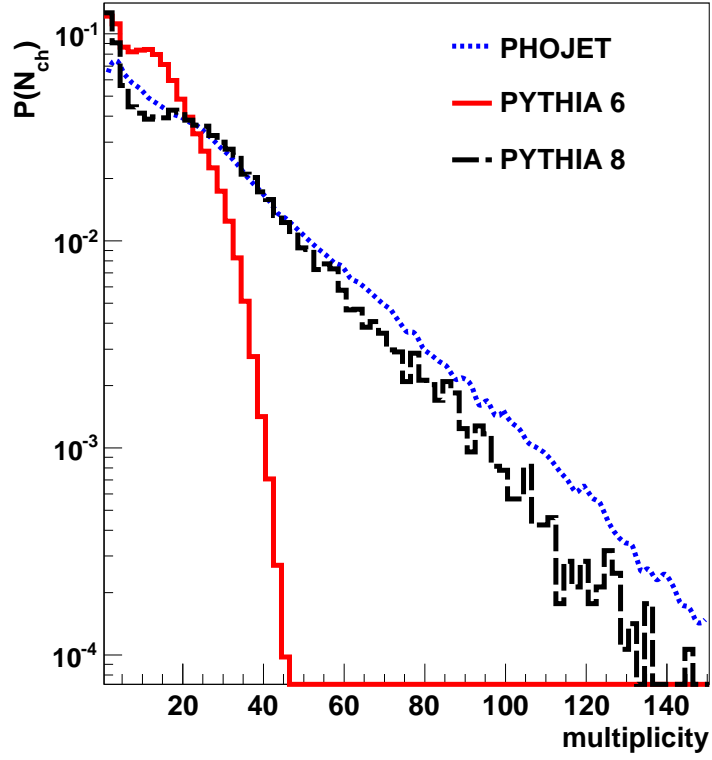
Figure 4.5: Multiplicity distribution for SD events at 7 TeV in PHOJET, PYTHIA 6 and PYTHIA 8.
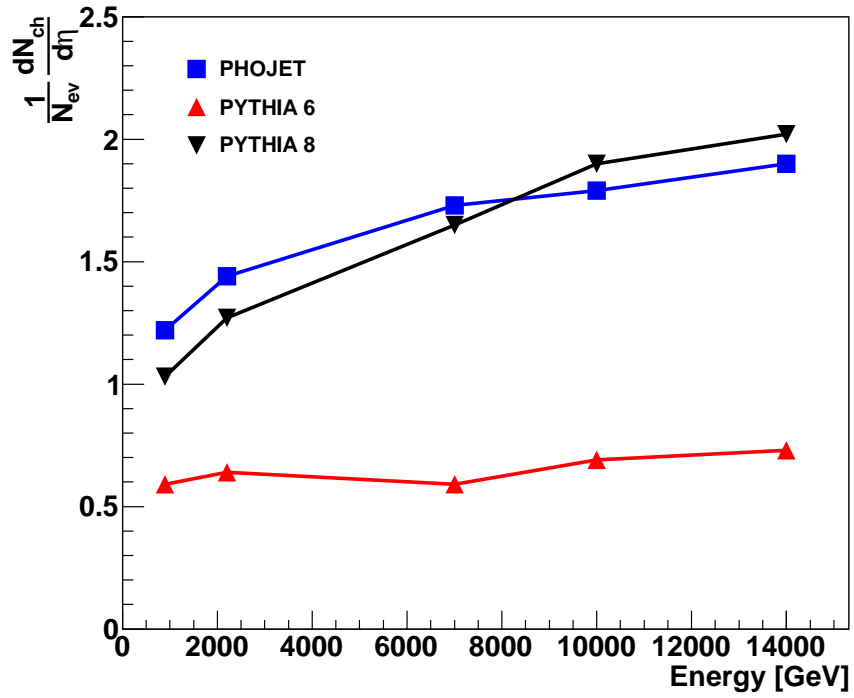
Figure 4.6: Average number of charged particles in $|\eta| < 0.5$ predicted by different physics models and different energies in SD events.

in figure 4.6. It is note-worthy that the pseudorapidity density increases more rapidly with CM energy in PYTHIA 8 than in other models. To investigate the dependence, the diffractive parameters are varied in their allowed regions.

There are five tunable diffractive parameters:

- Choice of Pomeron flux model: Schuler-Sjöstrand (SS), Bruni-Ingelman (BI), Berger-Streng (BS), Donnachie-Landshoff (DL).

- The effective Pomeron-proton cross-section: $2\,\text{mb} < \sigma_{\mathbb{P}-p}(\text{effective}) < 40\,\text{mb}$.

- Choice of Pomeron PDF: H12007 Jets, H12006 Fit A and H12006 FitB. The current default "H1 2006 Fit B LO" PDF was added into PYTHIA 8 after the analysis presented here was performed, and is hence excluded from this section.
  The standard PYTHIA 8 machinery is used for multiple interactions, parton showers and hadronisation. Hence, the parameters are common with the ND part.

- Diffractive mass threshold, above which the treatment is perturbative:
  $5\,\text{GeV} < M_X < \sqrt{s}$.

- Energy dependence of p_{T0} in equation (4.9) given by $E_{\text{CM}}^{\text{Pow}}$. This parameter is used to regularise a diverging QCD cross-section and is common to both the diffractive and non-diffractive parts.

Tables 4.2 to 4.5 and figures 4.7 to 4.10 show the influence on the pseudorapidity density of changing the first four parameters in the list above.

The final tunable parameter is the energy dependence of the p_{T0} parameter in equation (4.9). E_{CM}^{Pow} is a tunable parameter to increase multiple interactions. This restricts the quick increase of $d\text{N}/d\eta$ with energy. The pseudorapidity densities obtained with different values of E_{CM}^{Pow} are listed in table 4.6 and seen pictorially in figure 4.11.

Table 4.2: Average number of charged particles in $|\eta| < 0.5$ in SD events generated by PYTHIA 8 for different Pomeron flux models.

Energy	SS (default)	BS	BI	DL
900 GeV	1.03 ± 0.01	0.65 ± 0.01	0.99 ± 0.01	0.70 ± 0.01
2.2 TeV	1.27 ± 0.01	0.65 ± 0.01	1.15 ± 0.01	0.74 ± 0.01
7 TeV	1.65 ± 0.01	0.75 ± 0.01	1.49 ± 0.01	0.81 ± 0.01
10 TeV	1.90 ± 0.01	0.77 ± 0.01	1.66 ± 0.01	0.85 ± 0.01
14 TeV	2.02 ± 0.01	0.82 ± 0.01	1.73 ± 0.01	0.88 ± 0.01
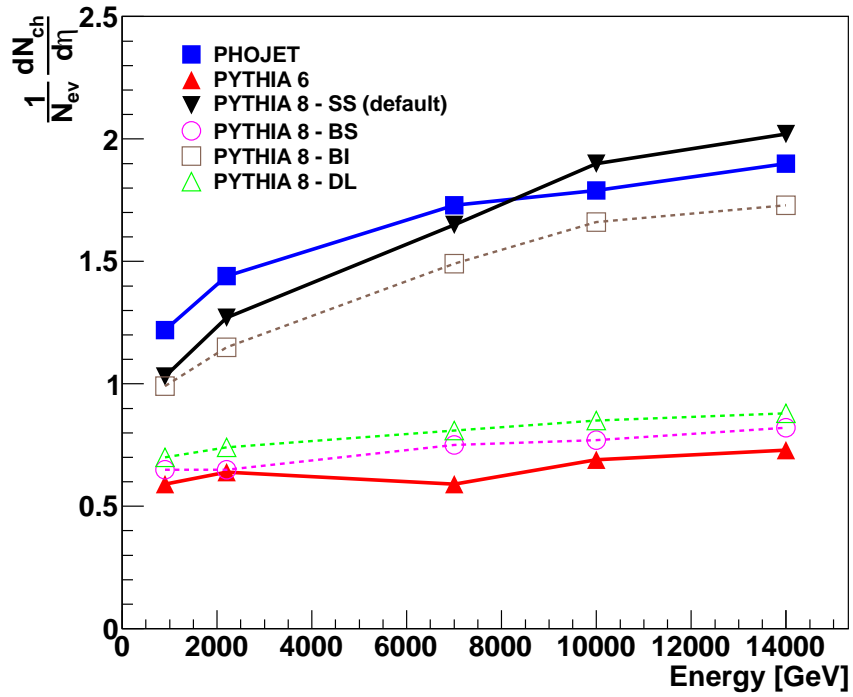
Figure 4.7: Average number of charged particles in $|\eta| < 0.5$ at different energies for different Pomeron fluxes in SD events.

Table 4.3: Average number of charged particles in $|\eta| < 0.5$ for SD events generated by PYTHIA 8 for different Pomeron-proton total cross-section $\sigma_{\mathbb{P}-p}$.

Energy	$\sigma_{\mathbb{P}-p} = 2\,\text{mb}$	$\sigma_{\mathbb{P}-p} = 10\,\text{mb}$ (default)	$\sigma_{\mathbb{P}-p} = 15\,\text{mb}$	$\sigma_{\mathbb{P}-p} = 25\,\text{mb}$	$\sigma_{\mathbb{P}-p} = 40\,\text{mb}$
900 GeV	1.82 ± 0.01	1.03 ± 0.01	1.03 ± 0.01	1.02 ± 0.01	0.99 ± 0.01
2.2 TeV	2.45 ± 0.02	1.27 ± 0.01	1.27 ± 0.01	1.17 ± 0.01	1.04 ± 0.01
7 TeV	3.33 ± 0.02	1.65 ± 0.01	1.49 ± 0.01	1.36 ± 0.01	1.31 ± 0.01
10 TeV	3.73 ± 0.02	1.90 ± 0.01	1.62 ± 0.01	1.43 ± 0.01	1.42 ± 0.01
14 TeV	4.00 ± 0.02	2.02 ± 0.01	1.81 ± 0.01	1.59 ± 0.01	1.51 ± 0.01
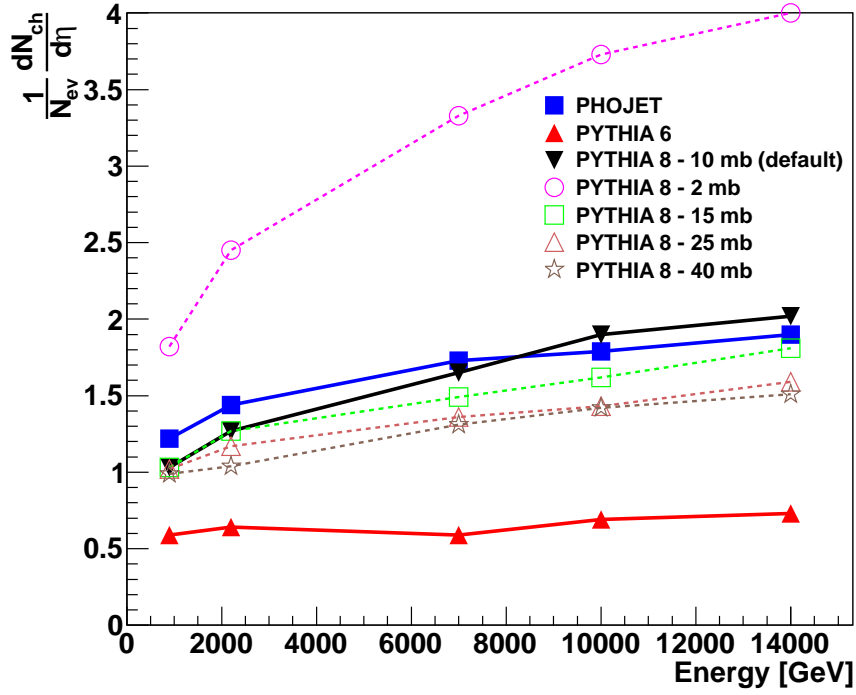
Figure 4.8: Average number of charged particles in $|\eta| < 0.5$ at different energies for different Pomeron-proton total cross-sections in SD events.

Table 4.4: Average number of charged particles in $|\eta| < 0.5$ in SD events generated by PYTHIA 8 for different Pomeron PDFs. The "H1 2006 Fit B LO" was added after later.

Energy	H12007 Jets (default)	H12006 FitA	H12006 FitB
900 GeV	1.03 ± 0.01	1.08 ± 0.01	1.16 ± 0.01
2.2 TeV	1.27 ± 0.01	1.28 ± 0.01	1.34 ± 0.01
7 TeV	1.65 ± 0.01	1.72 ± 0.01	1.77 ± 0.01
10 TeV	1.90 ± 0.01	1.85 ± 0.01	1.90 ± 0.01
14 TeV	2.02 ± 0.01	2.08 ± 0.01	2.19 ± 0.01

Table 4.5: Average number of charged particles in $|\eta| < 0.5$ in SD events generated by PYTHIA 8 for different diffractive mass thresholds M_X. The value of $\sqrt{s} + 1$ was chosen so that in this case there is no hard diffraction.

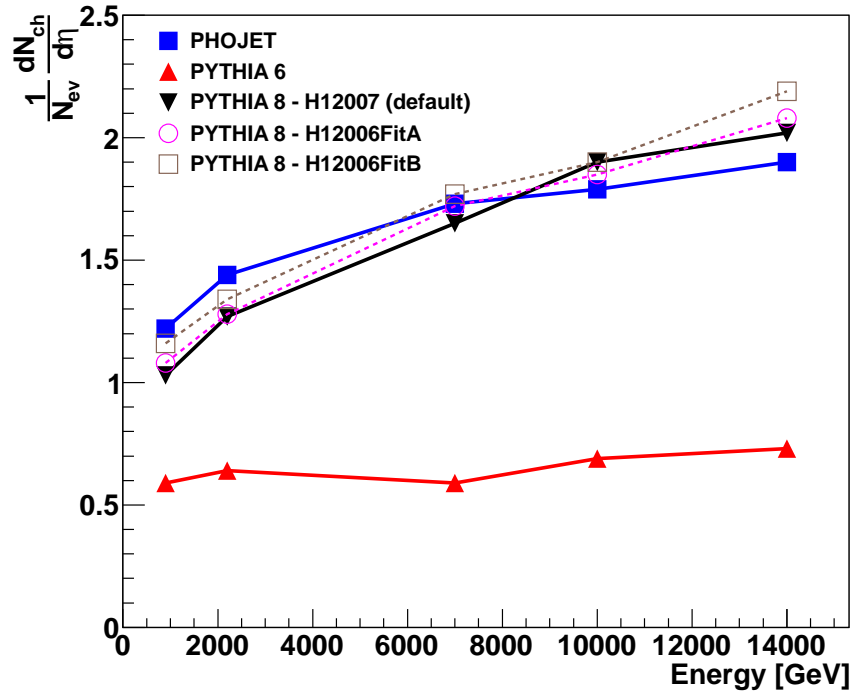| Energy	$M_X = 10\,\mathrm{GeV}$ (default)	$M_X = 25\,\mathrm{GeV}$	$M_X = \sqrt{s} + 1$
900 GeV	1.03 ± 0.01	1.00 ± 0.01	0.74 ± 0.01
2.2 TeV	1.27 ± 0.01	1.24 ± 0.01	0.80 ± 0.01
7 TeV	1.65 ± 0.01	1.67 ± 0.01	0.87 ± 0.01
10 TeV	1.90 ± 0.01	1.88 ± 0.01	0.89 ± 0.01
14 TeV	2.02 ± 0.01	2.09 ± 0.01	0.89 ± 0.01

Figure 4.9: Average number of charged particles in $|\eta| < 0.5$ at different energies for different Pomeron PDFs in SD events.

Figure 4.10: Average number of charged particles in $|\eta| < 0.5$ at different energies for different diffractive mass thresholds in SD events.

The choice of Pomeron flux parameterisation affects the average multiplicity generated in a SD event. At all energies the Schuler-Sjöstrand and the Berger-Streng models predict higher average multiplicities than the Ingelman-Bruni and Donnachie-Landshoff models, as higher mass diffractive states are produced more often in the former two models (see figure 4.2). The choice of Pomeron PDFs does not affect the pseudorapidity density distribution at a given energy. Changing the diffractive mass threshold does not affect the distribution unless the threshold is set high enough to avoid hard-diffraction altogether, resulting in a description of diffraction the same as that in PYTHIA 6. The value of the total Pomeron-proton cross-section affects the amount of activity in an event and hence, the pseudorapidity density distribution. A higher value of $\sigma_{\mathbb{P}p}(\text{effective})$ lowers multiple interactions and reduces the average multiplicity. This is the main tunable parameter in the description of high-mass diffraction.

Table 4.6: Average number of charged particles in $|\eta| < 0.5$ in SD events generated by PYTHIA 8 for different values of the parameter giving the energy dependence of the p_T cut-off.

Energy	$E_{\text{CM}}^{Pow} = 0.16$	$E_{\text{CM}}^{Pow} = 0.24$ (default)	$E_{\text{CM}}^{Pow} = 0.30$	$E_{\text{CM}}^{Pow} = 0.35$
900 GeV	1.13 ± 0.01	1.03 ± 0.01	1.21 ± 0.01	1.25 ± 0.01
2.2 TeV	1.25 ± 0.01	1.27 ± 0.01	1.37 ± 0.01	1.48 ± 0.01
7 TeV	1.73 ± 0.01	1.65 ± 0.01	1.68 ± 0.01	1.78 ± 0.01
10 TeV	1.92 ± 0.01	1.90 ± 0.01	1.89 ± 0.01	1.85 ± 0.01
14 TeV	2.15 ± 0.01	2.02 ± 0.01	2.01 ± 0.01	2.04 ± 0.01

4.5   Summary

This chapter gives a description of the hard diffraction model in PYTHIA 8. In this Pomeron-based model, a Pomeron is emitted from one of the protons in a pp collision via a soft interaction. The proton that emits the Pomeron is deflected after it transfers $x_{\mathbb{P}}$ of its momentum to the Pomeron. The Pomeron then interacts with the other proton via a hard interaction. This approach was pioneered by Bruni, Edin and Ingelman in their MC event generator POMPYT and implemented in PYTHIA 8. The standard PYTHIA 8 machinery for multiple interactions, parton showers and hadronisation for this hard interaction is used.
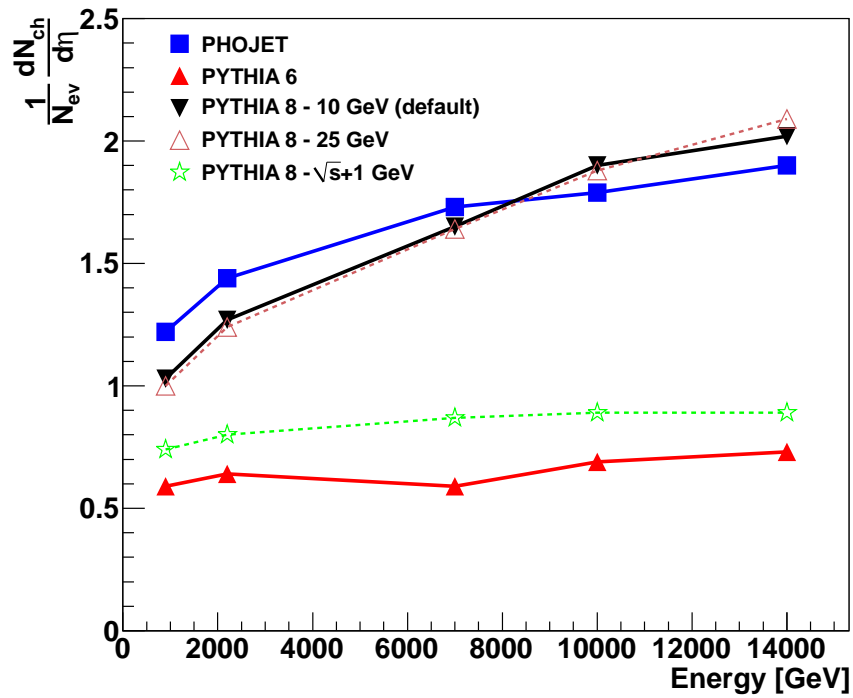
65
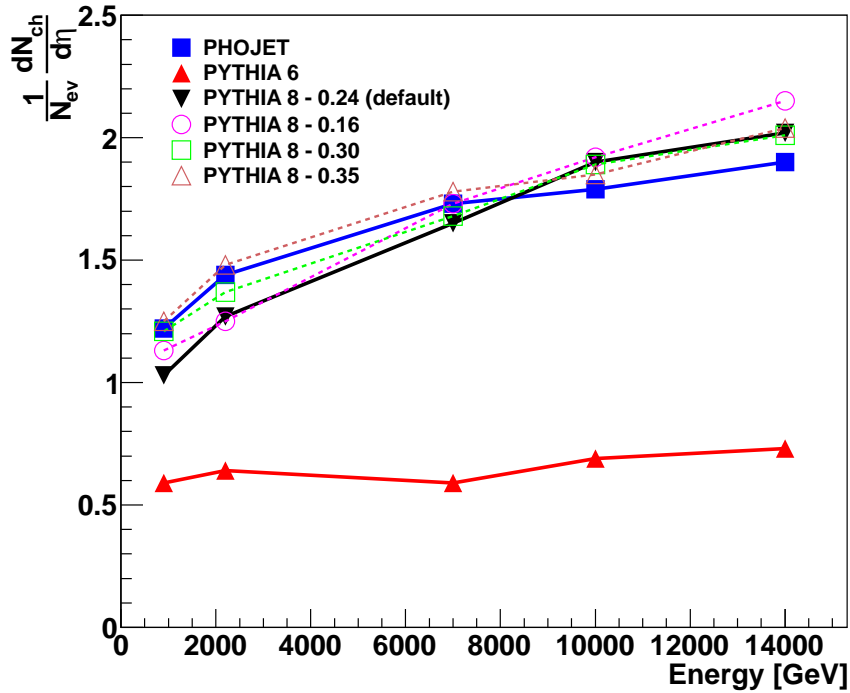
Figure 4.11: Average number of charged particles in $|\eta| < 0.5$ at different energies for different distributions of p_{T0} in SD events.

The Pomeron-specific event-generation parts consist of selecting diffractive cross-sections, the Pomeron flux parameterisation, and a classification of the diffractive system as either a low-mass or high-mass system, where these are handled differently. The diffractive cross-sections are parameterised as a function of the CM energy and are identical to those in PYTHIA 6. For diffractive processes, there are four different Pomeron flux parameterisations that can be used to generate a diffractive mass and the momentum transfer t. Based on the diffractive mass, the diffractive system is classified as being a low-mass unresolved system or a high-mass resolved system. The high-mass system uses a perturbative picture for Pomeron-proton collisions, which are only allowed in PYTHIA 8 for $E_{CM} > 10\,\text{GeV}$. For diffractive systems below this limit, the simple low-mass description from PYTHIA 6 is used, where longitudinal strings are stretched. The high-mass description uses Pomeron PDFs and an ansatz for the total Pomeron-proton cross-section, which is a tunable parameter. Currently there are six Pomeron PDFs one can choose from. The addition of a hard diffractive part to PYTHIA 8 makes it more similar to PHOJET, which has a different implementation of hard diffraction.

The final part of the chapter looks at the difference that changing of the parameters mentioned above makes in the average multiplicity of SD events at a given CM energy. The choice of the Pomeron PDF has the least influence on the average multiplicity, while the total Pomeron-proton cross-section and choice of p_{T0} have larger influences. These parameters need to be tuned to data. For a realistic comparison with data, both the non-diffractive and diffractive parts of PYTHIA 8 need to be tuned to existing data. Since there is no one-to-one correspondence between the parameters in PYTHIA 6 and PYTHIA 8, existing PYTHIA 6 tunes cannot be easily converted to a PYTHIA 8 tune. A comparison of PYTHIA 8 with ALICE diffractive data is presented in chapter 6.

TRIGGER EFFICIENCIES AND SYSTEMATICS

The ALICE detectors, including those used to trigger, do not provide full phase space coverage and are not 100% efficient. Hence, a trigger correction has to be applied to correct for events which are not detected by the trigger system.

The overall correction factor R_T depends on several variables:

$$R_T = \underbrace{\frac{\text{detectable}}{\text{generated}}}_{\text{acceptance}} \underbrace{\frac{\text{detected}}{\text{detectable}}}_{\text{detector eff}} \underbrace{\frac{\text{triggered}}{\text{detected}}}_{\text{trig elec eff}} \underbrace{\frac{\text{reconstructed}}{\text{triggered}}}_{\text{rec eff}} \underbrace{\frac{\text{selected}}{\text{reconstructed}}}_{\text{analysis}}. \tag{5.1}$$

In equation (5.1), "generated" comes from the MC model; "detectable" refers to the events within the acceptance of the triggering detectors; "detected" refers to the events recorded by the detector within its hardware and electronics limitations; "triggered" refers to the events recorded by the trigger electronics; "reconstructed" refers to the events reconstructed by the ALICE reconstruction software and "selected" refers to those events that pass analysis cuts. The first term in the equation refers to the acceptance of the detector, the second term to the detector efficiency, the third term to the trigger electronics efficiency, the fourth to the reconstruction software efficiency and the fifth to the selection procedures in the analysis.

Trigger systems use a set of selection criteria to decide if we want to record or analyse an event or not. There are two stages at which we can implement triggers with our data: in real time and

offline. An online trigger is implemented at the stage of recording data from collisions, in real time. Only events triggered by the online trigger are written to tape and can be analysed later. These interactions are then reconstructed using the ALICE reconstruction software [29]. An offline filter is implemented on the set of recorded data; interactions that pass the selection criteria of the offline triggers are then analysed. Different offline triggers can be implemented on the same sample of recorded events for different physics analyses.

Each trigger condition is associated with an efficiency. The efficiency of a trigger gives the fraction of produced events that are triggered ($\frac{N_{triggered}}{N_{generated}}$). The efficiencies presented in this chapter combine the first three terms of equation 5.1. Trigger efficiencies are different for different triggers and also for different process types (SD, DD, ND and CD).

5.1 Minimum Bias Triggers

Minimum bias (MB) events are those events selected by a trigger with the least bias, or least rejection, but with a good beam gas (BG) rejection (beam gas is explained in chapter 2). The definition of a MB trigger is detector dependent. Possible MB triggers in ALICE, some of which were used for online data taking, are defined and shown in table 5.1.

The two V0 trigger conditions used here are V0OR and V0AND:

V0OR = V0A or V0C

V0AND = V0A and V0C.

The Global Fast Or (GFO) is the trigger input obtained from the SPD (see section 2.3). Combinations of these trigger inputs are used to formulate MB trigger conditions. For example, in the first MB trigger, MB1, a hit in any of the pixels or in either of the V0 disks satisfies this condition as long as the interaction was not a BG event. This is the most inclusive MB trigger condition as it is the "OR" of all three inputs, the GFO, V0A and V0C. On the other hand, the least inclusive MB trigger condition is MB3 which is the "AND" of the three inputs. The SPD and TPC trigger

Table 5.1: Trigger definitions.

MB1 = (GFO or V0OR) and $\overline{\text{BG}}$
MB2 = (GFO and V0OR) and $\overline{\text{BG}}$
MB3 = (GFO and V0AND) and $\overline{\text{BG}}$
SPD = at least 1 SPD tracklet
PIX1 = at least 1 fired chip in the pixels
PIX2 = at least 2 fired chips in the pixels
TPC = at least 1 TPC track

conditions require at least one reconstructed tracklet in the SPD and track in the TPC respectively. The two pixel triggers PIX1 and PIX2 require at least 1 and 2 fired chips in the SPD respectively. Track and tracklet reconstruction, and the pixel trigger are explained in sections 2.4.1 and 2.2.2.

It is necessary to estimate what fraction of the inelastic cross-section we take with different MB triggers. These estimates are model dependent, hence a comparison between PYTHIA 6 [11] and PHOJET [12] is essential. The efficiencies at 900 GeV and 2.36 TeV quoted in this chapter were calculated on samples of 280,000 events generated by PHOJET 1.12 and PYTHIA 6.4.14 with the D6T tune [73]. The efficiencies quoted at 7 TeV were calculated on samples of 2,000,000 events generated by PHOJET 1.12 and PYTHIA 6.4.14 with the Perugia-0 tune [74], and 160,000 events generated by PYTHIA 8.145 [72]. All samples have been reconstructed with the magnetic field in the ALICE dipole magnet of 0.5 T.

The statistical error is calculated as

$$\sqrt{\frac{\varepsilon_T^{proc}(1-\varepsilon_T^{proc})}{N^{procGEN}}},$$

where ε_T^{proc} is the trigger efficiency of a particular process type and $N^{procGEN}$ is the number of events of that process type generated by the MC event generator. All errors quoted in the tables that follow are statistical errors, unless otherwise stated.

Tables 5.2 and 5.3 give the trigger efficiencies for PYTHIA 6 and PHOJET at 900 GeV respectively. The percentages in brackets give the fraction of inelastic events of that particular type at this energy. In these tables NSD = DD + ND + CD and INEL = SD + DD + CD + ND. Note that

70

there is no CD in PYTHIA.

Table 5.2: 900 GeV, PYTHIA 6 MB trigger efficiencies expressed as percentages. Statistical errors that appear as 0.0 are less than 0.05.

Trigger	SD (22.4%)	DD (12.2%)	ND (65.4%)	NSD	INEL
MB1	77.0±0.2	91.5±0.1	100.0±0.0	98.7±0.0	93.8±0.0
MB2	49.0±0.2	54.9±0.3	98.3±0.0	91.5±0.1	82.0±0.1
MB3	27.6±0.2	35.1±0.3	96.7±0.0	87.1±0.1	73.7±0.1
V0AND	29.1±0.2	49.1±0.3	98.1±0.0	90.4±0.1	76.7±0.1
SPD	45.4±0.2	49.3±0.3	96.5±0.0	89.1±0.1	79.3±0.1
PIX1	54.3±0.2	62.9±0.3	99.1±0.0	93.4±0.1	84.6±0.1
PIX2	49.8±0.2	55.4±0.3	98.3±0.0	91.6±0.1	82.2±0.1
TPC	43.0±0.2	46.0±0.3	94.9±0.1	87.2±0.1	77.3±0.1

Table 5.3: 900 GeV, PHOJET MB trigger efficiencies expressed as percentages. Statistical errors shown as 0.0 are less than 0.05.

Trigger	SD (19.1%)	DD (6.3%)	CD (2.0%)	ND (72.5%)	NSD	INEL
MB1	86.1±0.1	97.9±0.1	98.3±0.2	100.0±0.0	99.8±0.0	97.2±0.0
MB2	59.2±0.2	76.5±0.3	69.5±0.6	99.4±0.0	96.9±0.0	89.7±0.1
MB3	33.9±0.2	65.8±0.4	26.8±0.6	97.9±0.0	93.6±0.1	82.2±0.1
V0AND	34.4±0.2	77.1±0.3	27.5±0.6	98.3±0.0	94.9±0.1	83.3±0.1
SPD	55.6±0.2	71.3±0.3	70.3±0.6	98.1±0.0	95.3±0.0	87.7±0.1
PIX1	63.5±0.2	81.4±0.3	83.4±0.5	99.7±0.0	97.9±0.0	91.3±0.1
PIX2	59.3±0.2	76.6±0.3	76.6±0.6	99.5±0.0	97.1±0.0	89.9±0.1
TPC	53.7±0.2	68.6±0.3	68.9±0.6	96.8±0.0	93.8±0.1	86.2±0.1

The triggering efficiency for ND events is close to 100% because of the nature of the final state of ND events. For the same reason, the higher percentage of events not triggered in the case of SD events compared to DD events is justified. In all cases, the MB1 trigger is the most efficient, as it is the most inclusive trigger condition. Efficiencies in PHOJET are systematically higher than for PYTHIA 6.

PYTHIA 6 generates events with diffractive mass (M_X) sampled from the full kinematic range, but $M_X > 0.15s$ (where s is the CM energy of the collision) is unphysical due to the coherence condition. This corresponds to 15%, 12% and 11% of the SD cross-sections at CM energies 900 GeV, 2.36 TeV and 7 TeV respectively.

Restricting the range of invariant masses to the physical region leads to $\lesssim 1\%$ change in the inelastic trigger efficiency using the MB1 trigger.

Table 5.4: 2.36 TeV, PYTHIA 6 MB trigger efficiencies expressed as percentages. Statistical errors that appear as 0.0 are less than 0.05.

Trigger	SD (21.1%)	DD (12.8%)	ND (66.1%)	NSD	INEL
MB1	74.0±0.2	89.1±0.2	100.0±0.0	98.2±0.0	93.1±0.0
MB2	50.9±0.2	56.6±0.3	98.5±0.0	91.7±0.1	83.1±0.1
MB3	32.2±0.2	36.3±0.3	97.1±0.0	87.2±0.1	75.6±0.1
V0AND	33.8±0.2	46.8±0.3	98.3±0.0	89.9±0.1	78.1±0.1
SPD	46.9±0.2	51.1±0.3	96.8±0.0	89.4±0.1	80.4±0.1
PIX1	55.4±0.2	63.7±0.3	99.1±0.0	93.4±0.1	85.4±0.1
PIX2	51.3±0.2	57.2±0.3	98.5±0.0	91.8±0.1	83.3±0.1
TPC	44.5±0.2	47.8±0.3	95.4±0.0	87.7±0.1	78.6±0.1

Table 5.5: 2.36 TeV, PHOJET MB trigger efficiencies expressed as percentages. Statistical errors that appear as 0.0 are less than 0.05.

Trigger	SD (16.0%)	DD (5.7%)	CD (1.8%)	ND (76.6%)	NSD	INEL
MB1	82.6±0.2	96.2±0.4	98.0±0.2	100.0±0.0	99.7±0.0	97.0±0.0
MB2	58.7±0.2	74.1±0.4	68.5±0.7	99.5±0.0	97.1±0.0	91.0±0.1
MB3	37.2±0.2	62.0±0.4	28.9±0.6	98.4±0.0	94.4±0.0	85.3±0.1
V0AND	37.8±0.2	71.6±0.4	29.6±0.6	98.8±0.0	95.5±0.0	86.2±0.1
SPD	55.4±0.2	69.1±0.4	67.8±0.7	98.3±0.0	95.6±0.0	89.2±0.1
PIX1	62.5±0.2	79.1±0.3	80.2±0.6	99.7±0.0	97.9±0.0	92.3±0.1
PIX2	58.8±0.2	74.2±0.4	73.7±0.6	99.5±0.0	97.2±0.0	91.1±0.1
TPC	53.6±0.2	66.9±0.4	65.5±0.7	97.0±0.0	94.3±0.0	87.8±0.1

Tables 5.4 and 5.5 show the trigger efficiencies for the same MB triggers at a CM energy of 2.36 TeV, and tables 5.6 and 5.7 show trigger efficiencies at a CM energy of 7 TeV for PYTHIA 6 and PHOJET respectively. Comparing tables 5.4 and 5.5, it is clear that, again, the triggering efficiency estimates are systematically higher in PHOJET than in PYTHIA 6 for the same CM energy. This is caused by the different efficiencies for diffractive events. For SD events they are higher for PHOJET by ∼10-20% while for DD the difference is larger. This is a consequence of the difference in the diffractive mass distributions (see figure 4.2) between PYTHIA 6 and PHOJET at small values of M_X - PYTHIA 6 enhances low diffractive mass events that have low multiplicity, a large rapidity gap and are undectable in ALICE. ALICE has no acceptance for invariant masses

72

smaller than 10[GeV] [75]. Another reason is the higher multiplicities in diffractive events in PHOJET arising from the hard diffractive component, compared to PYTHIA 6, which lacks a description of hard diffraction. The difference in efficiencies between PYTHIA 6 and PHOJET gets smaller with CM energy and increasing multiplicities. The V0AND trigger selects NSD events and hence is sensitive to diffraction, highlighting the differences in efficiencies between PYTHIA 6 and PHOJET.

Comparing PYTHIA 6 at different energies in tables 5.2 and 5.4 and 5.6, shows that triggering efficiency increases with energy. The reason is again because of increasing multiplicities with CM energy.

Table 5.6: 7 TeV, PYTHIA 6 MB trigger efficiencies expressed as percentages. Statistical errors that appear as 0.0 are less than 0.05.

Trigger	SD (19.2%)	DD (13.0%)	ND (67.8%)	NSD	INEL
MB1	72.8±0.1	87.5±0.1	99.9±0.0	97.9±0.0	93.1±0.0
MB2	50.9±0.1	57.0±0.1	98.5±0.0	91.8±0.0	84.0±0.0
MB3	35.1±0.1	38.2±0.1	97.1±0.0	87.6±0.0	77.6±0.0
V0AND	38.0±0.1	47.8±0.1	98.0±0.0	90.0±0.0	80.0±0.0
SPD	45.9±0.1	50.6±0.1	96.6±0.0	89.2±0.0	80.9±0.0
PIX1	56.1±0.1	64.6±0.1	99.1±0.0	93.6±0.0	86.4±0.0
PIX2	51.5±0.1	57.7±0.1	98.5±0.0	92.0±0.0	84.2±0.0
TPC	26.7±0.1	27.2±0.1	89.1±0.0	79.1±0.0	69.1±0.0

Table 5.7: 7 TeV, PHOJET MB trigger efficiencies expressed as percentages. Statistical errors expressed as 0.0 are less than 0.05.

Trigger	SD (13.8%)	DD (5.1%)	CD (1.7%)	ND (79.4%)	NSD	INEL
MB1	78.7±0.1	94.2±0.1	95.7±0.1	100.0±0.0	99.6±0.0	96.7±0.0
MB2	57.2±0.1	72.1±0.1	66.7±0.3	99.3±0.0	97.1±0.0	91.5±0.0
MB3	39.8±0.1	59.5±0.2	34.3±0.3	98.4±0.0	94.9±0.0	87.3±0.0
V0AND	40.5±0.1	67.8±0.1	35.2±0.3	98.9±0.0	95.8±0.0	88.2±0.0
SPD	54.0±0.1	66.9±0.1	64.0±0.3	97.8±0.0	95.3±0.0	90.0±0.0
PIX1	60.4±0.1	76.4±0.1	75.5±0.2	99.6±0.0	97.8±0.0	92.6±0.0
PIX2	57.3±0.1	72.2±0.1	69.7±0.2	99.3±0.0	97.1±0.0	91.6±0.0
TPC	43.9±0.1	51.9±0.2	45.6±0.3	91.0±0.0	87.8±0.0	81.7±0.0

Additionally, table 5.8 shows the trigger efficiencies for events generated by the PYTHIA 8 MC generator. It is interesting to note the differences between tables 5.6 and 5.8 that show trigger effi-

ciencies in PYTHIA 6 and PYTHIA 8 respectively. In general, trigger efficiencies are consistently higher in PYTHIA 8 than in PYTHIA 6 for NSD and inelastic events. Trigger efficiencies depend on the fractions of processes and their kinematic distribution in phase space, as described in the section below. The fractions in PYTHIA 8 are the same as in PYTHIA 6, while the hard diffractive kinematics in PYTHIA 8 are similar to PHOJET. The overall trigger efficiencies in PYTHIA 8 are a combination of both the features. Note that the statistical uncertainties on the efficiencies quoted in table 5.8 are higher than those in table 5.6 because of the limited statistics in PYTHIA 8.

Table 5.8: 7 TeV, PYTHIA 8 MB trigger efficiencies expressed as percentages. Statistical errors that appear as 0.0 are less than 0.05.

Trigger	SD (19.1%)	DD (13.0%)	ND (67.9%)	NSD	INEL
MB1	71.6±0.3	86.3±0.2	100.0±0.0	97.8±0.0	92.8±0.1
MB2	53.6±0.3	59.4±0.3	99.8±0.0	93.3±0.1	85.7±0.1
MB3	37.4±0.3	38.9±0.3	99.4±0.0	89.7±0.1	79.7±0.1
V0AND	37.7±0.3	45.0±0.3	99.6±0.0	90.8±0.1	80.7±0.1
SPD	50.9±0.3	55.2±0.3	98.7±0.0	91.7±0.1	83.9±0.1
PIX1	56.0±0.3	63.5±0.3	100.0±0.0	94.1±0.1	86.8±0.1
PIX2	53.7±0.3	59.5±0.3	99.8±0.0	93.3±0.1	85.7±0.1
TPC	44.4±0.3	45.4±0.3	94.7±0.1	86.8±0.1	78.7±0.1

5.2 Trigger Efficiencies and Fractions

The trigger correction takes into account the first three sources of bias in equation (5.1) giving us $\frac{N_{triggered}}{N_{generated}}$. However, these numbers depend on the fractions of the different process types (SD (sd), DD (dd) and ND (nd)). The exact cross-sections of SD, DD and ND events are not known and the trigger efficiencies for the different types of processes are different as shown above. The lack of knowledge of the different process types introduces model dependence in the efficiency estimate of the process type fractions. The correction we implement depends on the values of cross-sections and the generator we use. To study the systematic effect of the model dependency, we identify two areas in which models could differ: cross-sections and kinematics. The MC generators we use to study systematic effects are PYTHIA 6 and PHOJET. In this section, CD is included in ND unless specified.

The number of events generated by a MC model is

$$N^{GEN} = N^{ndGEN} + N^{sdGEN} + N^{ddGEN}.$$

The number of interactions triggered by a trigger type T is

$$N_T = N_T^{nd} + N_T^{sd} + N_T^{dd}$$

The trigger efficiency for a trigger type T is given by

$$\varepsilon_T^{EVENT} = \frac{N_T}{N^{GEN}} = \frac{N_T^{nd}}{N^{ndGEN}} \frac{N^{ndGEN}}{N^{GEN}} + \frac{N_T^{sd}}{N^{sdGEN}} \frac{N^{sdGEN}}{N^{GEN}} + \frac{N_T^{dd}}{N^{ddGEN}} \frac{N^{ddGEN}}{N^{GEN}}. \qquad (5.2)$$

where,

- N^{GEN} is the number of generated events,

- N_T is the number of events selected by trigger T,

- $N^{procGEN}$ is the number of generated events for process types ($proc = nd, dd, sd$) and

- N_T^{proc} is the number of events for the process types above selected by trigger T.

The overall trigger efficiency for a trigger T can be factorized as

$$\varepsilon_T^{EVENT} = \varepsilon_T^{nd} f^{nd} + \varepsilon_T^{sd} f^{sd} + \varepsilon_T^{dd} f^{dd} \qquad (5.3)$$

into a part that is dependent on the cross-sections of the different process types and another that depends only on the detector acceptance and kinematic distributions of particles for the different process types given by the model. In equation (5.3), f^{proc} is the process type fraction and ε_T^{proc} is the trigger efficiency for that process type, taking into account the first three terms of equation (5.1). These are given by

$$f^{proc} = \frac{N^{procGEN}}{N^{GEN}} \quad \text{and} \quad \varepsilon_T^{proc} = \frac{N_T^{proc}}{N^{procGEN}}. \qquad (5.4)$$

Model kinematics are folded with detector acceptance into the process type efficiencies ε_T^{proc} for each trigger T we define.

The corrected number of collisions taken with trigger type T is calculated as

$$N_T^{cor} = \frac{N_T^{DATA}}{\varepsilon_T^{EVENT}} \tag{5.5}$$

where N_T^{DATA} is the number of events in data selected by trigger T.

5.3 Systematics on multiplicity

The systematic uncertainty on all measured quantities depends on the trigger type T. However, there are other factors that contribute to the systematic uncertainty of a particular quantity. For example, in the case of a measurement of the charged particle density, a correction on the number of tracks has to be applied. The following section discusses how such a correction on the number of tracks can be applied.

The number of tracks generated (n^{GEN}) by a MC model in N^{GEN} generated interactions is

$$n^{GEN} = n^{ndGEN} + n^{sdGEN} + n^{ddGEN}.$$

The number of tracks selected (n_T) by a trigger T in N_T triggered interactions is

$$n_T = n_T^{nd} + n_T^{sd} + n_T^{dd}.$$

Here, $n^{procGEN}$ and n_T^{proc} are the number of generated and selected tracks respectively, in the individual process types: ND (nd), SD (sd) and DD (dd).

The uncorrected average multiplicity is given by $\mu = \frac{n}{N}$ where n is the number of measured tracks and N is the number of triggered events. Similarly, the average multiplicity for tracks generated for

process type *proc* in N^{GEN} interactions is given by $\mu^{procGEN} = \frac{n^{procGEN}}{N^{procGEN}}$. The uncorrected average multiplicity for tracks selected with a trigger type T for process type *proc* in N_T interactions is given by $\mu_T^{proc} = \frac{n_T^{proc}}{N_T^{proc}}$. The procedure to calculate track efficiency in N_T events selected with a trigger T is similar to that of event efficiency given in equation (5.2) and is given by

$$e_T^{TRACK} = \frac{n_T}{n^{GEN}} = \frac{n_T^{nd} + n_T^{sd} + n_T^{dd}}{n^{ndGEN} + n^{sdGEN} + n^{ddGEN}}$$
$$= \frac{e_T^{nd} \mu^{ndGEN} f^{nd} + e_T^{sd} \mu^{sdGEN} f^{sd} + e_T^{dd} \mu^{ddGEN} f^{dd}}{\mu^{ndGEN} f^{nd} + \mu^{sdGEN} f^{sd} + \mu^{ddGEN} f^{dd}} \qquad (5.6)$$

where

$$e_T^{proc} = \frac{n_T^{proc}}{n^{GEN}}$$

is the average track efficiency in events triggered by T.

The corrected number of tracks selected by trigger T in N interactions is given by

$$n_T^{cor} = \frac{n_T^{DATA}}{e_T^{TRACK}} \qquad (5.7)$$

where n_T^{DATA} is the number of tracks in the data sample selected by the trigger T.

Using equations 5.5 and 5.7, the corrected average multiplicity for a trigger T is given by

$$\mu_T^{corr} = \frac{n_T^{cor}}{N_T^{cor}} = \frac{n_T^{DATA}}{N_T^{DATA}} \frac{\varepsilon_{EVENT}^T}{e_T^{TRACK}}. \qquad (5.8)$$

Therefore, the final correction factor $\frac{\varepsilon_T^{EVENT}}{e_T^{TRACK}}$ on the triggered multiplicity μ_T depends on

1. cross-sections for various processes through process fractions f^{proc},

2. multiplicity of processes through μ^{proc} and

3. kinematics of processes through ε^{proc} and e^{proc}.

The first two contributions are model dependent with no dependence on the detector, while the third factor depends both on the model and the detector, as the detector doesn't cover the full

phase space.

The relative fractions of SD and DD events f^{sd} and f^{dd} are being measured in ALICE [75, 76] and the first set of results are available at [76]. To estimate the systematic uncertainty from cross-sections, the SD, DD and ND fractions are varied while keeping the total number of events constant and the variation of mean multiplicity is studied. Assuming that f^{sd} and f^{dd} are independent of each other, all the possible values of the fractions are scanned, bearing in mind that $f^{nd} + f^{sd} + f^{dd} = 1$. In this method we change the fraction of SD events by x and the fraction of DD events by y. f^{nd} also changes to keep the total number of events constant. The changed fractions of the different process types are given by the equations (5.9), where f_0^{proc} is the default fraction for process *proc* in the event generator:

$$f^{sd} = x f_0^{sd}, \quad f^{dd} = y f_0^{dd}, \quad f^{nd} = 1 - f^{sd} - f^{dd}. \tag{5.9}$$

Figures 5.1 and 5.2 show how varying the fraction of diffractive events changes the corrected mean multiplicity for events selected by the MB1 trigger at a CM energy of 900 GeV and 7 TeV respectively. f^{sd} and f^{dd} are on the x and y axes respectively. On the z-axis is the fractional change in the corrected mean multiplicity density from that calculated at the MC generator's default fractions (f_0^{sd} and f_0^{dd}).

In each plot the default fractions of SD and DD events for PYTHIA 6 are shown as the inverted triangle and for PHOJET as the regular triangle. In the 7 TeV case, both PYTHIA 6 and PYTHIA 8 have the same default fractions, shown in the plots as "PYTHIA".

The plots show that the mean multiplicity is higher for lower values of f^{sd} and f^{dd} (i.e, where f^{nd} is high), consistent with the models they are based on. In the 900 GeV case, using PYTHIA 6 kinematics and "correcting" with PHOJET default fractions increases the mean multiplicity by less than 1.5% compared to using PYTHIA 6 kinematics and PYTHIA 6's default fractions. Whereas, the change in mean multiplicity is around 0.5% when PHOJET's kinematics are "corrected" with PYTHIA 6's default fractions. In the 7 TeV case, the mean multiplicity changes by less than 3% irrespective of which kinematics model is used. An explanation could be an increase in multiplicity with CM energy in all models.
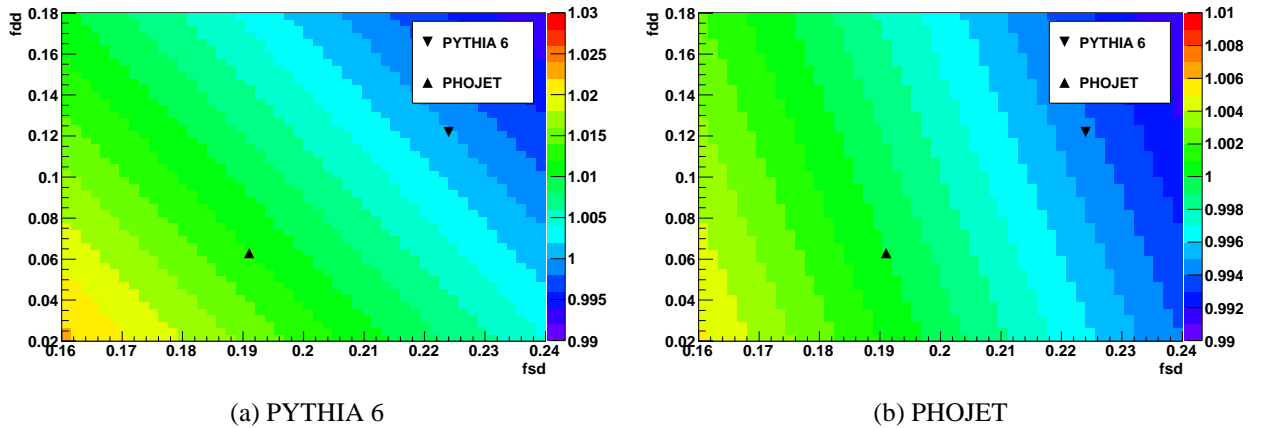
Figure 5.1: Systematics plots with MB1 trigger at a CM energy of 900 GeV. The triangle and the inverted triangles show the default fractions in PHOJET and PYTHIA 6 respectively. The difference between these two points gives an estimate of the systematic uncertainty due to the model dependence of the fractions of SD and DD events.

It is interesting to see that at a given energy, for the same fractions f^{sd} and f^{dd} for PYTHIA 6 and PHOJET in figures 5.1(a) and 5.1(b), the mean multiplicity on the z-axis is different. These differences arise from the differences in the kinematic models used in the MC generators. A comparison and description of the models is presented in 3.2.3.

5.4 Estimate of trigger efficiency and systematics on multiplicity measurement for ALICE publication

The methods described above have been used to calculate trigger efficiencies and as a cross-check on values of systematic error introduced on charged-particle pseudorapidity density published in the initial physics publications of ALICE [4, 5]. The trigger efficiencies have been calculated, and the systematic error on the pseudorapidity distribution has been estimated in this section at 900 GeV and 2.36 TeV.

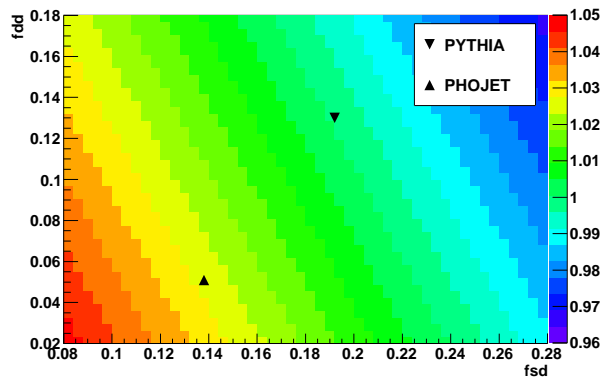### 5.4.1 Trigger Selection Efficiency

In the analysis presented in the first two ALICE physics papers [4, 5], measured fractions of SD and DD events are used to normalise ALICE results to inelastic and NSD event classes. UA5 [77]
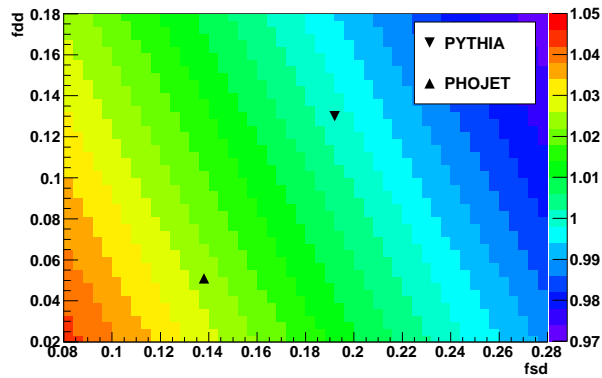
(a) PYTHIA 6
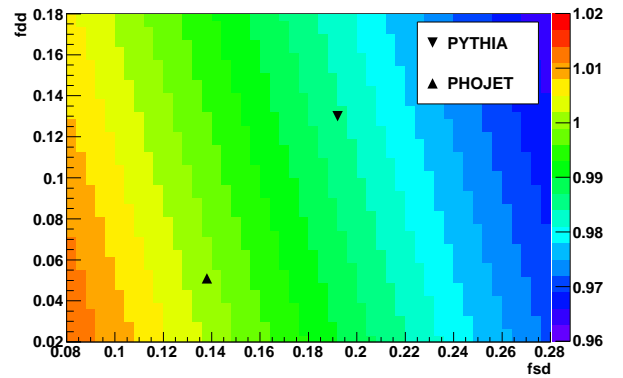
(b) PHOJET

(c) PYTHIA 8

Figure 5.2: Systematics plots with MB1 trigger at a CM energy of 7 TeV. The triangle and the inverted triangles show the default fractions in PHOJET and PYTHIA 6 respectively. The difference between these two points gives an estimate of the systematic uncertainty due to the model dependence of the fractions of SD and DD events.

measurements from $p\bar{p}$ collisions are used for the fractions at 900 GeV. These measurements were made in a diffractive mass range of $M_X^2 < 0.05s$. Since there is a small increase of the relative SD and DD fractions with energy, the closest measured fractions at 1.8 TeV were used for the analysis at 2.36 TeV. For the SD fraction, SD cross-section measurements by the E710 [78] collaboration were used along with a measurement of the inelastic cross-section from CDF and E811 experiments [79]. The DD cross-section was obtained from CDF [80].

Table 1 from the second ALICE publication [5] provides process fractions and selection efficiencies for different process types, and is reproduced in tables 5.9 and 5.10. In table 5.9, the relative fractions of SD and DD are experimental measurements. When the fraction of SD events are varied by 30% due to the uncertainty in the diffractive mass range, the result stays within the quoted systematic error [5]. The ND fraction is calculated as $1 - f^{sd} - f^{dd}$. The MB_{OR} and MB_{AND} triggers have been used for the analyses of the inelastic and NSD event classes at 900 GeV respectively, and are equivalent to the MB1 and V0AND triggers defined in section 5.1. The trigger used for the analyses of data at $\sqrt{s} = 2.36$ TeV is MB_{SPD} which is equivalent to the PIX1 trigger in table 5.1.

Table 5.9: Relative fractions of SD and DD fractions from previous measurements used in the ALICE publication [5].

Energy	Experiment	SD	DD
900 GeV	UA5 [77]	0.153 ± 0.023	0.095 ± 0.060
1.8 TeV	E710 and CDF [78, 79]	0.159 ± 0.024	0.107 ± 0.031

Table 5.10: Selection efficiencies of different event classes using PYTHIA 6 and PHOJET generators [5].

Energy	Trigger	Generator	SD	DD	ND	INEL	NSD
900 GeV	MB_{OR} (MB1)	PYTHIA 6	0.77	0.92	1.00	0.95	
		PHOJET	0.86	0.98	1.00	0.97	
	MB_{AND} (V0AND)	PYTHIA 6	0.29	0.49	0.98		0.92
		PHOJET	0.34	0.77	0.96		0.94
2.36 TeV	MB_{SPD} (PIX1)	PYTHIA 6	0.55	0.63	0.99	0.86	0.94
		PHOJET	0.62	0.79	0.99	0.90	0.97

The SD and DD efficiencies calculated in this thesis (tables 5.2 - 5.5) are the same as those from the ALICE paper [5] in table 5.10 and were used as an independent cross-check during the preparation of the paper. The ND efficiencies in table 5.10 are the sum of the CD and ND efficiencies shown in the tables in section 5.1. The NSD and inelastic efficiencies are calculated as follows:

$$\varepsilon_T^{inel} = f^{sd}\varepsilon_T^{sd} + f^{dd}\varepsilon_T^{dd} + f^{nd}\varepsilon_T^{nd}$$

$$\varepsilon_T^{NSD} = \frac{f^{dd}\varepsilon_T^{dd} + f^{nd}\varepsilon_T^{nd}}{f^{NSD}}.$$

The NSD and inelastic efficiencies in table 5.10 were calculated using the measured f^{sd}, f^{dd} and f^{nd} from table 5.9.

5.4.2 Systematic uncertainty

A list of contributors to the overall systematic uncertainty in the measurements of the charged-particle pseudorapidity density and the multiplicity distribution is listed in table 2 of the ALICE publication [5] and partly reproduced in table 5.11. The method described in section 5.3 was used as an initial estimate of the uncertainty on the charged-particle pseudorapidity density that arises from varying the process fractions (contribution of diffraction) and the kinematics (event-generator dependence). However, it is important to note that the systematics described in the ALICE publication were estimated using SPD tracklets while the estimates presented in the section below use TPC tracks. Additionally, the estimates in this section are purely based on MC, while in the paper, the systematic error was obtained by correcting data with two different MC models. Hence, they are not directly comparable but illustrate the method used.

To estimate the uncertainty arising from the fraction of diffractive events, the kinematics in PYTHIA 6 and PHOJET are used with different fractions f^{sd} and f^{dd} as in section 5.3. Figures 5.3 and 5.4 show how changing the fraction of diffractive events (f^{sd} and f^{dd} on the x and y axes respectively) changes the mean multiplicity with respect to that at the measured UA5 fractions (colour scale on right panel) using the MB1 (MB$_{OR}$) and V0AND (MB$_{AND}$) triggers respectively for PYTHIA 6 and PHOJET. The full circle shows the UA5 measured fractions. The upper limit on the uncer-

Table 5.11: Contributions to systematic uncertainties from diffraction and event-generator dependence in the measurement of charged particle pseudorapidity density from an ALICE publication [5].

Uncertainty	900 GeV	2.36 TeV
Contribution of diffraction (INEL)	0.7%	2.6%
Contribution of diffraction (NSD)	2.8%	2.1%
Event-generator dependence (INEL)	+1.7%	+5.9%
Event-generator dependence (NSD)	-0.5%	+2.6%

tainty in mean multiplicity μ is estimated numerically as

$$\sigma(\mu) = \left| \frac{\partial \mu}{\partial f^{sd}} \right| \sigma(f^{sd}) + \left| \frac{\partial \mu}{\partial f^{dd}} \right| \sigma(f^{dd}) \qquad (5.10)$$

where $\sigma(f^{sd})$ and $\sigma(f^{dd})$ are the errors on the measurements of f^{sd} and f^{dd} from UA5 [77] shown in table 5.9. The open circles with respect to full circles show the change in mean multiplicity between the UA5 fractions and 1 σ of the UA5 fractions as in equation (5.10). Figure 5.3 shows that the mean multiplicity changes by a maximum of around 0.7% in the case of PYTHIA 6 and 0.4% in the case of PHOJET within 1σ of the UA5 measured fractions for inelastic events selected using the MB1 trigger. From figure 5.4, for the NSD event class selected using the V0AND trigger, the uncertainty in mean multiplicity is just over 4% in PYTHIA 6 and around 3% in PHOJET.

(a) PYTHIA 6   (b) PHOJET
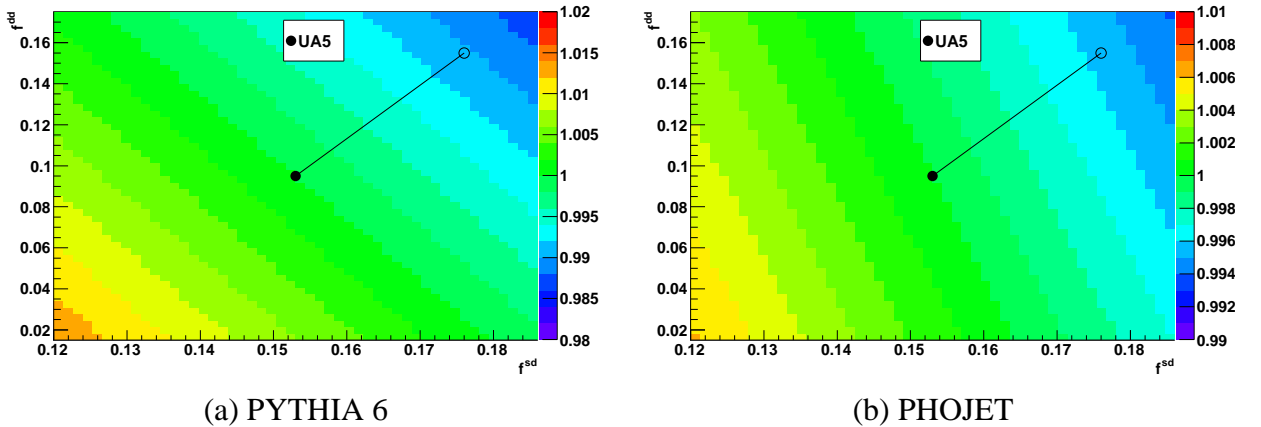
Figure 5.3: Systematics plots with MB1 trigger at a CM energy of 900 GeV for inelastic events. The full circle shows the measured UA5 fraction and the open circle shows 1 σ of the measured fraction which corresponds to the uncertainty in equation (5.10).

Figures 5.5 and 5.6 are similar plots at 2.36 TeV using measured E710 fractions from table 5.9 and
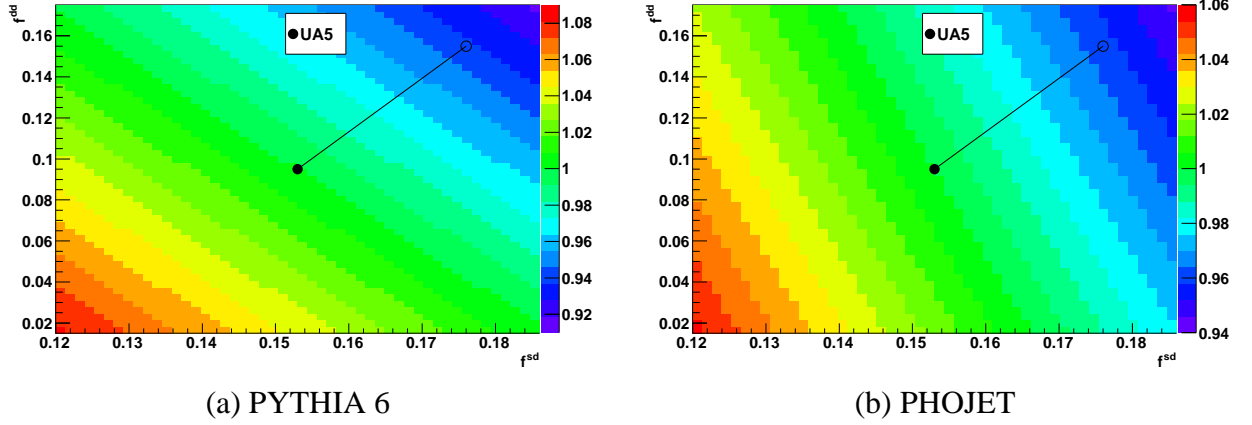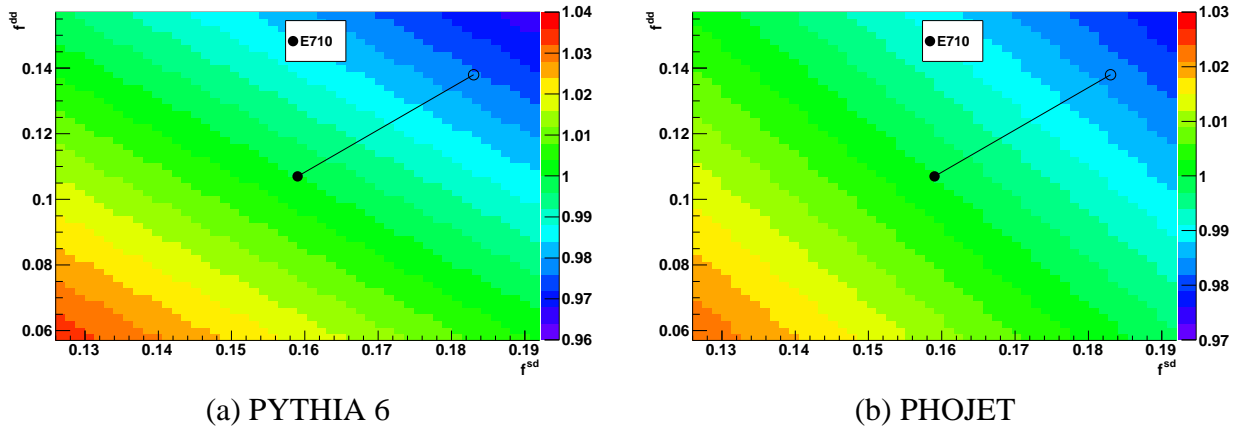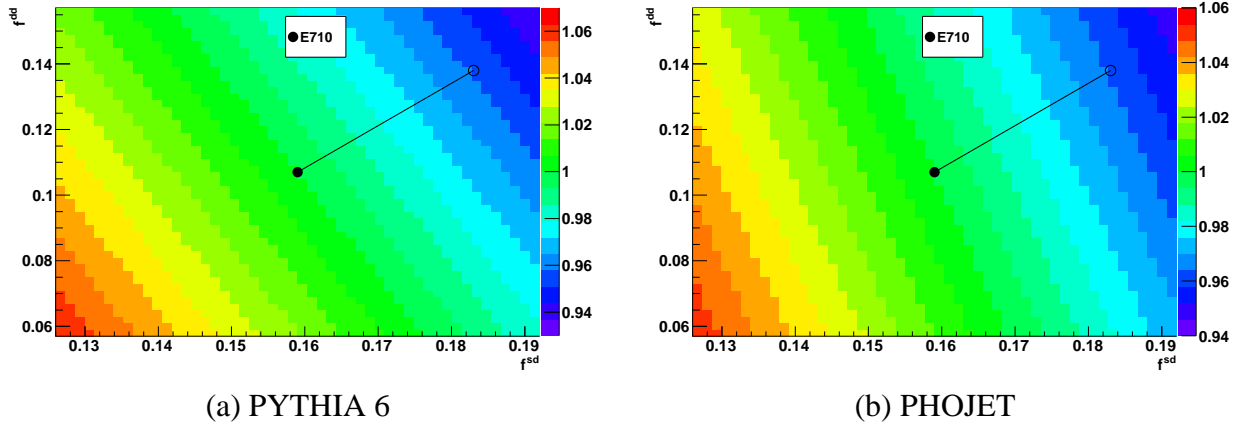
(a) PYTHIA 6   (b) PHOJET

Figure 5.4: Systematics plots with V0AND trigger at a CM energy of 900 GeV for NSD events. The full circle shows the measured UA5 fraction and the open circle shows 1 σ of the measured fraction which corresponds to the uncertainty in equation (5.10).

the PIX1 (MB$_{\mathrm{SPD}}$) trigger condition for inelastic and NSD events respectively. Figure 5.5 shows that the uncertainty from diffractive fractions in inelastic events at 2.36 TeV selected using PIX1 is around 1.7% in PYTHIA 6 and just over 1% in PHOJET. For the NSD event class, from figure 5.6, the uncertainty estimate using PYTHIA 6 is just over 3% and using PHOJET is around 3%.

(a) PYTHIA 6   (b) PHOJET

Figure 5.5: Systematics plots with PIX1 trigger at a CM energy of 2.36 TeV for inelastic events. The full circle shows the measured E710 fraction and the open circle shows σ of the measured fraction which corresponds to the uncertainty in equation (5.10).

To estimate the dependence on event generator kinematics, PYTHIA 6 was corrected with PHO-JET efficiencies and measured fractions. For the case of inelastic events at 900 GeV selected with the MB1 trigger, the difference in mean multiplicity using PYTHIA 6's kinematics is +3.1%, and

(a) PYTHIA 6	(b) PHOJET

Figure 5.6: Systematics plots with PIX1 trigger at a CM energy of 2.36 TeV for NSD events. The full circle shows the measured E710 fraction and the open circle shows 1 σ of the measured fraction which corresponds to the uncertainty in equation (5.10).

for the NSD event class selected with the V0AND trigger, is +2.5%. Similarly, at 2.36 TeV using the PIX1 trigger, the difference in mean multiplicity obtained using PHOJET's efficiencies compared to that obtained using PYTHIA 6's efficiencies is +4.3% for inelastic events and +3.4% for the NSD event class.

These estimates are summarised in table 5.12. They were calculated before data were available as a "dress-rehearsal" for the published analyses. In the ALICE publication [5], tracklets were used for multiplicity measurements along with a more thorough differential approach in multiplicity to estimate the systematic uncertainty in the charged particle pseudorapidity density distribution. The systematic uncertainty estimates obtained by both methods are comparable.

Table 5.12: Contributions to systematic uncertainties from diffraction and event-generator dependence in the measurement of charged particle pseudorapidity density.

Uncertainty	900 GeV	2.36 TeV
Contribution of diffraction (INEL)	0.4% to 0.7%	1% to 1.7%
Contribution of diffraction (NSD)	3% to 4%	3%
Event-generator dependence (INEL)	+3.1%	+4.3%
Event-generator dependence (NSD)	+2.5%	+3.4%

5.5 Summary

Triggers are not 100% efficient. Hence, trigger corrections need to be applied, which are different for different triggers and event classes. Since trigger corrections are model dependent, PYTHIA 6 and PHOJET generators, which differ in both the fractions of diffractive events and their kinematics, are compared. In order to separate the contributions towards systematic uncertainty on a measurement (eg, the mean multiplicity), from fractions and kinematics, we vary fractions with the kinematics from the same model. When fractions in the two event generators are identical, the difference in trigger efficiencies is purely due to a difference in the kinematics of the models. A kinematic comparison of PYTHIA 6 and PHOJET is presented in section 3.2.3.

At a given energy PHOJET efficiencies for diffractive events are higher than those for PYTHIA 6. This is because PHOJET has a hard diffractive component, while PYTHIA 6 does not. Comparing efficiencies in the same generator at different energies shows that efficiencies increase with energy as charged particle multiplicities also increase.

This chapter also presents an estimate of the uncertainty on the number of charged particle tracks using the kinematics model of one generator with the default fractions of another, while varying the diffractive cross-section. For inelastic events at $900\,\mathrm{GeV}$ selected using the MB1 trigger, the uncertainty is between 2%-6%, while the uncertainty is under 3% for the same event class at $7\,\mathrm{TeV}$.

For the first ALICE publications, measured fractions of SD and DD were taken from previous experiments and two models, PYTHIA 6 and PHOJET, were used. At $900\,\mathrm{GeV}$, the efficiency of selecting inelastic events using the MB1 trigger is 95%-97% and the efficiency for selecting NSD events with the V0AND trigger is 92%-94% depending on the event generator used. In the case of $2.36\,\mathrm{TeV}$, the efficiency of selecting inelastic events using the PIX1 trigger is 86%-90% and that for NSD events using the same trigger is 94%-97%. The efficiencies presented in section 5.1 were used in the first ALICE publications. A method to estimate systematic uncertainties from fractions and kinematics was presented in section 5.4. The uncertainty due to the relative fractions of diffractive events is between 0.4% and 0.7% in the inelastic event class and 3%-4% in the NSD event class at $900\,\mathrm{GeV}$. At $2.36\,\mathrm{TeV}$, the systematic uncertainty due to the relative fractions

of diffractive events is between 1%-1.7% and around 3% for the inelastic and NSD event classes respectively. The uncertainty due to the kinematic models in the MC generators used is estimated as 2.5%-3.1% at 900 GeV and 3.4%-4.3% at 2.36 TeV respectively for the two event classes.

DIFFRACTIVE DATA IN ALICE

This chapter describes the final part of my thesis work and compares MC models to data enhanced in SD diffraction. Data are initially selected with an offline trigger with a high acceptance for diffractive events and a low acceptance for non-diffractive events. Standard ALICE track and vertex selection cuts are applied to this sample. Transverse momentum p_T, pseudorapidity η and charged particle multiplicity distributions of this diffractive sample are then compared to similar distributions obtained by projecting MC models onto data, satisfying the same offline trigger condition. The distributions from MC generators are 'corrected' for detector effects and compared to uncorrected data. A partial study of systematic effects has been performed. Systematic uncertainties on the comparison are estimated by examining track and vertex cuts only. Possible additional sources related to the detector have been considered in the ALICE publication [5]. No systematic uncertainty on the MC models is assigned as uncorrected data are compared to models directly.

The chapter starts off by examining potential offline triggers. This is followed by a discussion of the data that are being analysed along with the offline trigger that enhances diffraction. The next section examines the standard ALICE track and vertex cuts, comparing data and MC for each of the variables. Then, the cuts that are used are varied and their effect on the resulting p_T, η and multiplicity spectra is taken as a measure of the systematic uncertainty. Finally, correlations between these variables are estimated to combine uncertainties. The p_T, η and multiplicity distributions of data and MC are presented with a total systematic uncertainty.

6.1   Selection of a diffractive sample

Diffractive events produce more particles in the forward regions in pseudorapidity and are char-
acterised by a rapidity gap that depends on the diffractive mass (M_X) as $\Delta\eta = -\ln(M_X^2/s)$. SD
events have an asymmetric topology with more activity on one side of η than the other, while
DD events produce activity on both sides of η. However, both SD and DD events have a rapidity
gap. Keeping this topology in mind, four new triggers for the sake of diffractive studies are shown
in table 6.1. In the section, "trigger" refers to an offline selection of diffractive events. The diff
trigger is defined so that it selects both SD and DD events; the Ddiff trigger requires a hit in both
the V0 counters, so it should select DD events; the Sdiff trigger requires a hit in only one of the
V0 counters, so it should select SD events. All these triggers require no hit in the SPD, imposing
a rapidity gap of 1.6 units at central rapidity. The MBV0diff trigger on the other hand does not
impose a rapidity gap at mid-rapidity. However, it is an asymmetric trigger intended to have a
high selection efficiency for SD events. For each of these triggers, we calculate the efficiencies
for the different process types using the generators PYTHIA 6, PYTHIA 8 and PHOJET at a CM
energy of 7 TeV. The MC event samples used here are the same as in chapter 5.

Table 6.1: Diffractive trigger definitions.

diff	= $\overline{\text{GFO}}$ and V0OR
Ddiff	= $\overline{\text{GFO}}$ and V0AND
Sdiff	= $\overline{\text{GFO}}$ and V0OR and $\overline{\text{V0AND}}$
MBV0diff	= ($\overline{\text{V0A}}$ or $\overline{\text{V0C}}$) and MB1
	(MB1 = SPD or V0OR)

Table 6.2 shows the efficiencies (given by ε_T^{proc} in equation (5.4)) for the four diffractive triggers
defined in table 6.1. The SD and DD efficiencies for all diffractive triggers are clearly higher than
for ND events. The Sdiff trigger is more inclusive compared to the Ddiff trigger, and has similar
efficiencies for both SD and DD events. However, the Ddiff trigger clearly enhances DD events.
Among all the diffractive triggers considered, the MBV0diff trigger has the highest efficiency for
selecting SD and DD events. It is also interesting to note that this is the only trigger among the
four diffractive triggers defined which still allows tracks in the central region. This makes the

Table 6.2: Diffractive trigger efficiencies at 7 TeV expressed as percentages. Statistical uncertainties shown as 0.0 are less than 0.05.

Trigger	SD	DD	CD	ND	NSD	INEL
PYTHIA 6						
diff	21.3±0.1	29.8±0.1		1.4±0.0	6.0±0.0	8.9±0.0
Ddiff	2.9±0.0	9.7±0.1		0.9±0.0	2.3±0.0	2.4±0.0
Sdiff	18.4±0.1	20.1±0.1		0.5±0.0	3.6±0.0	6.5±0.0
MBV0diff	34.0±0.1	39.6±0.1		1.9±0.0	8.0±0.0	13.1±0.0
PHOJET						
diff	21.4±0.1	22.0±0.1	30.0±0.2	0.7±0.0	2.4±0.0	5.1±0.0
Ddiff	0.7±0.0	8.3±0.1	0.8±0.0	0.5±0.0	1.0±0.0	0.9±0.0
Sdiff	20.8±0.1	13.7±0.1	25.1±0.2	0.2±0.0	1.5±0.0	4.1±0.0
MBV0diff	38.2±0.1	26.4±0.1	60.6±0.3	1.1±0.0	3.7±0.0	8.5±0.0
PYTHIA 8						
diff	18.0±0.2	26.8±0.3		0.2±0.0	4.5±0.1	7.1±0.1
Ddiff	0.3±0.1	6.1±0.2		0.2±0.0	1.1±0.0	1.0±0.0
Sdiff	17.7±0.2	20.7±0.3		0.02±0.0	3.3±0.1	6.1±0.1
MBV0diff	33.9±0.2	41.3±0.3		0.4±0.0	7.0±0.0	12.1±0.0

MBV0diff trigger the obvious choice to study a sample of diffractive events. Table 6.3 shows the fraction of events of a particular process type 'proc' ($\frac{N_{proc}}{N_{events}}$) and the fraction of triggered events that are of a particular process type ($\frac{N_{proc,trig}}{N_{trig}}$) using all three event generators PYTHIA 6, PYTHIA 8 and PHOJET.

Table 6.3: Fractions of SD, DD and ND events in MBV0diff triggered events using MC models, expressed as percentages. Statistical uncertainties shown as 0.0 are less than 0.05.

MC model	proc	$\frac{N_{proc}}{N_{events}}$	$\frac{N_{proc,trig}}{N_{trig}}$
PYTHIA 6	SD	19.3 ± 0.0	50.8 ± 0.1
	DD	13.0 ± 0.0	39.3 ± 0.1
	ND	67.7 ± 0.0	9.9 ± 0.1
PHOJET	SD	13.8 ± 0.0	61.9 ± 0.2
	DD	5.1 ± 0.0	15.8 ± 0.1
	ND	79.4 ± 0.0	10.2 ± 0.1
	CD	01.7 ± 0.0	12.1 ± 0.1
PYTHIA 8	SD	19.1 ± 0.0	44.5 ± 0.4
	DD	13.0 ± 0.0	36.9 ± 0.4
	ND	67.9 ± 0.2	18.6 ± 0.3

It is seen in table 6.3 that while the fraction of single diffractive events produced is between 14%

and 20 % depending on which MC model is used, about 45% to 62% of the events selected by the MBV0diff trigger are single diffractive. Over 60% of CD events are triggered in PHOJET, resulting in a 12% population of CD events in the sample of triggered events.

6.2 Data selection

The data analysed in this chapter are from ALICE run 125849, collected on the 12th of July 2010. The choice of run is based on the understanding of detector performances both online and offline. Data were collected at a magnetic field of 0.5 T at a centre of mass energy of 7 TeV. There were 6 interacting bunches per beam. The typical bunch intensity for collisions was 0.9×10^{10} protons per bunch resulting in a luminosity of around $10^{28}\,\mathrm{cm}^{-2}\mathrm{s}^{-1}$. The average number of interactions per bunch crossing (μ) is 0.03.

Data were collected with a trigger (cint1b) requiring a hit in the SPD or in either one of the VZERO counters, in coincidence with signals from the two beam pick up counters (BPTX). The BPTX lie on either side of the interaction point and indicate the presence of a bunch. A total of 2.1 million events were recorded at a rate of 640 Hz. Events in coincidence with only one passing bunch on each side (cint1a and cint1c) and with no passing bunches (cint1e) were also registered. These "control triggers" can be used to measure the beam-induced background. The background fraction is defined as

$$\text{Background} = \frac{\text{cint1c} + \text{cint1a} - \text{cint1e}}{\text{cint1b}}$$

Beam induced background is less than 8×10^{-3}% for the 'cint1b' trigger.

Once the data were collected and written to tape, the 'offline' MBV0diff trigger was used to select an event sample enhanced in diffraction. The beam induced background is less than 0.1% for the MBV0diff trigger calculated as

$$\text{Background} = \frac{\text{MBV0diff and cint1c} + \text{MBV0diff and cint1a} - \text{MBV0diff and cint1e}}{\text{MBV0diff}}.$$

The following analysis is based on 2 million events of data collected by ALICE, 2 million events generated by PYTHIA 6 and PHOJET, and 160,000 events generated by PYTHIA 8. Comparisons are made between data and each MC model in multiplicity, p_T and η distributions. Poisson errors are propagated bin by bin and all plots are normalised to the number of events in data.

Figures 6.1 to 6.3 show the multiplicity, p_T and η distributions of events selected with the MBV0diff trigger for both data and MC, with each process in MC shown separately. Inelastic events are labelled as 'MC sum'. It is clear also from these figures that the MBV0diff trigger selects mainly diffractive events. The MC curves corresponding to SD, DD and ND are normalised to the relative fraction of the process type. The multiplicity and p_T plots for PYTHIA 6 show a clear drop for diffractive processes, highlighting the lack of a hard-diffractive part in PYTHIA 6.

6.3   Track and vertex Cuts

The standard track cuts recommended for the selection of primary tracks in the analyses of pp data ensure that tracks are selected with at least one point in the SPD. The distance of closest approach (DCA) between the track and the primary vertex is used to control the background and the number of secondaries selected, using the projections of the DCA in the transverse plane relative to the beam (DCAXY or d_0) and in the direction of the beam (DCAZ). The transverse impact parameter of a track is the projection of the vector connecting the primary vertex and the point of the track's closest approach to the vertex, on the plane perpendicular to the beam. The transverse impact parameter with respect to the primary vertex must be smaller than 7 σ of the resolution for this track. In addition to the standard TPC and ITS quality cuts (TPSRefit and ITSRefit), the recommended TPC track quality cuts for these data listed below are implemented.

The track cuts for the TPC are:

1. Minimum number of clusters (*MinNClustersTPC*) is 70.
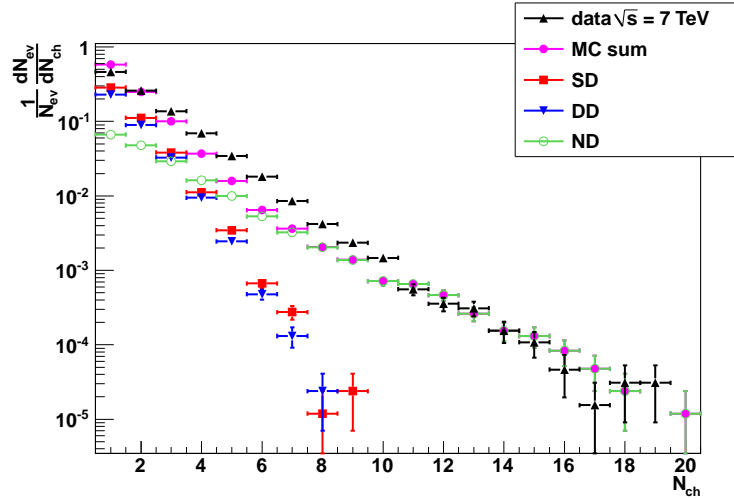
(a) Data and PYTHIA 6.
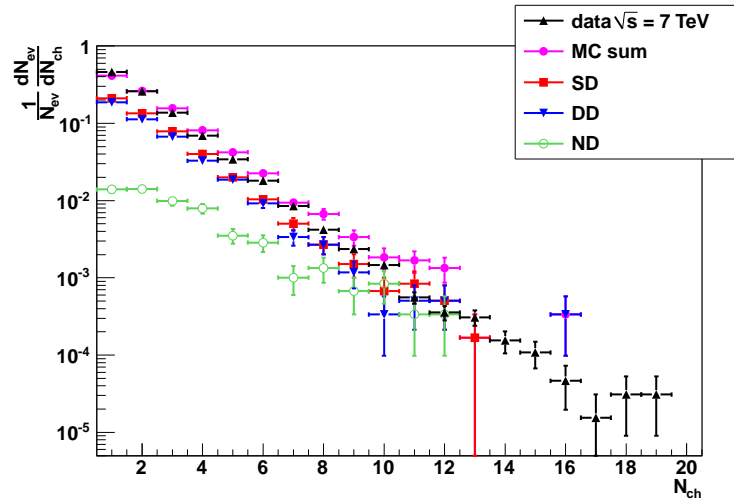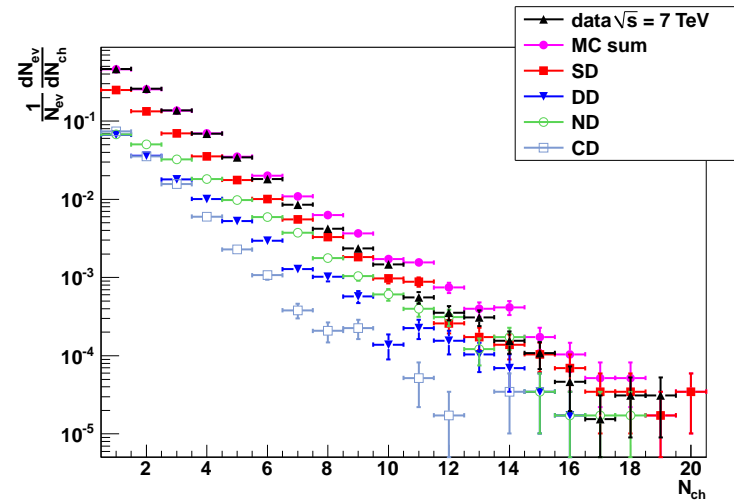
(b) Data and PYTHIA 8.

(c) Data and PHOJET.

Figure 6.1: Multiplicity distributions of data and MC selected with the MBV0diff trigger for different process types.
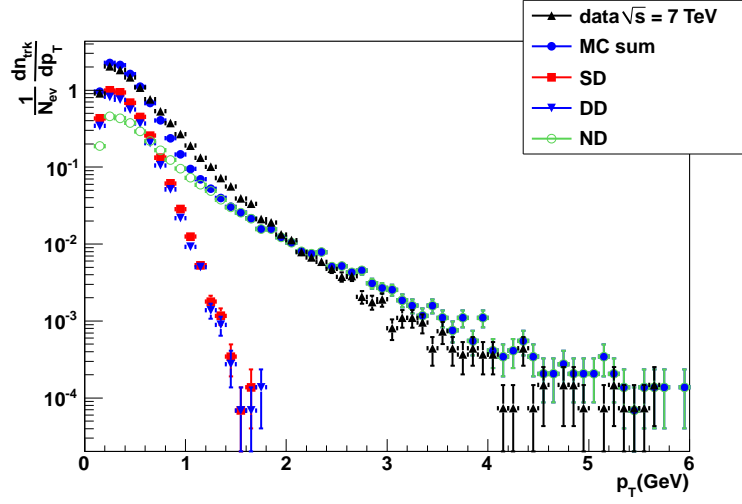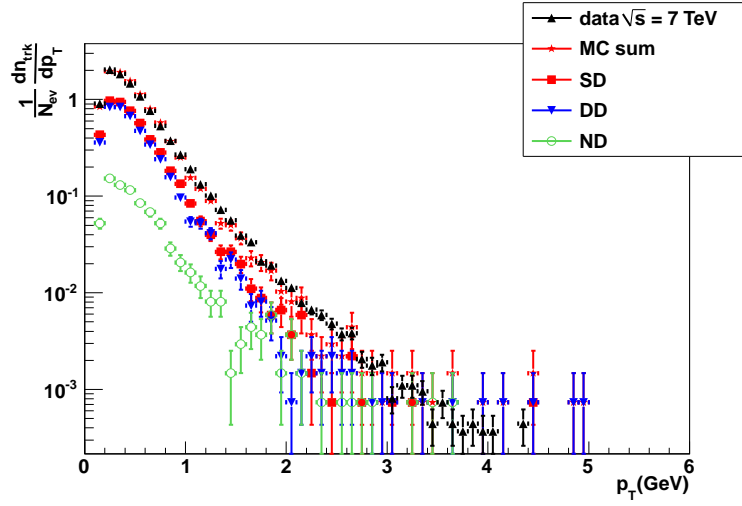
(a) Data and PYTHIA 6.
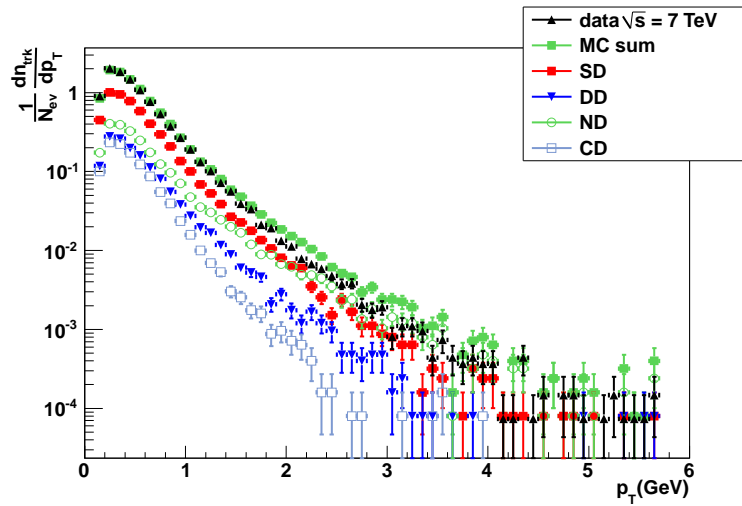
(b) Data and PYTHIA 8.

(c) Data and PHOJET.

Figure 6.2: p_T distributions of data and MC selected with the MBV0diff trigger for different process types.
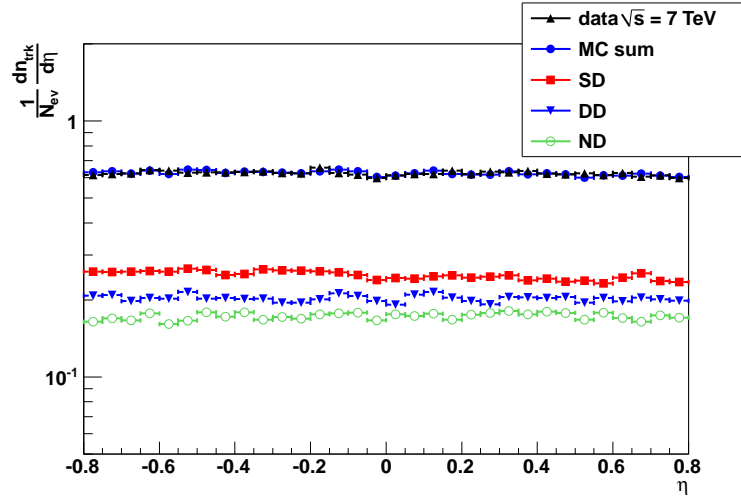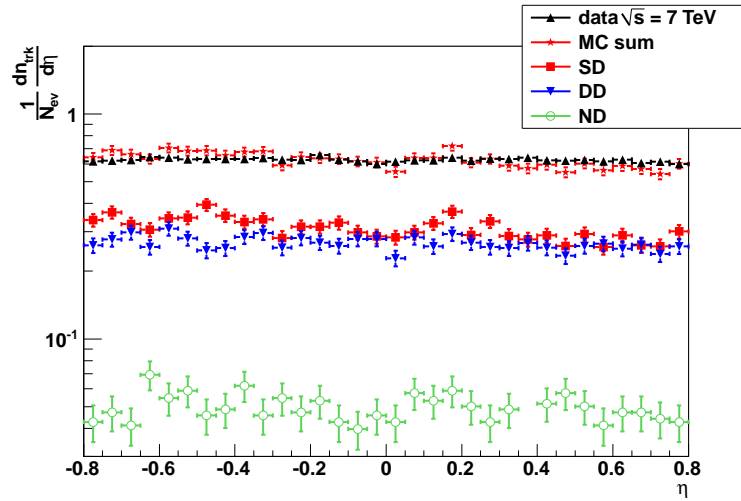
(a) Data and PYTHIA 6.

(b) Data and PYTHIA 8.
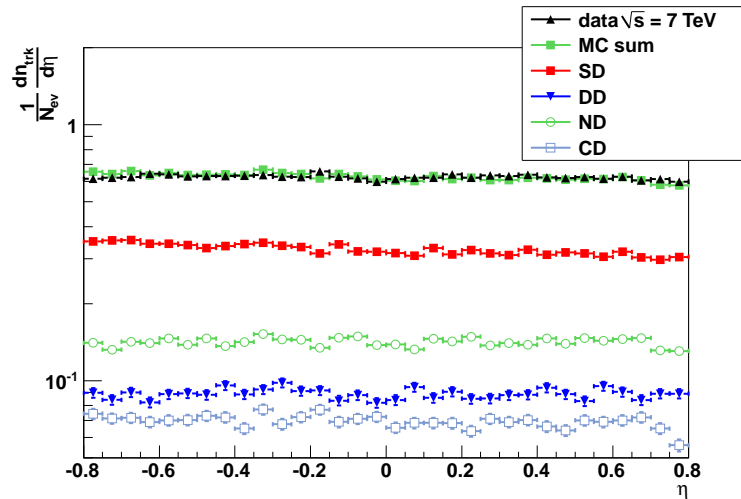
(c) Data and PHOJET.

Figure 6.3: Pseudorapidity distributions of data and MC selected with the MBV0diff trigger for different process types.

2. Maximum χ^2 per cluster (*MaxChi2PerClusterTPC*) is 4.

The primary vertex, in the first instance, is obtained from Event Summary Data (ESD) global tracks. If the ESD vertex is not reconstructed, a vertex from the SPD tracklets is used. If unsuccessful, finally, a TPC vertex is used.

The track-to-vertex cuts are:

1. p_T-dependent cut on transverse impact parameter d_0 such that

   $|d_0| < 7(0.0026\,\mathrm{cm} + 0.0050\,\mathrm{cm}/p_T^{1.01})$ where p_T is in GeV/c.

2. Maximum DCAZ (*MaxDCAToVertexZ*) is 2 cm.

In addition, only tracks with $p_T > 150\,\mathrm{MeV/c}$ and $|\eta| < 0.8$ are considered.

Table 6.4 shows the fraction of events selected by the MBV0diff trigger, with at least one track that passes the cuts above. The values in this table represent the population of the different process types in figures 6.1 to 6.3.

Table 6.4: Fraction of events triggered by the MBV0diff trigger passing the track and vertex quality cuts, expressed as percentages. Statistical errors of 0.0 are less than 0.05.

MC model	proc	≥ 1 track & MBV0diff
PYTHIA 6	SD	45.0 ± 0.2
	DD	37.4 ± 0.2
	ND	18.4 ± 0.2
PHOJET	SD	53.0 ± 0.3
	DD	14.2 ± 0.2
	ND	19.3 ± 0.2
	CD	13.5 ± 0.2
PYTHIA 8	SD	50.4 ± 0.9
	DD	43.8 ± 0.8
	ND	5.8 ± 0.3

After these track and vertex cuts, the MBV0diff trigger selects 4.3%, 3.0% and 4.3% of generated

events that satisfy the cint1b trigger in PYTHIA 6, PHOJET and PYTHIA 8 MC models respectively compared to 3.5% of MB data recorded with the MBV0diff trigger.

6.4 Systematic uncertainty on the measurements

The detection efficiency depends on many factors, like the position of the interaction point or vertex and the momenta of particles produced in the interaction. To estimate the systematic uncertainty on measurements due to track and vertex reconstruction, each variable that appears in the track and vertex cuts is plotted for data and MC. For those variables where data and MC differ significantly, the difference between different cuts on the same variable is taken as an estimate of the systematic uncertainty on that variable.

6.4.1 Track Cuts

In this section various track related variables are plotted for data and MC, for events that satisfy the cint1b trigger and for those that satisfy the MBV0diff diffractive trigger, looking at the data as a whole and in particular at the diffraction enriched sample.

Figures 6.4(a) and 6.4(b) show the distribution of the number of clusters in the TPC detector (*NClustersTPC*) for events that satisfy the cint1b described in section 6.2 and MBV0diff trigger conditions respectively. The recommended cut on the minimum number of TPC clusters for a track is set at 70. There is good agreement among the three MC models. Data and MC are in good agreement in the most populated regions of the *NClustersTPC* plot, while there is 20% discrepancy in the tails of the distribution. As an estimate of systematics, the p_T, η and multiplicity spectra for MC, that satisfy the MBV0diff trigger, are compared at different *NClustersTPC* cuts. In figure 6.5 the cut on the minimum number of TPC clusters is increased to 75 and multiplicity, p_T and η distributions are compared with those at the standard cut of 70. These estimates are made using the PHOJET model. There is no systematic effect on the observed shape. The difference in absolute normalisation from changing the cut is less than 0.5%.

(a) Events selected by cint1b trigger.	(b) Events selected by the MBV0diff trigger.
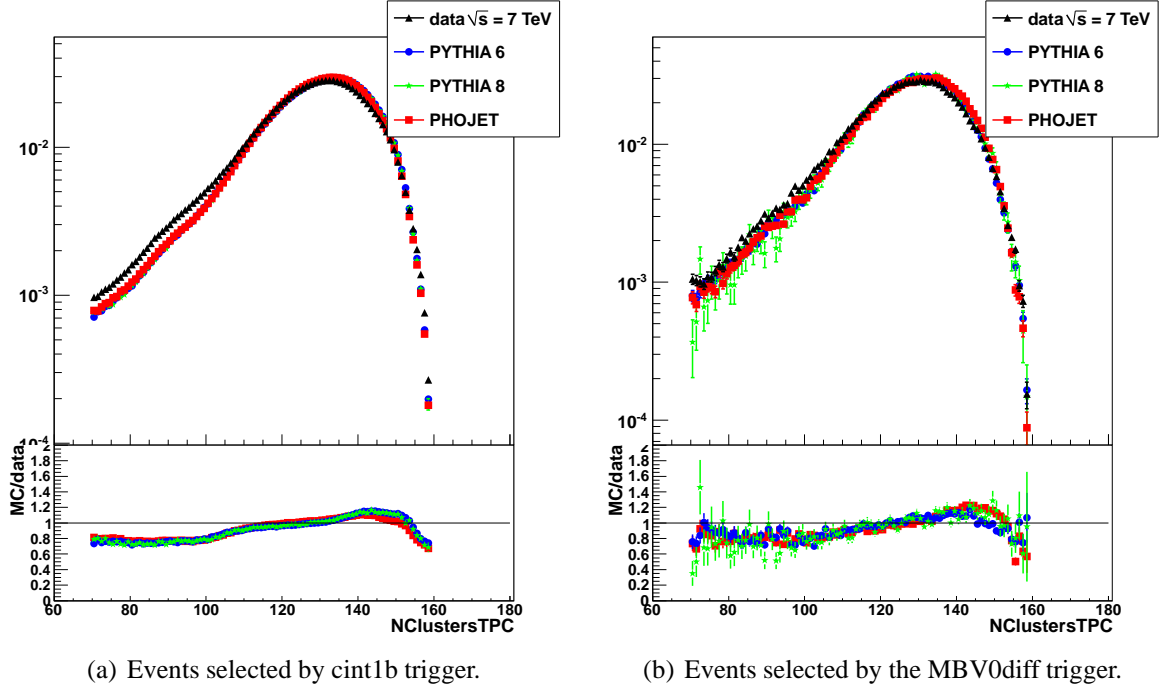
Figure 6.4: Distributions of number of TPC clusters. The bottom panel shows the ratio of MC and data.

The next variable to consider is the maximum χ^2 per TPC cluster (*MaxChi2PerClusterTPC*). The recommended cut on this variable is 4. Figures 6.6(a) and 6.6(b) show the χ^2 per TPC cluster distributions for events that satisfy the cint1b and the MBV0diff trigger conditions respectively. The distributions appear to be shifted by 0.4 units. The systematic uncertainty is estimated by varying the χ^2 per cluster of the TPC from 4 to 4.4 for events satisfying the MBV0diff trigger. Figure 6.7 shows the effect of this cut on the measured p_T, η and multiplicity spectra using the PHOJET model. Changing the maximum χ^2 per TPC cluster cut has no effect on the shape of the p_T, multiplicity and η distributions. The uncertainty from the absolute normalisation of the number of events is negligible.

6.4.2 Vertex Cuts

Although there is no explicit cut on the vertex, the positions of the reconstructed vertices in data and MC are compared as they may affect the charged-particle distribution of events satisfying the MBV0diff trigger. The primary vertex can be reconstructed from information from different detectors. The three reconstruction methods available are
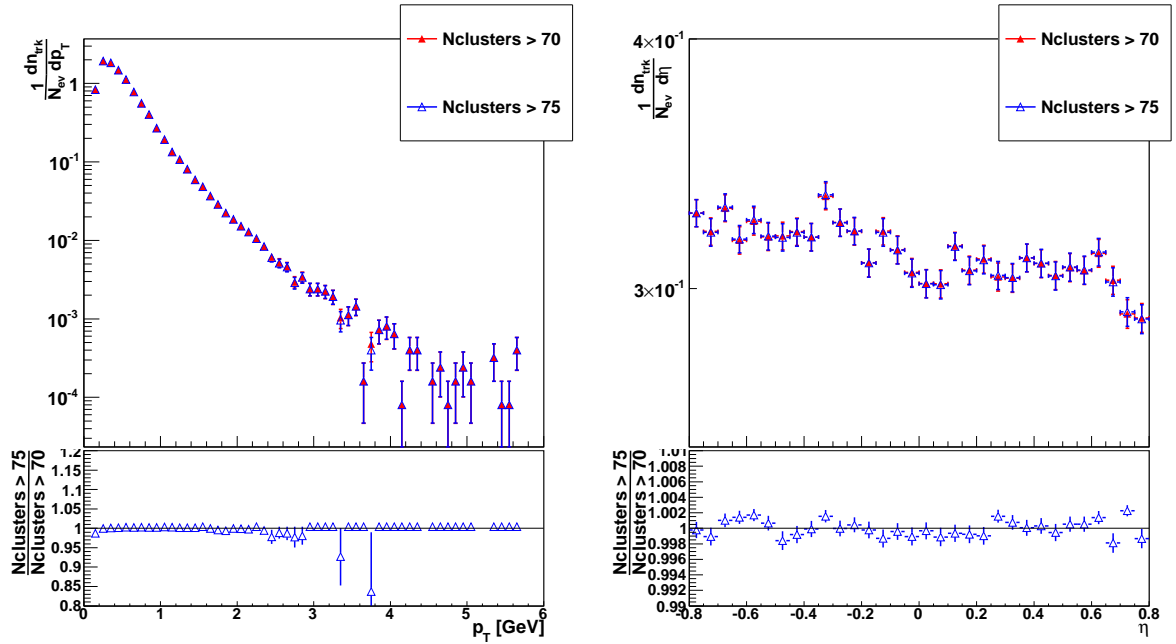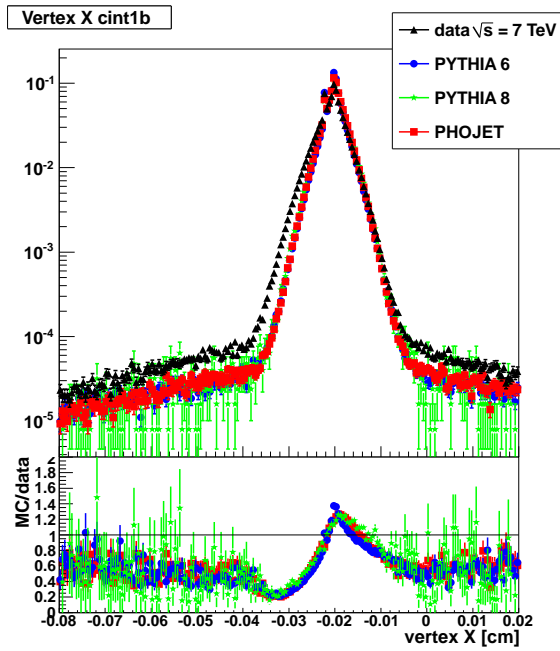
(a) p_T distribution.
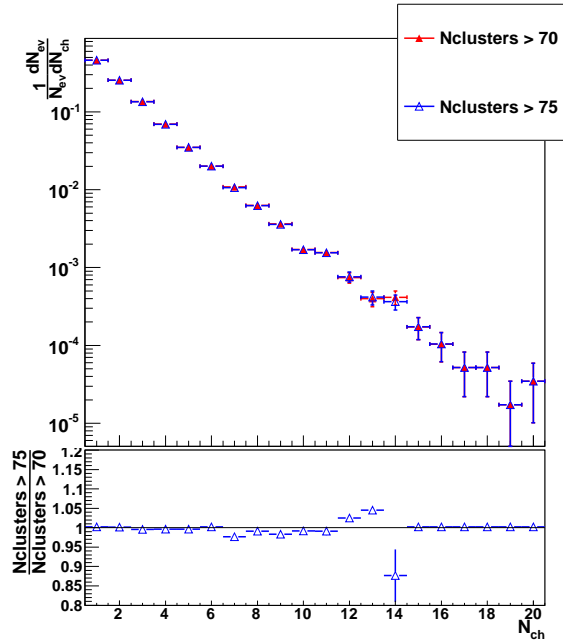
(b) η distribution.

(c) N_{ch} distribution.

Figure 6.5: Distributions of p_T, η and N_{ch} for PHOJET events at different *NClustersTPC* cuts. The bottom panel shows the ratio of two different cuts on the minimum number of TPC clusters.
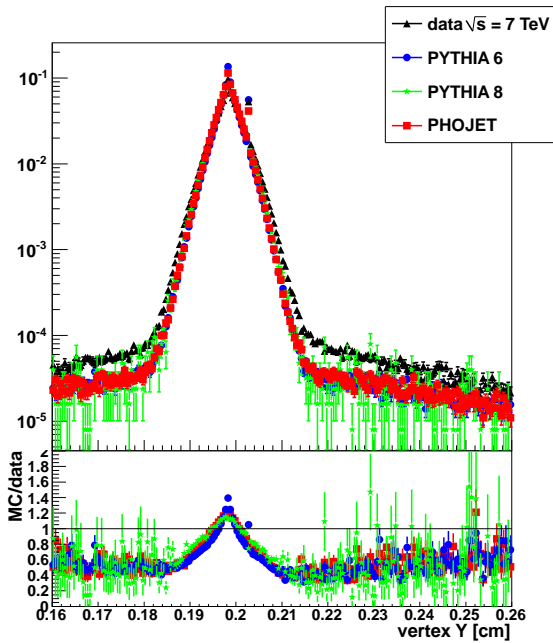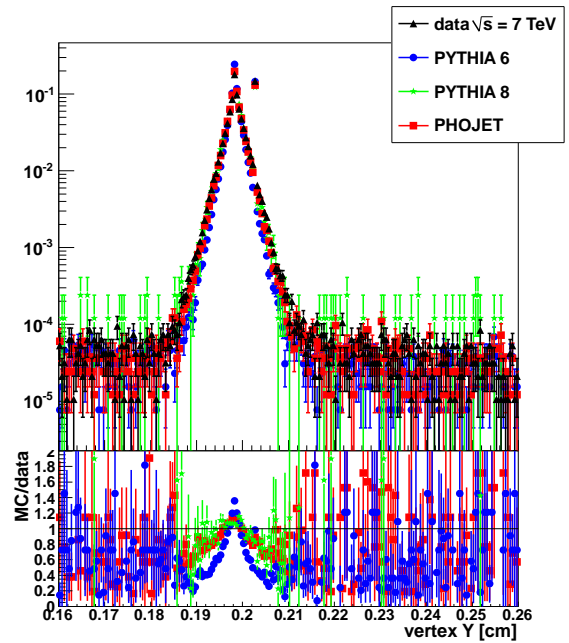
(a) Events selected by cint1b trigger.

(b) Events selected by the MBV0diff trigger.
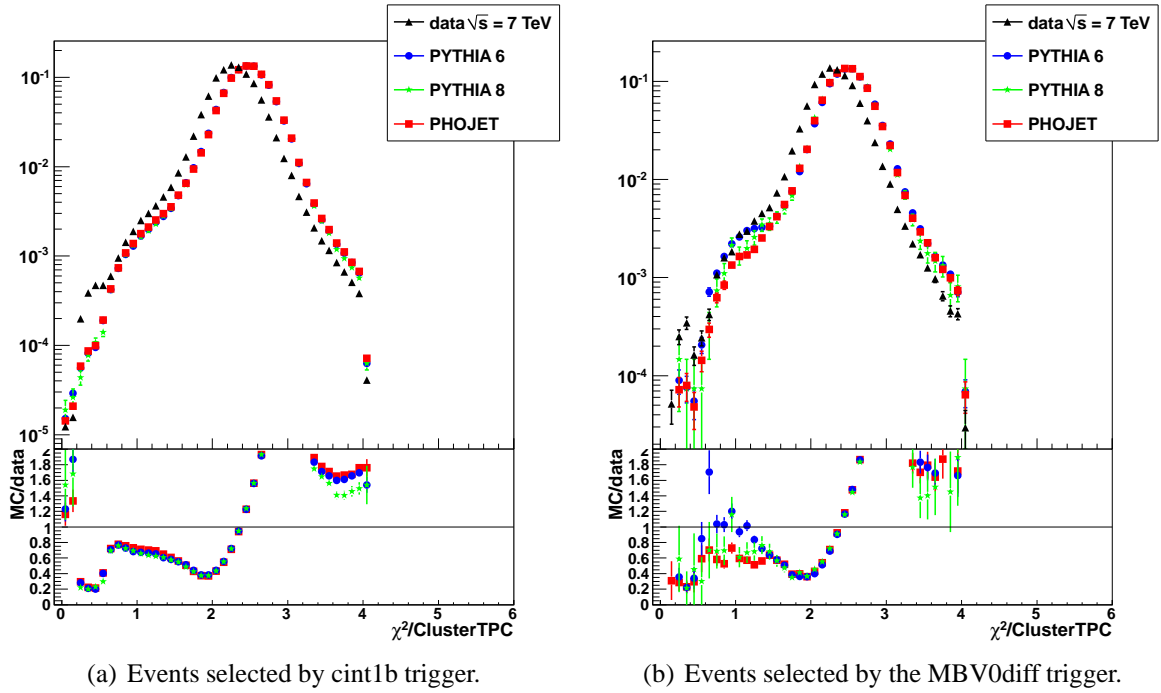
Figure 6.6: Distributions of χ^2 per cluster in the TPC. The bottom panel shows the ratio of MC and data.

1. PrimaryVertexTracks - reconstruction after tracking, using ESD tracks with points in the ITS and TPC

2. PrimaryVertexSPD - reconstruction before tracking, using correlations of SPD points

3. PrimaryVertexTPC - reconstructed after tracking, using TPC-only tracks

The vertex reconstructed for data and MC in this study uses the first successful reconstruction method among the above three methods, applied in the same order. Figures 6.8 to 6.10 show the x, y and z positions respectively of the reconstructed primary vertex in data and MC for the cint1b selection and the MBV0diff selection of events for PYTHIA 6 , PYTHIA 8 and PHOJET. The little peaks seen in figure 6.8 around -0.025 cm and in figure 6.9 between 0.2 cm and 0.21 cm are the default values assigned in the case of the failure of the vertexer in all three methods above.

Figures 6.11 and 6.12 show the distributions of the x and y positions of the generated vertex in the MC model PHOJET and the reconstructed vertices from both the MC and data. The observed shape of the reconstructed vertex is the effect of the beam constraint used in vertex reconstruction.

100
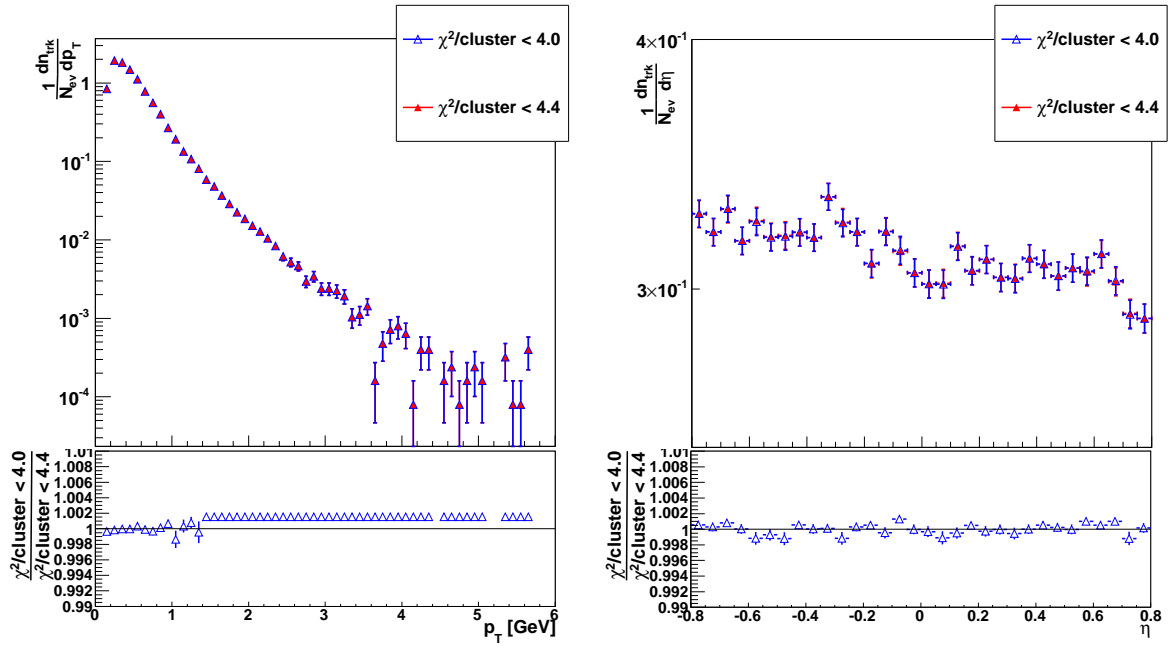
(a) p_T distribution.
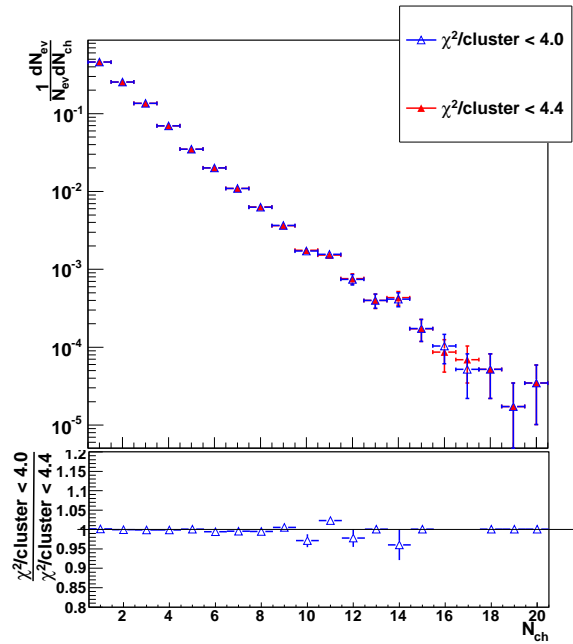
(b) η distribution.

(c) N_{ch} distribution.

Figure 6.7: Distributions of p_T, η and N_{ch} for PHOJET events at different cuts for $\chi^2/cluster$ of the TPC. The bottom panel shows the ratio of two different cuts on the maximum value of χ^2 per TPC cluster.

(a) Events selected by cint1b trigger.
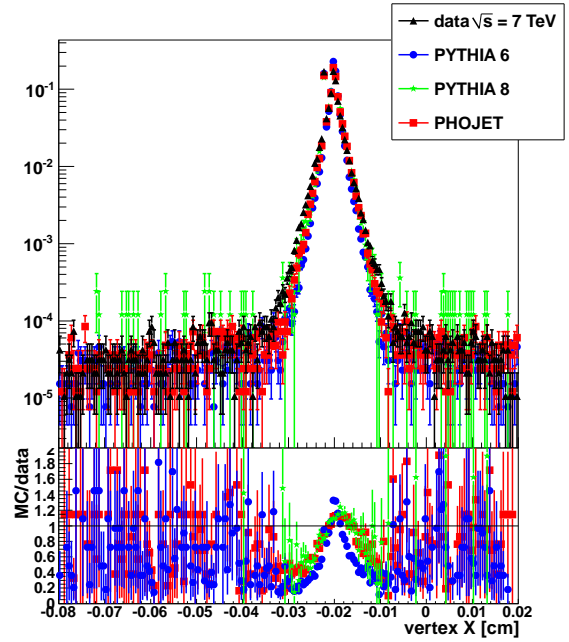
(b) Events selected by the MBV0diff trigger.

Figure 6.8: Distribution of the *x* position of the vertex. The bottom panel shows the ratio of MC and data.

(a) Events selected by cint1b trigger.

(b) Events selected by the MBV0diff trigger.

Figure 6.9: Distribution of the *y* position of the vertex. The bottom panel shows the ratio of MC and data.

(a) Events selected by cint1b trigger. (b) Events selected by the MBV0diff trigger.
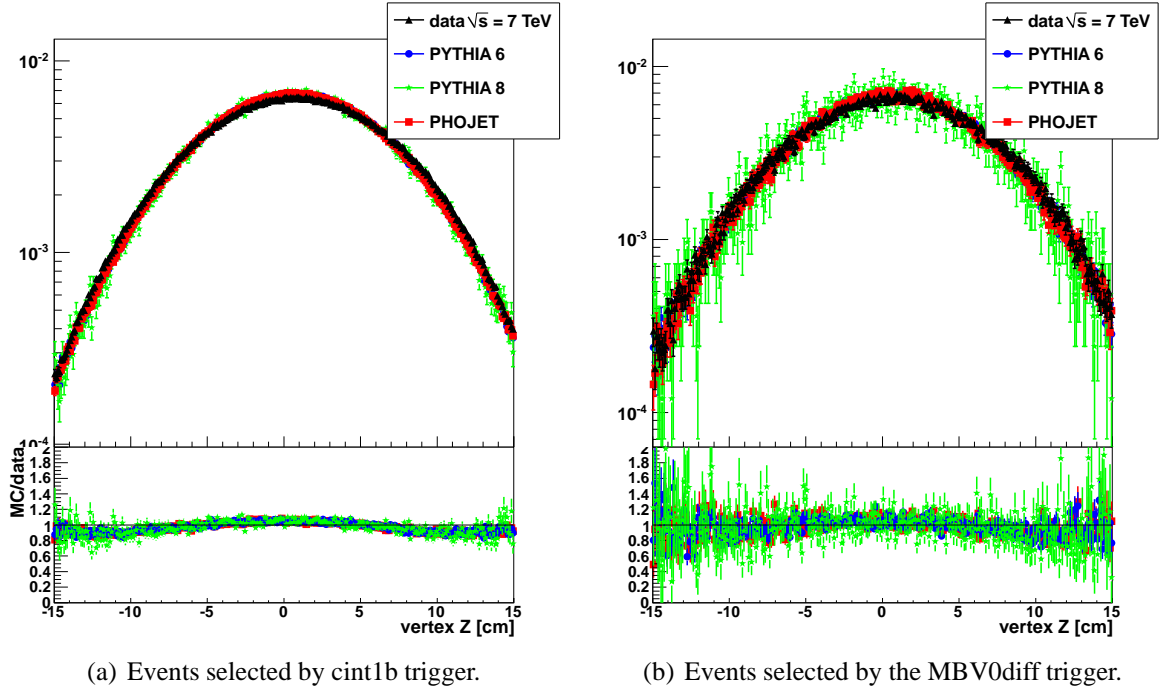
Figure 6.10: Distribution of the z position of the vertex. The bottom panel shows the ratio of MC and data.

In low multiplicity events with a few tracks, the effect of the constraint is more significant and the primary vertex is pulled to the centre of the luminous region.

To gain a measure of the systematic uncertainty from the vertex position and distribution, a cut of 1σ is applied on the generated vertex in the MC. Only those events that pass this cut are reconstructed. Figure 6.13 shows the p_T, η and multiplicity spectra for events that satisfy the MBV0diff trigger, for a sample with the full Gaussian vertex distribution compared with a sample of events that pass a 1σ cut on the generated vertex. The figures shown use the PHOJET MC model. In order to compare the two data sets, which are not independent, the difference between the pseudorapidity density, the momentum and the multiplicity spectra of the two different vertex distributions are studied. The differences in these spectra, called residuals, are measured bin by bin in units of the binomial statistical error of that bin. Figures 6.14(a) to 6.14(c) show a Gaussian fit to the residuals in the p_T, η and multiplicity distributions. The mean values from the fit are -0.16±0.08, -0.10±0.34 and 0.14±0.39, and the standard deviations are 0.49±0.13, 0.97±0.53 and 0.92±0.66 for p_T, η and multiplicity respectively. These values show that the two vertex distributions are compatible. Hence, no systematic error from the vertex position is assigned to the p_T, η and multiplicity distributions.
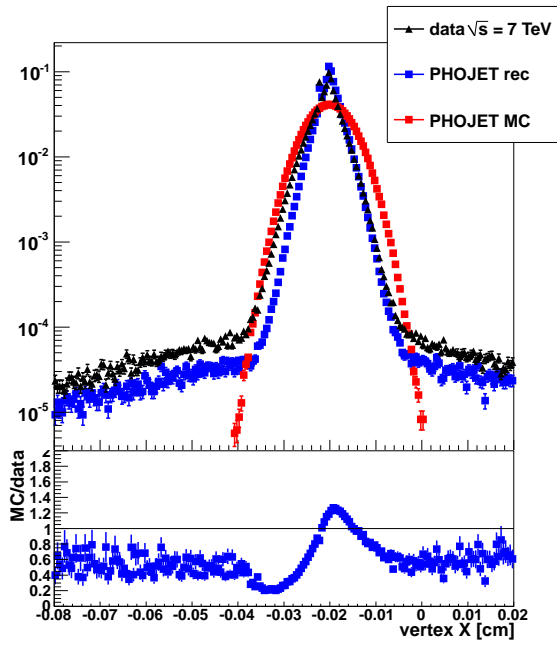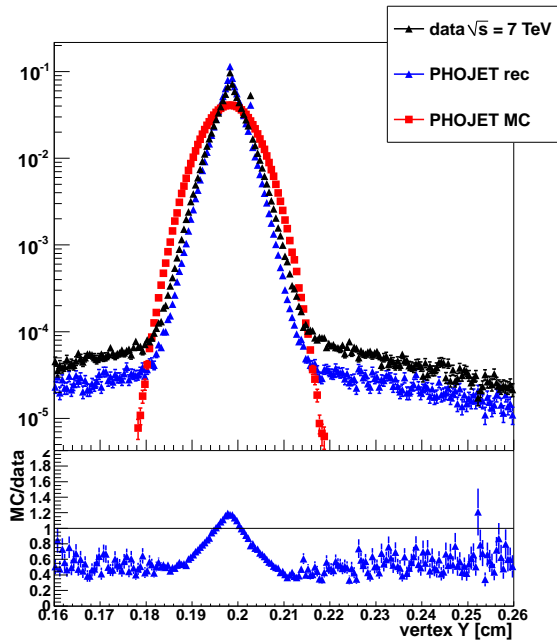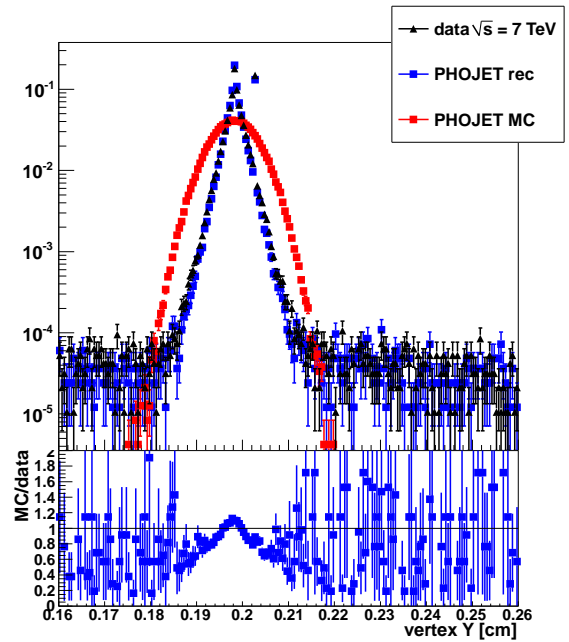
(a) Events selected by cint1b trigger.
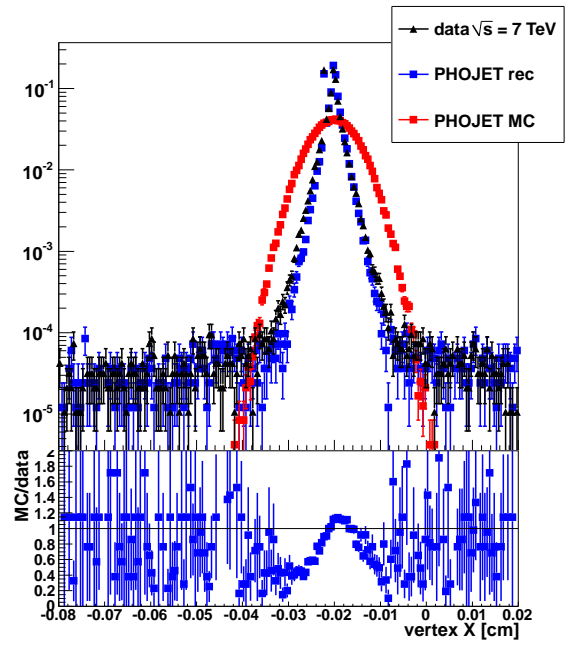
(b) Events selected by the MBV0diff trigger.

Figure 6.11: Comparison of *x* positions of vertices for the generated PHOJET MC, reconstructed MC and data. The bottom panel shows the ratio of reconstructed MC and data.


(a) Events selected by cint1b trigger.

(b) Events selected by the MBV0diff trigger.

Figure 6.12: Comparison of *y* positions of vertices for the generated PHOJET MC, reconstructed MC and data. The bottom panel shows the ratio of reconstructed MC and data.

6.4.3 Track-to-vertex cuts

Finally, the DCA cuts on the tracks in data and MC are compared. Figures 6.15(a) and 6.15(b) show the DCA in the *xy* position of tracks to the primary vertex in events that satisfy the cint1b and MBV0diff trigger conditions respectively.

Figure 6.16 shows the DCA *xy* plotted against the track p_T for data, PYTHIA 6, PYTHIA 8 and PHOJET satisfying the MBV0diff trigger condition. The curve on the plots shows the p_T dependent cut on DCA-*xy* corresponding to a 7 σ cut at a given p_T. The distributions in these plots are produced without the DCAXY-to-vertex cut to show the number of tracks that lie above the cut. It is clear that the standard DCAXY cut does not exclude many events and the effect on the absolute normalisation is negligible.

The last variable to compare is the *z* position of the DCA of the track to the vertex. The standard value of this cut is at 2 cm. Figures 6.17(a) and 6.17(b) show the *z* component of the DCA of tracks to the primary vertex in events that satisfy the cint1b and MBV0diff trigger conditions respectively. The cut affects less than 1 in a thousand events and so has a negligible effect on the p_T, η and multiplicity distributions of the sample.

6.4.4 Final systematic uncertainty estimates

To combine the systematic uncertainties arising from varying different cuts, the correlations between the variables are studied. This is achieved by applying a cut on one variable and studying its effect on another. For example, the DCA distributions might depend on the position of the primary vertex and track cuts. Figures 6.18 to 6.20 examine the correlation between the DCA-*xy* and *NclustersTPC*, *MaxChi2PerClusterTPC* and the vertex respectively, for events satisfying the cint1b and MBV0diff triggers. Similarly, figures 6.21 to 6.23 examine these correlations for the DCA-*z*. These correlations are studied using the PHOJET MC model.
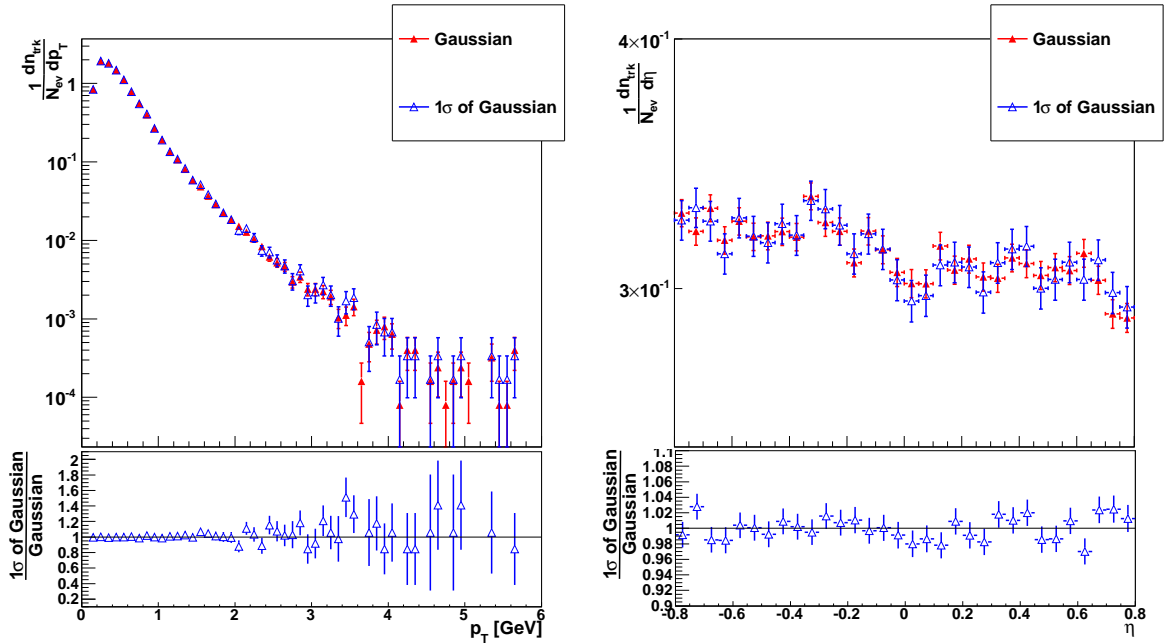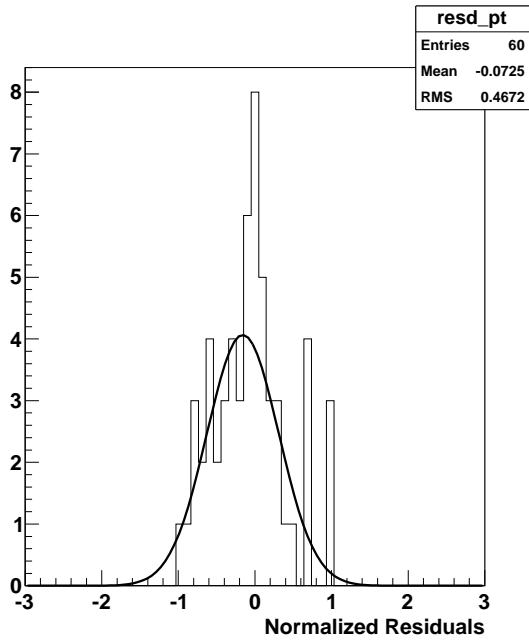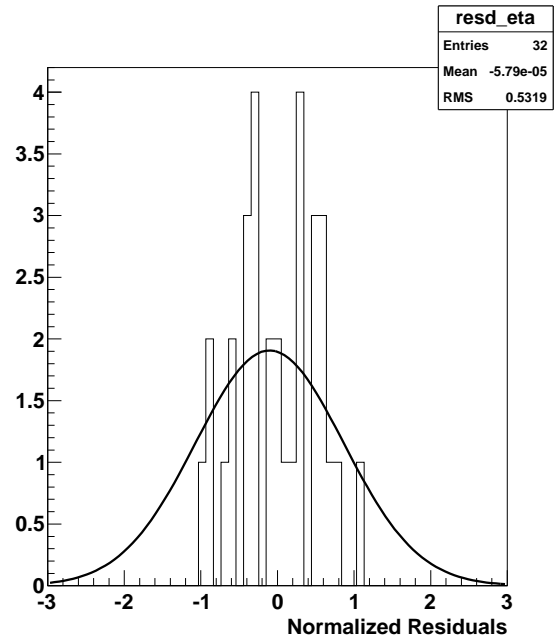
(a) p_T distribution.
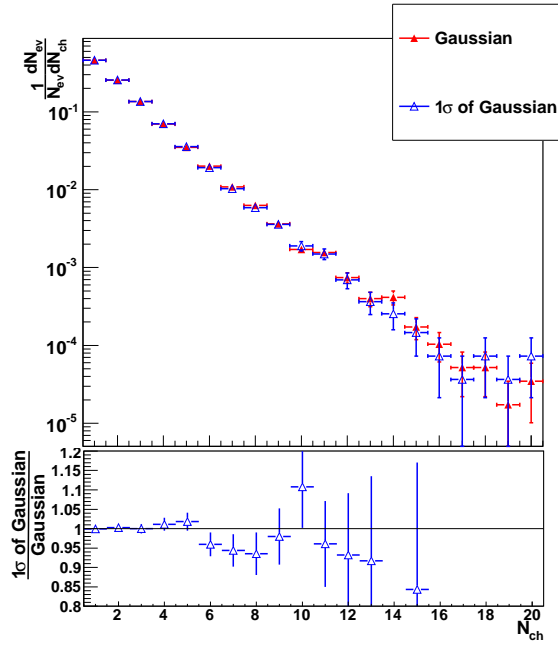
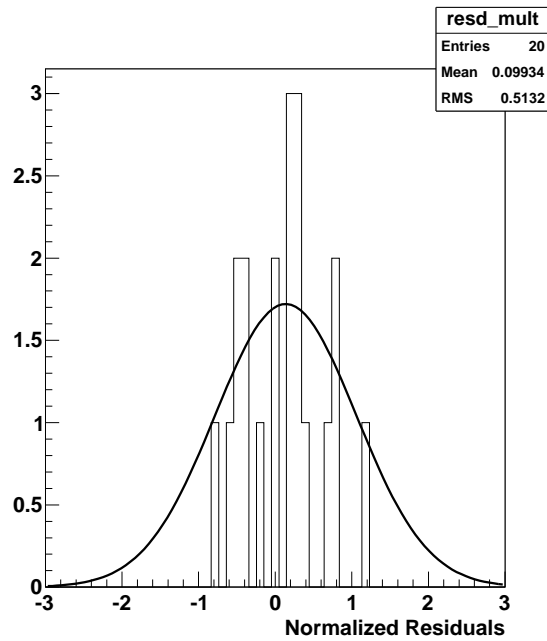(b) η distribution.

(c) N_{ch} distribution.

Figure 6.13: Distributions of p_T, η and N_{ch} for PHOJET events comparing a full Gaussian vertex with a cut at 1σ on the generated vertex in MC. The bottom panel shows the ratio of 1σ of the Gaussian vertex and the full Gaussian vertex. All distributions are normalised to the number of events.

(a) p_T distribution.

(b) η distribution.

(c) N_{ch} distribution.

Figure 6.14: Residuals in p_T, η and multiplicity distributions comparing PHOJET at a 1σ cut on the generated vertex with no such cut.

(a) Events selected by cint1b trigger.

(b) Events selected by the MBV0diff trigger.
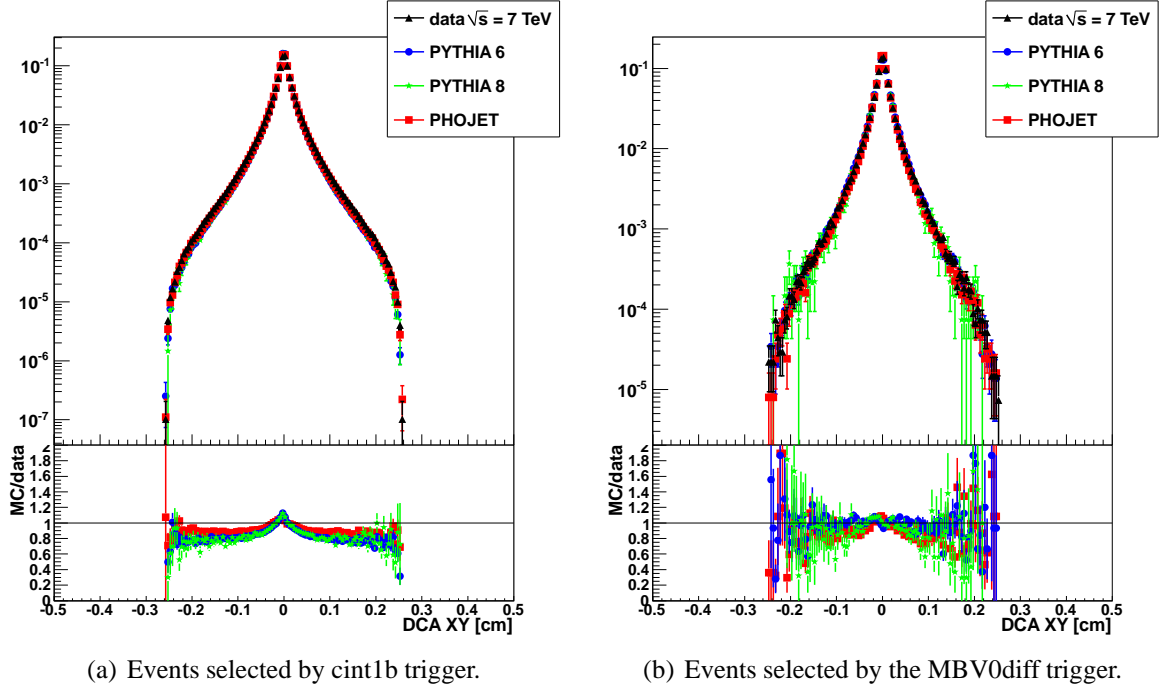
Figure 6.15: Distributions of the DCA-*xy* of tracks to the primary vertex. The bottom panel shows the ratio of MC and data.

The correlation studies show that there is negligible correlation between the DCA and the variables used to estimate systematic uncertainties. Hence, the uncertainties from various sources are added linearly to get a conservative estimate. Table 6.5 shows the systematic uncertainty on the p_T, multiplicity and η distributions. Also included is the VZERO detector efficiency [5] and uncertainty from background estimated using the control triggers described in section 6.2. Additionally, no systematics in the shape of p_T, η and multiplicity is observed from the sources of systematic uncertainty studied. In the ALICE publication [5], additional sources of systematic uncertainties arising from material budget, alignment, SPD efficiency and tracking efficiency are considered.

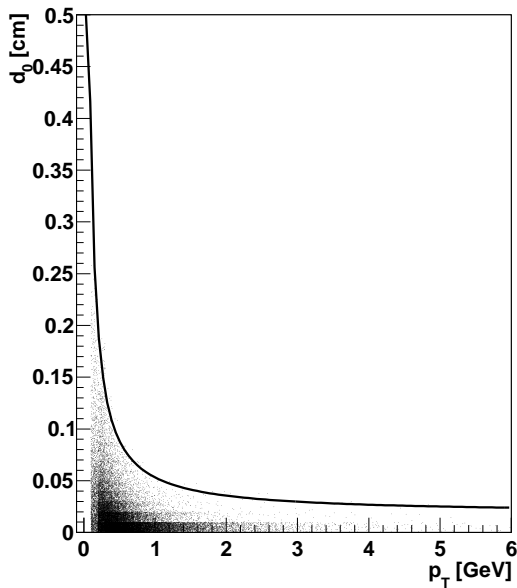## 6.5 Kinematic distributions - comparison of data with MC

Figures 6.24, 6.25 and 6.26 show the p_T, η and multiplicity distributions in data compared with all three MC models - PYTHIA 6, PYTHIA 8 and PHOJET. The bottom plot in each shows the ratio of MC to data. The total systematic uncertainty is less than 2.1% (when individual contributions
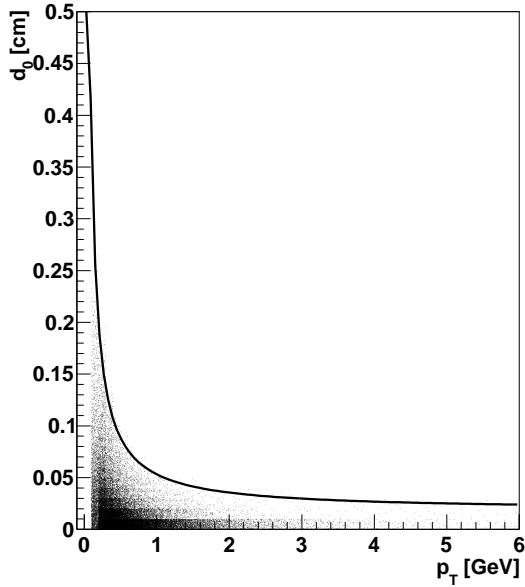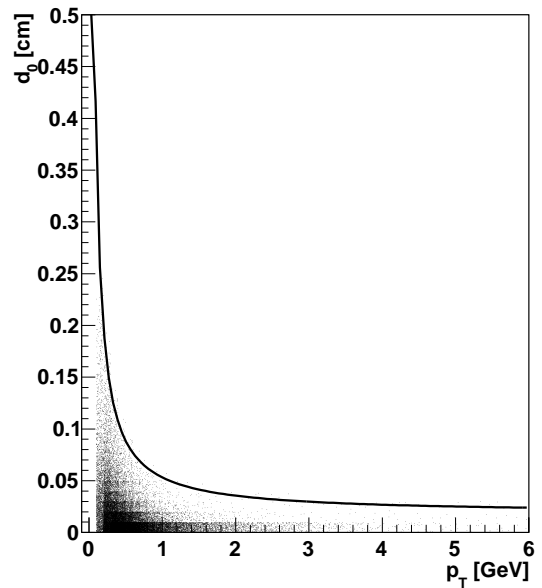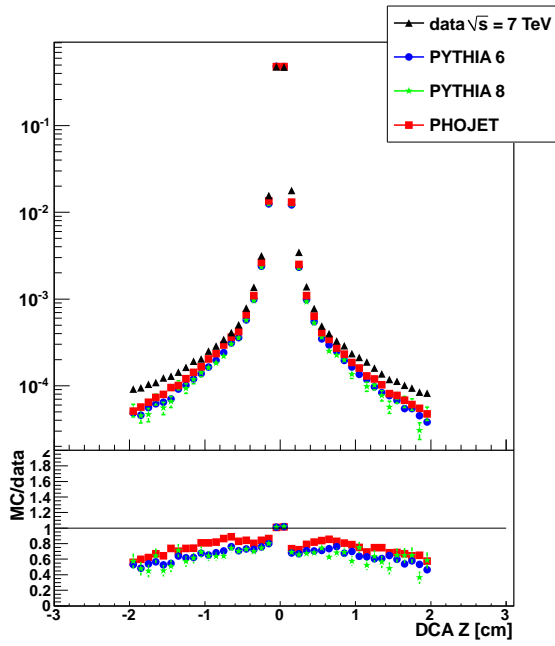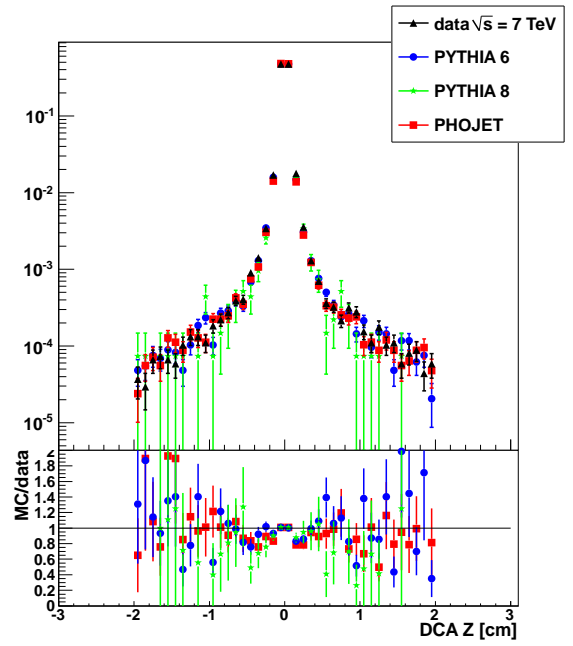
(a) Data.
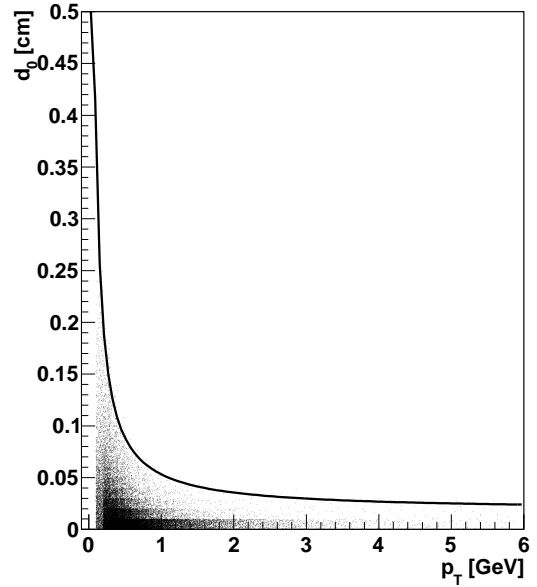
(b) PYTHIA 6.

(c) PYTHIA 8.

(d) PHOJET.

Figure 6.16: Distributions of the DCA-*xy* of tracks to the primary vertex versus the track p_T for events satisfying the MBV0diff trigger.
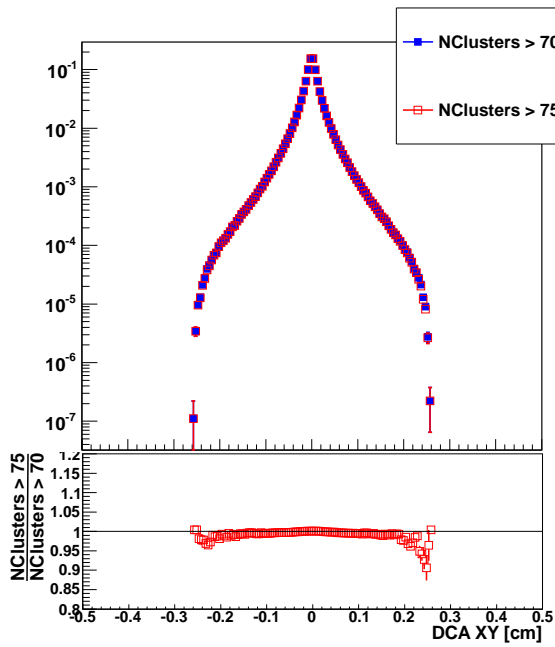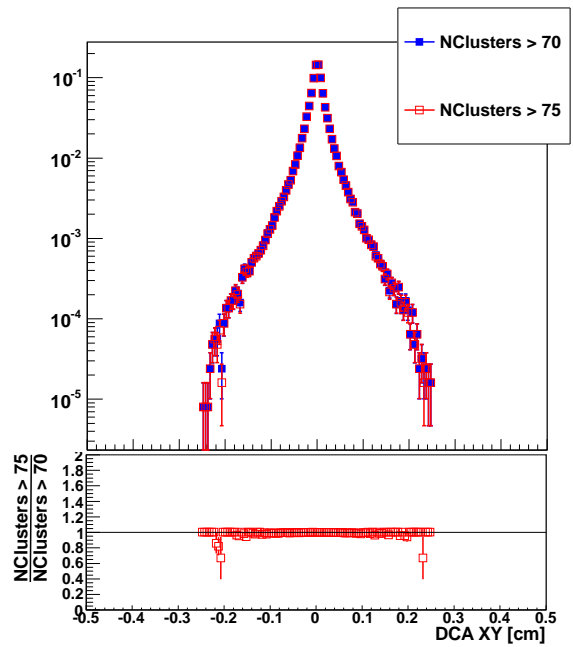
(a) Events selected by cint1b trigger.

(b) Events selected by the MBV0diff trigger.

Figure 6.17: Distributions of the DCA-z of tracks to the primary vertex. The bottom panel shows the ratio of MC and data.
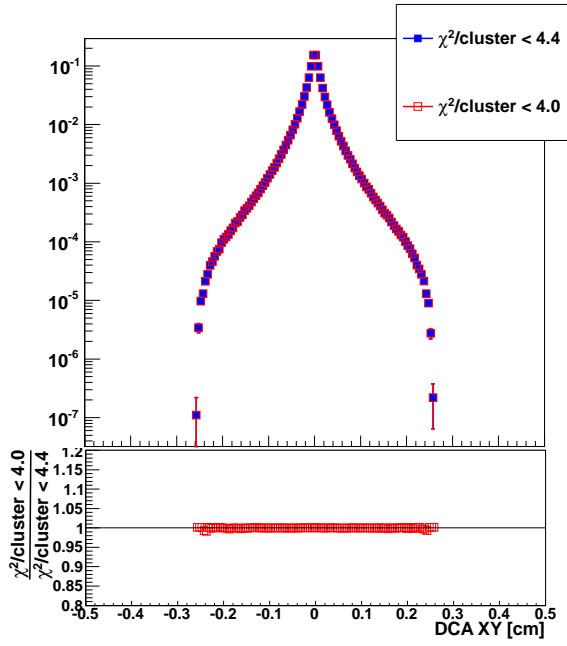

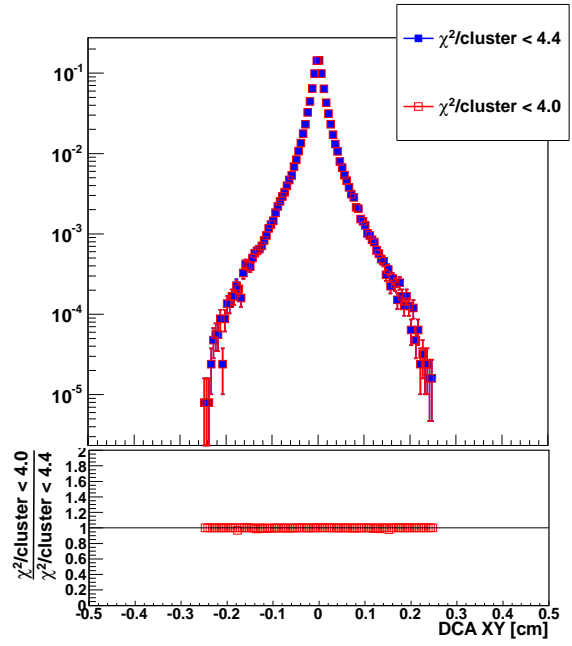(a) Events selected by cint1b trigger.

(b) Events selected by the MBV0diff trigger.

Figure 6.18: The correlation between DCA-xy and the *NClustersTPC* cut. The bottom panel shows the ratio of the DCA-xy for the two cuts in the minimum number of TPC clusters.

(a) Events selected by cint1b trigger.

(b) Events selected by the MBV0diff trigger.

Figure 6.19: The correlation between DCA-*xy* and the *MaxChi2PerClusterTPC* cut. The bottom panel shows the ratio of the DCA-*xy* for the two cuts in the maximum χ^2 per TPC cluster.

(a) Events selected by cint1b trigger.

(b) Events selected by the MBV0diff trigger.

Figure 6.20: The correlation between DCA-*xy* and the vertex distribution. The bottom panel shows the ratio of the DCA-*xy* for the full Gaussian vertex and 1σ of the Gaussian vertex.

111

(a) Events selected by cint1b trigger.

(b) Events selected by the MBV0diff trigger.

Figure 6.21: The correlation between DCA-z and the *NClustersTPC* cut. The bottom panel shows the ratio of the DCA-z for the two cuts in the minimum number of TPC clusters.
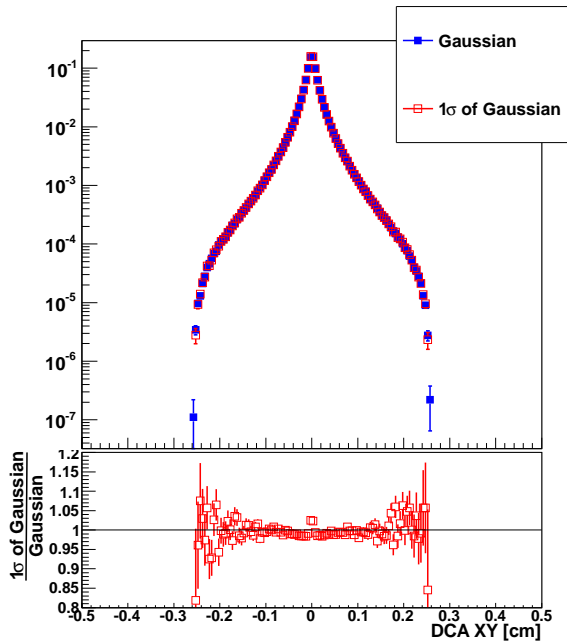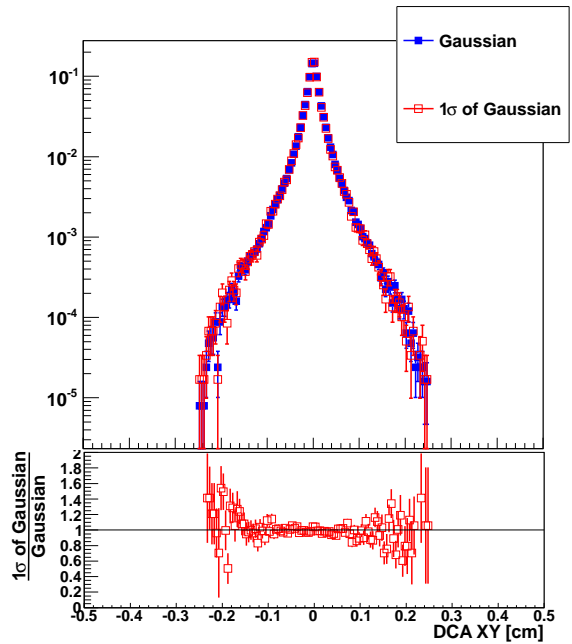

(a) Events selected by cint1b trigger.
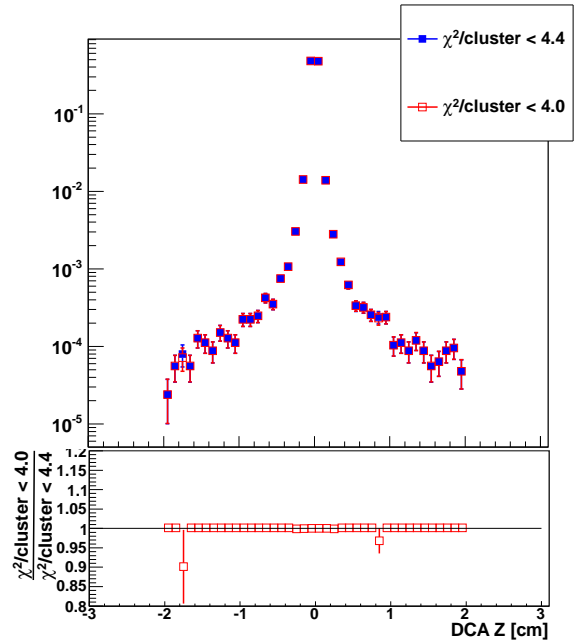
(b) Events selected by the MBV0diff trigger.

Figure 6.22: The correlation between DCA-z and the *MaxChi2PerClusterTPC* cut. The bottom panel shows the ratio of the DCA-z for the two cuts in the maximum χ^2 per TPC cluster.
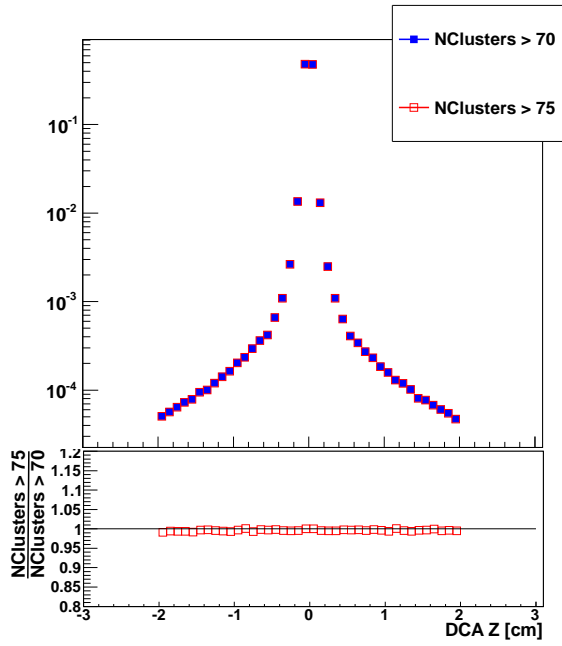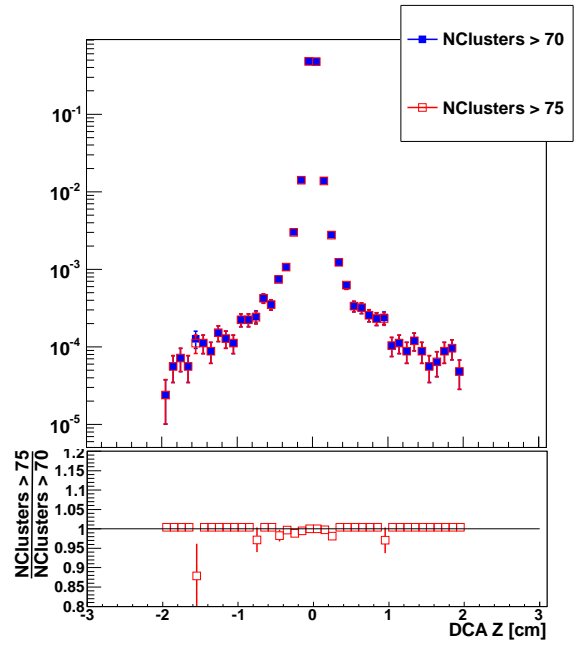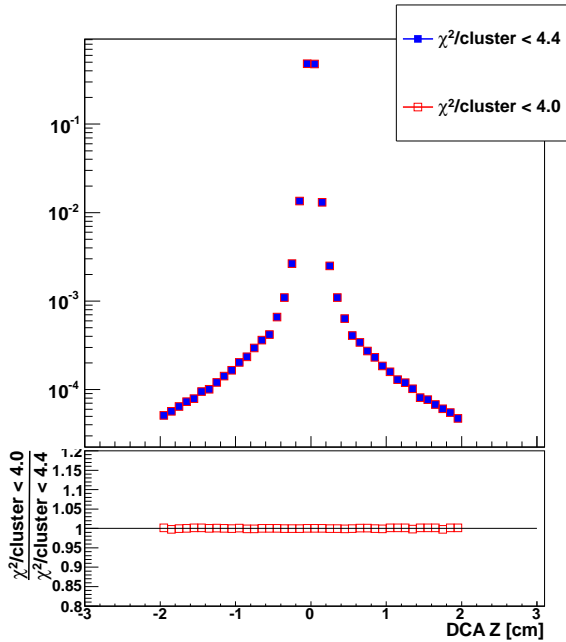
(a) Events selected by cint1b trigger.

(b) Events selected by the MBV0diff trigger.
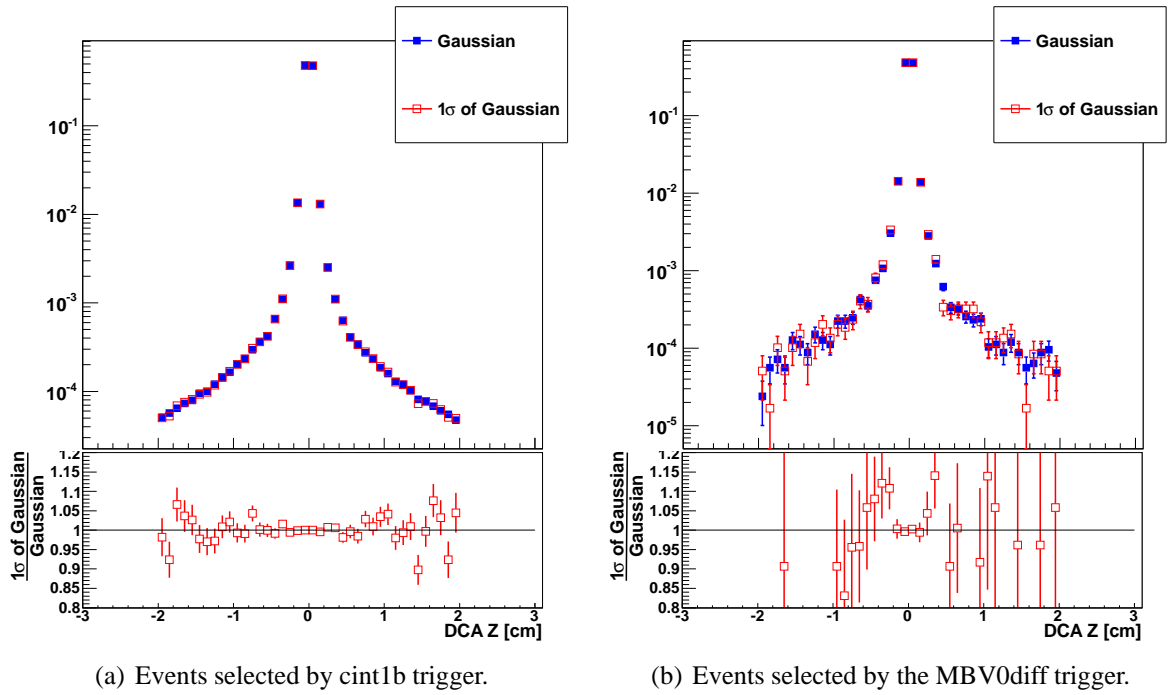
Figure 6.23: The correlation between DCA-z and the vertex distribution. The bottom panel shows the ratio of the DCA-z for the full Gaussian vertex and 1σ of the Gaussian vertex.

Table 6.5: Contributions to systematic uncertainties from various sources in p_T, η and multiplicity distributions. The total error is the linear sum of the individual contributions.

Source	Systematic uncertainty
background	0.1%
V0 detector efficiency	1.5%
track selection cuts	$< 0.5\%$
vertex position	negl.
track-to-vertex cuts	negl.
Total	$< 2.1\%$

are added linearly) and the statistical errors are shown as error bars on each point. All three fig-ures show that PYTHIA 8 and PHOJET describe data better than PYTHIA 6. This is because of a missing hard component of diffraction in PYTHIA 6. In order to obtain a quantitative comparison of the three models with data, the χ^2/NDF (number of degrees of freedom) of a two dimensional histogram of the p_T and multiplicity distributions, integrated over η, in data and each of the MC models are compared. Table 6.6 shows the χ^2/NDF for the comparison of data with PYTHIA 6, PYTHIA 8 and PHOJET. The χ^2/NDF values clearly indicate that none of the models describe data well; PYTHIA 6 is significantly the worst. The residuals (see equation (C8) in appendix C) for PHOJET, PYTHIA 6 and PYTHIA 8 are shown in figures 6.27 to 6.29. On the x-axis is multi-plicity in 20 bins and on the y-axis is p_T in 60 bins. Pseudorapidity has been integrated over. The colour scale indicates the value of the residual for each p_T and multiplicity bin. In all models, it is seen that the largest residuals are at low p_T, indicating that all models are bad at low p_T. PYTHIA 6 clearly underestimates data at low p_T up to a multiplicity of around 10, while in PHOJET the largest discrepancy with data is at mid-multiplicity (5-15). In this range of multiplicity, PHOJET over-estimates data. While none of the models describes data perfectly, PYTHIA 8 and PHOJET do a qualitatively better job.

Table 6.6: The χ^2/NDF for the comparison of data with MC models. The NDFs for the different generators are not the same for the various models as empty bins are excluded from the comparison.

MC model	χ^2/NDF
PYTHIA 6	12644.5/182 = 69.5
PHOJET	1357.0/176 = 7.7
PYTHIA 8	924/158 = 5.8

6.6   Summary

In this chapter, a data sample enhanced in SD events was selected using the MBV0diff offline trigger. The efficiency of this trigger varies between 3% and 4.3% depending on the MC genera-tor used to estimate efficiencies. The fraction of cint1b events that satisfy the MBV0diff trigger condition in data is 3.5%. The data were compared with PYTHIA 6, PYTHIA 8 and PHOJET
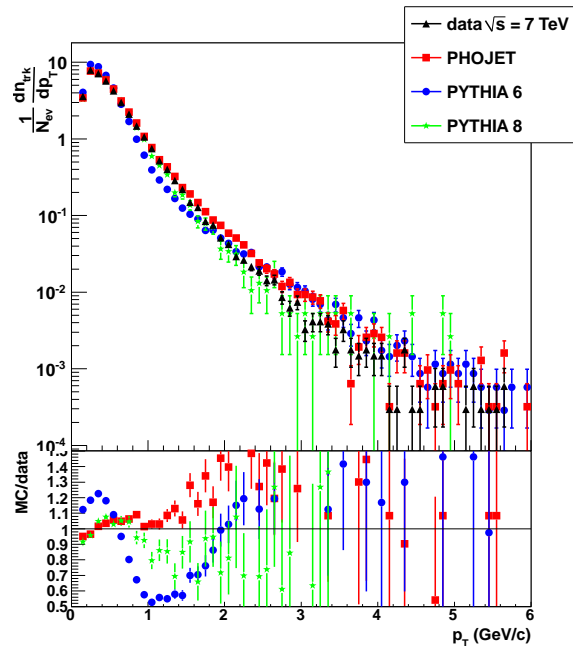
Figure 6.24: p_T distributions for data and MC models, and the ratio of MC/data. The total systematic error is less than 2.1% and the error bars give the statistical errors.
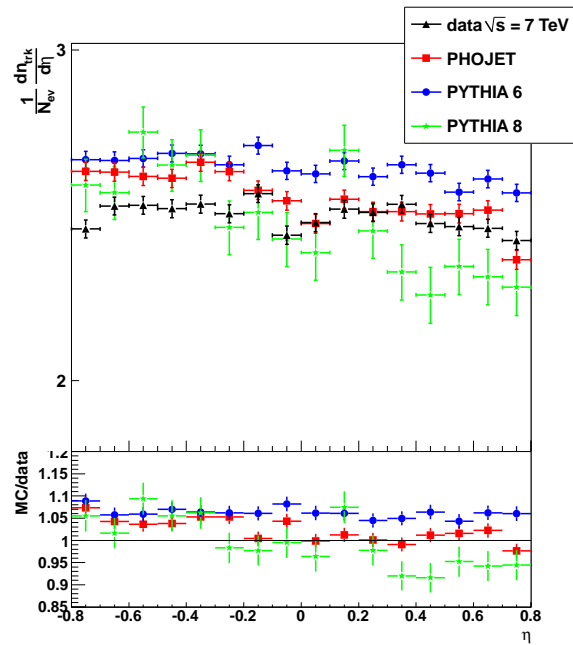
Figure 6.25: η distributions for data and MC models, and the ratio of MC/data. The total systematic error is less than 2.1% and the error bars give the statistical errors.
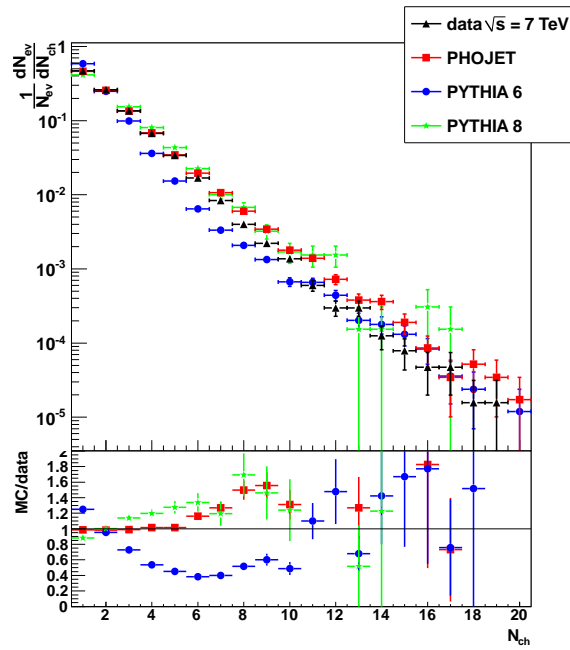
Figure 6.26: Multiplicity distributions for data and MC models, and the ratio of MC/data. The total systematic error is less than 2.1% and the error bars give the statistical errors.
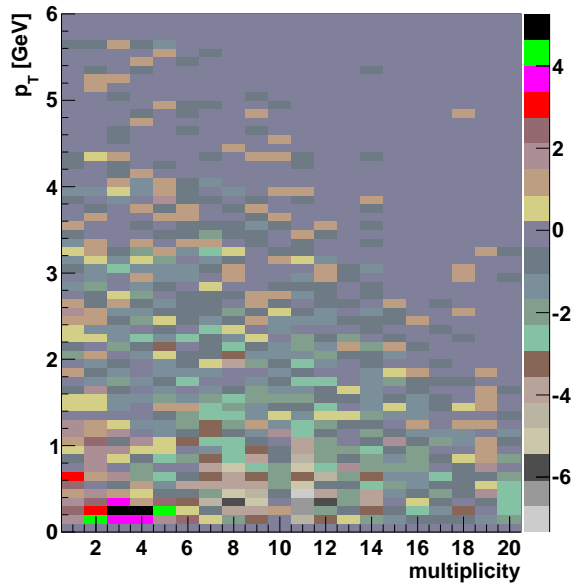
Figure 6.27: Normalised residuals of p_T and multiplicity comparing PHOJET with data. η is integrated over 1.6 units of pseudorapidity.

116
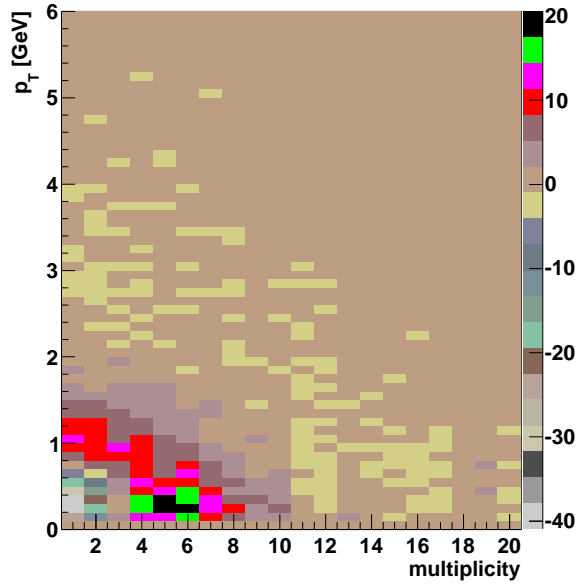
Figure 6.28: Normalised residuals of p_T and multiplicity comparing PYTHIA 6 with data. η is integrated over 1.6 units of pseudorapidity.
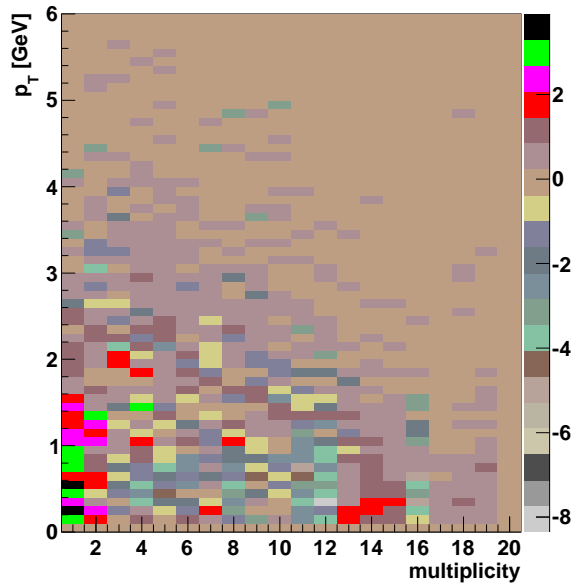
Figure 6.29: Normalised residuals of p_T and multiplicity comparing PYTHIA 8 with data. η is integrated over 1.6 units of pseudorapidity.

MC models in p_T, η and multiplicity distributions.

The total systematic error due to beam induced background, detector efficiency and track selection cuts is estimated to be $< 2.1\%$.

None of the models describe data perfectly. PYTHIA 8 and PHOJET describe data equally well and significantly better than PYTHIA 6. The inclusion of hard diffraction in PYTHIA 8 improves the agreement with data. At high p_T and multiplicities in the selected MBV0diff samples, hard diffraction and the non-diffractive components are dominant.

ATLAS has performed a similar study [81], also presented in [82]. The results presented here are not directly comparable with ATLAS because of the different η ranges of the detectors and the difference in the minimum p_T cut-off. ATLAS has a higher p_T cut-off than ALICE. However, the qualitative trends of differences between data and MC models in the two studies are similar.

CHAPTER 7

Summary

ALICE at the LHC is designed to measure properties of strongly interacting matter created in heavy-ion collisions. However, its design, and in particular, its low p_T acceptance in the central barrel enables ALICE to play an important role in understanding pp collisions. The analyses presented in this thesis are based on early pp data collected at a centre-of-mass energy of 7 TeV and the Monte Carlo event generators PYTHIA 6, PHOJET and PYTHIA 8.

Multiplicity, pseudorapidity density and transverse momentum distributions of data are among the first measurements made at a new energy regime. They are taken with a minimum bias trigger. Other selection criteria based on trigger signals can be used to select rare events in the MB sample. Triggers are subject to an efficiency, which gives the fraction of events of a particular process type that are selected by that trigger. Since trigger efficiencies are model dependent, the results from two different event generators, PYTHIA 6 and PHOJET are compared. PYTHIA 6 and PHOJET differ not only in the fraction of diffractive events they predict, but also in their kinematic distributions. At a given energy PHOJET efficiencies are higher than those for PYTHIA 6, because PHOJET has a hard diffractive component, while PYTHIA 6 does not. For results published on charged particle multiplicity at 900 GeV and 2.36 TeV, measured fractions of single and double diffraction were taken from previous experiments and used along with the kinematics from both PYTHIA 6 and PHOJET to get an estimate of the efficiencies of the triggers used to select non-single diffractive events and inelastic events. These efficiencies were used for correcting data in the first ALICE publications on multiplicity. The systematic uncertainty of this measurement due to kinematics and the relative fractions of diffractive events are calculated and have been used as

a cross-check in ALICE's initial physics publications.

PYTHIA 8.130 is the first version of PYTHIA to include a description of hard diffraction. In this model, a Pomeron is emitted from one of the protons in a pp collision via a soft interaction. The proton transfers a fraction of its momentum to the Pomeron before it is deflected. The Pomeron then interacts with the other proton via a hard interaction. The implementation of this model in PYTHIA 8 has a few tunable parameters. The effect of changing these parameters on the average multiplicity at a given center-of-mass energy is presented. A comparison of multiplicity, pseudo-rapidity density and transverse momentum distributions in PYTHIA 6, PYTHIA 8 and PHOJET is also presented.

Finally, a data sample enriched in single diffractive events was selected. These data were compared with PYTHIA 6, PHOJET and PYTHIA 8 models in multiplicity, pseudorapidity density and transverse momentum distributions. While none of the models describes data perfectly, PYTHIA 8 and PHOJET describe data equally well and better than PYTHIA 6.
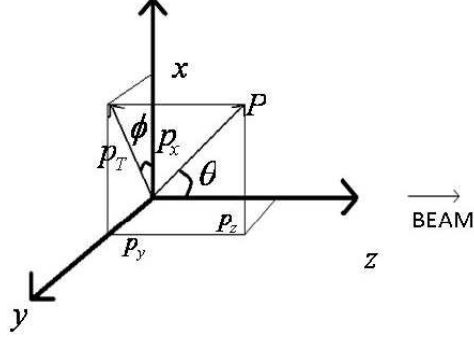
Appendix

A Collision Kinematics

Figure A1: Axes showing the definition of various angles and the beam direction.

In figure A1 the beam is along the z-axis in the positive z direction. θ is the angle made by the momentum of the particle $\mathbf{p}$ ($|\mathbf{p}| = \sqrt{p_x^2 + p_y^2 + p_z^2}$) with the beam axis, where p_x, p_y and p_z are the x, y and z components of the particle's momentum respectively. ϕ is the azimuthal angle between the transverse momentum ($\mathbf{p_T}$) of the particle and the positive x direction where $|\mathbf{p_T}| = p_T = \sqrt{p_x^2 + p_y^2}$.

A useful variable commonly used to describe the kinematic condition of a particle is its rapidity. For a particle of energy E, the rapidity y is defined as

$$y = \frac{1}{2} \ln \frac{E + p_z}{E - p_z}. \tag{A1}$$

Rapidity is a dimensionless quantity which can be positive or negative. In the non-relativistic limit ($E \simeq m$, where m is the mass of the particle), the rapidity of a particle travelling along the beam reduces to the velocity (v) of the particle. What makes rapidity a useful variable is the fact that it transforms additively under a Lorentz boost along z giving

$$y \xrightarrow[\text{boost}]{} y' + \frac{1}{2} \ln \frac{1 + v}{1 - v}. \tag{A2}$$

So rapidity differences (and hence, the shape of the rapidity distribution) are invariant under lon-

I

gitudinal boosts and remain the same in all collinear frames.

To characterise the rapidity of a particle, we need to measure its E and p_z. In many experiments it is only possible to measure the angle θ. The pseudorapidity of a particle is defined as

$$\eta = -\ln\tan\frac{\theta}{2}. \tag{A3}$$

In terms of its momentum the pseudorapidity of a particle can be written as

$$\eta = \frac{1}{2}\ln\frac{|\mathbf{p}|+p_z}{|\mathbf{p}|-p_z}. \tag{A4}$$

Comparing equations A1 and A4, in the relativistic limit ($E \simeq |\mathbf{p}|$) the pseudorapidity and rapidity of a particle are equal.

More generally, the rapidity and pseudorapidity of a particle are related by the Jacobian in equation (A5). The derivation is provided in appendix B.

$$\frac{dy}{d\eta} = \frac{p_T\cosh\eta}{\sqrt{m^2+p_T^2\cosh^2\eta}} \tag{A5}$$

II

B Derivation of the Jacobian to convert from η to y

Rapidity (y) is a function of energy (E) and the longitudinal momentum (p_z), and pseudorapidity (η) is a function of the polar angle θ. To change from the momentum coordinates $y = f(E, p_z)$ to $\eta = f(\theta)$, we need to map the area dy to $d\eta$. This is done by the Jacobian matrix.

We start off by defining the transverse mass of a particle as

$$m_T^2 = m^2 + p_T^2. \tag{B1}$$

Using equation (B1) along with equation (A1) and multiplying the fraction by $\sqrt{E + p_z}$, we get

$$m_T e^y = E + p_z. \tag{B2}$$

Similarly, by multiplying the fraction by $\sqrt{E - p_z}$, we get

$$m_T e^{-y} = E - p_z. \tag{B3}$$

Subtracting equation (B3) from equation (B2), we get equation (B4).

$$p_z = m_T \sinh y \tag{B4}$$

From figure A1,

$$\tan \theta = \frac{p_T}{p_z} \qquad \text{or} \qquad p_z = p_T \frac{\cos \theta}{\sin \theta} = \frac{p_T}{\tan \theta}. \tag{B5}$$

The following two equations are standard trigonometric equations.

$$\tan \theta = \frac{2 \tan \frac{\theta}{2}}{1 - \tan^2 \frac{\theta}{2}} \tag{B6}$$

$$\sinh x = \frac{e^x - e^{-x}}{2} \tag{B7}$$

Equating for p_z in B4 and B5, and using equations B6, B7 and A3, we can show that

III

$$m_T \sinh y = p_T \sinh \eta. \tag{B8}$$

Differentiating equation (B8) with respect to η gives

$$m_T \frac{dy}{d\eta} \cosh y = p_T \cosh \eta \qquad \text{or}$$

$$\frac{dy}{d\eta} = \frac{p_T \cosh \eta}{m_T \cosh y}. \tag{B9}$$

Using equation (B9) and the equation

$$\cosh^2 x - \sinh^2 x = 1$$

leads to equation (A5) which is

$$\frac{dy}{d\eta} = \frac{p_T \cosh \eta}{\sqrt{m^2 + p_T^2 \cosh^2 \eta}},$$

the Jacobian.

C χ^2 test for comparing two unweighted histograms

This section reiterates a part of the method Chi2Test, described and implemented in the TH1 class in ROOT [30]. Below is a description of the comparison of two unweighted histograms based on Pearson's test [83] described in [84].

In the case of two histograms with the same binning and the number of bins in each equal to r, the total number of entries in histograms 1 and 2 are given by

$$N = \sum_{i=1}^{r} n_i \tag{C1}$$

and

$$M = \sum_{i=1}^{r} m_i, \tag{C2}$$

where n_i and m_i are the number of entries in the ith bin in histograms 1 and 2 respectively.

According to [85] two histograms are homogeneous if they represent random values with identical distributions. Mathematically, this is equivalent to the existence of r constants $p_1, ..., p_r$, where p_i is the probability of a measured value in both experiments belonging to the ith bin, such that

$$\sum_{i=1}^{r} p_i = 1. \tag{C3}$$

The number of entries in the ith bin is a random variable with a distribution approximated by a Poissonian probability distribution with

$$\frac{e^{-Np_i}(Np_i)^{n_i}}{n_i!} \tag{C4}$$

and

$$\frac{e^{-Mp_i}(Mp_i)^{m_i}}{m_i!} \tag{C5}$$

for the first and second histograms respectively. For homogeneous histograms, the maximum

likelihood estimator $\hat{p}_i$ for each p_i with $i = 1,...,r$ is given by

$$\hat{p}_i = \frac{n_i + m_i}{N + M} \tag{C6}$$

and

$$X^2 = \sum_{i=1}^{r} \frac{(n_i - N\hat{p}_i)^2}{N\hat{p}_i} + \sum_{i=1}^{r} \frac{(m_i - M\hat{p}_i)^2}{M\hat{p}_i} = \frac{1}{MN} \sum_{i=1}^{r} \frac{(Mn_i - Nm_i)^2}{n_i + m_i} \tag{C7}$$

has approximately a $\chi^2_{(r-1)}$ distribution [85]. The difference between the bin content and expected bin content is called a residual. A comparison of normalised residuals, as explained below, helps in identifying bins of histograms responsible for a significant overall χ^2 value [86]. In homogeneous histograms, normalised residuals are independent and identically distributed random variables that are normally distributed with a mean of zero and a variance of 1. The normalised residuals in the first and second histograms are given by

$$r_i = \frac{n_i - N\hat{p}_i}{\sqrt{N\hat{p}_i}\sqrt{\left(\frac{1-N}{N+M}\right)\left(1 - \frac{n_i + m_i}{N+M}\right)}} \tag{C8}$$

and

$$r_i' = \frac{m_i - M\hat{p}_i}{\sqrt{M\hat{p}_i}\sqrt{\left(\frac{1-M}{N+M}\right)\left(1 - \frac{n_i + m_i}{N+M}\right)}} \tag{C9}$$

respectively. It is interesting to note that $r_i = -r_i'$, so either residual can be used.

The application of the test has restrictions on the value of the expected frequencies Np_i and Mp_i for $i = 1,...,r$. According to [87] a conservative rule states that all expectations for both histograms must be greater than or equal to one. However, in most cases the χ^2 test may be used when expectations in the smallest bins of the histograms is greater than 0.5. For unknown expected frequencies Np_i and Mp_i, the estimated expected frequencies $N\hat{p}_i$ and $M\hat{p}_i$ for $i = 1,...,r$ can be used.

Bibliography

[1] L. Evans, P. Bryant, *LHC Machine*, JINST **3** S08001 (2008).

[2] ALICE Collaboration, *The ALICE experiment at the CERN LHC*, JINST **3** S08002 (2008).

[3] P. Giubellino *et al.*, ALICE Internal Note 2000-28;
J.-P. Revol, *Low-p_T Proton-Proton Physics at Low Luminosity.*, ALICE-PUB-2002-02, Oct 2001.

[4] K. Aamodt *et al.* [ALICE Collaboration], Eur. Phys. J. C **65** (2010) 111-125.

[5] K. Aamodt *et al.* [ALICE Collaboration], Eur. Phys. J. C **68** (2010) 89-108.

[6] K. Aamodt *et al.* [ALICE Collaboration], Eur. Phys. J. C **68** (2010) 345-354.

[7] K. Aamodt *et al.* [ALICE Collaboration], Phys. Lett. B **693** (2010) 53-68;

[8] K. Aamodt *et al.* [ALICE Collaboration], *Production of pions, kaons and protons in pp collisions at $\sqrt{s} = 900\,GeV$ with ALICE at the LHC*, arXiv:1101.4110 [hep-ex] 9 May 2011.

[9] K. Aamodt *et al.* [ALICE Collaboration], Eur. Phys. J. C **71** (2011) 1594.

[10] F. Carminati *et al.*, *ALICE:Physics Performance Report, Volume I*, J. Phys. G: Nucl. Part. Phys. **30** (2004) 1517-1763.

[11] T. Sjöstrand, S. Mrenna and P. Skands, JHEP**05** (2006) 026.

[12] R. Engel, *PHOJET manual (program version 1.05, June 96)*, University Siegen preprint 95-05.

[13] A. Breakstone *et al.*, Phys. Rev. **D 30** (1984) 528.

[14] V. Khachatryan *et al.* [CMS collaboration], J. High Energy Phys. **2010** 02041 (2010).

[15] G. J. Alner *et al.* [UA5 collaboration], Phys. Lett. **B 167** (1986) 476.

[16] C. Albajar *et al.* [UA1 collaboration], Nucl. Phys. **B 335** (1990) 261.

[17] R. Noucier *et al.* [PHOBOS collaboration], J. Phys. G **30** S1133 (2004).

[18] F. Abe *et al.* [CDF collaboration], Phys. Rev. **D 41** (1990) 2330.

[19] B. I. Abelev *et al.* [STAR collaboration], Phys. Rev. **C 79** (2009) 034909.

[20] B. Adeva *et al.* [L3 Collaboration], Nucl. Inst. Meth. **A 289** (1990) p241.

[21] ALICE Collaboration, *ALICE TDR 010*, CERN-LHCC-2003-062, 7 January 2004; ALICE Collaboration, *ALICE - Technical Design Reports*, `http://alice.web.cern.ch/Alice/TDR`.

[22] ATLAS Collaboration, *The ATLAS Experiment at the CERN Large Hadron Collider*, JINST 3 S08003 (2008).

[23] CMS Collaboration, *The CMS experiment at the CERN LHC*, JINST 3 S08004 (2008).

[24] LHCb Collaboration, *The LHCb Detector at the LHC*, JINST 3 S08005 (2008).

[25] LHCf Collaboration, *Technical Proposal for the CERN LHCf Experiment*, CERN/LHCC 2005-032 (2005).

[26] TOTEM Collaboration, *TOTEM Technical Proposal*, CERN/LHCC 99-7 (1999).

[27] J. F. Grosse-Oetringhaus, *Proton-Proton Physics with ALICE*, arXiv:0808.2935v1 [hep-ex] 21 Aug 2008.

[28] J. Conrad, J. G. Contreras and C. Jørgensen, ALICE-INT-2005-025 (2005) 5.

[29] *The ALICE experiment offline project*, `http://aliweb.cern.ch/Offline`; *The ALICE Offline Bible*; *ALICE Technical Design Report of the Computing*, CERN-LHCC-2005-018, ALICE TDR 012 (2005).

[30] *An object oriented data analysis framework*, `http://root.cern.ch`.

[31] S. Bagnasco *et al.*, J. Phys.: Conf. Ser. 119 062012 (2008).

[32] *Worldwide LHC Computing Grid*, `http://lcg.web.cern.ch/lcg/`.

[33] P. Billoir, *Progressive track recognition with a Kalman like filter procedure*, Comput. Phys. Commun. **57** (1989) 390.

[34] D. H. Perkins, *Introduction to High Energy Physics*, CUP, fourth edition (2000) p 7,171.

[35] S. Bethke, Prog. in Part. and Nucl. Phys. **58** Issue 2 (2007) 351-386, doi:10.1016/j.ppnp.2006.06.001.

[36] V. Barone, E. Predazzi, *High-Energy Particle Diffraction*, Springer-Verlag Berlin Heidelberg New York (2002) p 1-6,47.

[37] A. Aktas *et al.* [H1 Collaboration], Eur. Phys. J. **C48** (2006) 715 [hep-ex/0606004].

[38] P. D. Collins, *An Introduction to Regge Theory And High-Energy Physics*, CUP (1977).

[39] C-Y. Wong, *Introduction to high-energy heavy-ion collisions*, World Scientific Publishing (1994) pp.132-154.

[40] M. J. Menon, Braz. Jour. of Phys. **35** number 1 (2005) 100-121.

[41] V. N. Gribov, Soviet Phys. JETP **14** (1961) 478 and 1395;
G. F. Chew and S. Frautschi, Phys. Rev. Lett. **7** (1961) 394.

[42] R. M. Godbole, *et al.*, arXiv:1001.4749 [hep-ph] January 2010.

[43] I. Y. Pomeranchuk, Sov. Phys. JETP, **3** (1961) 307.

[44] J. R. Forshaw, D. A. Ross, *Quantum Chromodynamics and the Pomeron*, CUP (1997), p17.

[45] Z. Li-Juan *et al.*, Commun. Theor. Phys. **45** (2006) 1069;
H. Zhao-Hui *et al.* Commun. Theor. Phys. **49** (2008) 729.

[46] M. Deile, *Open issues in diffractive physics: What answers do we expect from the LHC?*, Talk given at Physics at the LHC 2008 in Split, Croatia on 2nd October, 2008, `http://indico.cern.ch/materialDisplay.py?contribId=58&sessionId=14&materialId=slides&confId=17686`.

[47] N. Metropolis, *The Beginning of the Monte Carlo method*, Los Alamos Science **Special Issue** (1987).

[48] J. Halton, SIAM Rev. 12. January (1970) p.1-63.

[49] B. Andersson *et al.*, Phys. Rep. **97** (1983) 31.

[50] P. Edén, G. Gustafson, Z. Phys. C **75** (1997) 41; P. Edén, LUTP 96-29 (hep-ph/9610246).

[51] A. Capella *et al.*, Phys. Rep. **236** (1994) 227.

[52] M. Froissart, Phys. Rev. **123** (1961) 1053.

[53] R. Fiore, L. L. Jenkovszky and F. Paccanoni, Acta Physica Hungarica A **9** Number 1 (1999) pp. 5-14.

[54] J. P. Guillaud, A. Sobol, LAPP-EXP 2004-06 July 2004.

[55] T. Sjöstrand, Comp. Phys. Commun. **27** (1982) 243, **28** (1983) 229, **39** (1986) 347; T. Sjöstrand and M. Bengtsson, Comp. Phys. Commun. **43** (1987) 367.

[56] A. Donnachie and P. V. Landshoff, Phys. Lett. **B296** (1992) 227.

[57] G. A. Schuler and T. Sjöstrand, Nucl. Phys. **B407** (1993) 539.

[58] G. A.Schuler and T. Sjöstrand, Phys. Rev. **D49** (1994) 2257.

[59] P. Bruni, A. Edin and G. ungelman, POMPYT version 2.6 - A Monte Carlo to Simulate Diffractive Hard Scattering Processes [ISSN 0418-9833].

[60] S. Navin, *Diffraction in PYTHIA 8*, arXiv:1005.3894v1 [hep-ph], LUTP-09-23, MC-net/10/09.

[61] F. E. Low, Phys. Rev. **D12** (1975) 163;

S. Nussinov, Phys. Rev. Lett **34** (1975) 1286; Phys. Rev. **D14** (1976) 246.

[62] G. Ingelman and P. Schlein, Phys. Lett. **B152** (1985) 256.

[63] V. Gribov and L. Lipatov, J. Nucl. Phys. **15** (1972) 438 [Yad. Fiz. **15** (1972) 781];

V. Gribov and L. Lipatov, J. Nucl. Phys. **15** (1972) 675 [Yad. Fiz. **15** (1972) 1218];

Y. Dokshitzer, Sov. Phys. JETP **46** (1977) 641;

G. Altarelli and G. Parisi, Nucl. Phys. **B126** (1977) 298.

[64] P. Bruni and G. Ingelman, Phys. Lett. **B311** (1993) 317.

[65] E. Berger *et al.*, Nucl. Phys. **B286** (1987) 704.

[66] K. Streng, CERN-TH.4949 (1988).

[67] H. Jung, Comput. Phys. Commun. **86** (1995) 147.

[68] A. Donnachie and P. V. Landshoff, Nucl. Phys. **B244** (1984) 322.

[69] *The Les Houches Accord PDF interface* `http://projects.hepforge.org/lhapdf/pdfsets`.

[70] A. Aktas *et al.* [H1 Collaboration], JHEP 0710 (2007) 042 [arXiv:0708.3217 [hep-ex]].

[71] P. R. Newman *et al.* H1 2006 Diffractive densities: Updates and Practicalities - talk at HERA-LHC workshop 2007, `http://indico.cern.ch/getFile.py/access?contribId=144&sessionId=10&resId=0&materialId=slides&confId=11784`.

[72] T. Sjöstrand, S. Mrenna and P. Skands, Comput. Phys. Comm. **178** (2008) 852.

[73] M. G. Albrow *et al.*, (TeV4LHC QCD working group), arXiv:hep-ph/0610012 (2006), D6T (109) tune.

[74] P. Z. Skands, *Multi-parton interaction workshop* Perugia, Italy Oct 2008, arXiv:0905.3418[hep-ph] (2009) Perugia-0 (320) tune.

[75] Z. L. Matthews, ALICE-INT-2009-027; PhD thesis, in preparation, Birmingham, 2011.

[76] M. Poghosyan, *Diffraction dissociation in proton-proton collisions at $\sqrt{s} = 0.9\,TeV, 2.76\,TeV and 7\,TeV, with ALICE at the LHC.*, Quark Matter 2011, Annecy, France, May 23-28, 2011.

[77] R. E. Ansorge *et al.* [UA5 Collaboration], Z. Phys C **33** (1986) 175.

[78] N. A. Amos *et al.*, Phys. Lett. B **301** (1993) 313.

[79] S. Klimenko, J. Konigsberg, T. M. Liss, Fermilab preprint, Fermilab-FN-0741(2003).

[80] T. Affolder *et al.* [CDF Collaboration], Phys. Rev. Lett. **87** (2001) 141802.

[81] The ATLAS collaboration, ATLAS-CONF-2010-048, July 2010.

[82] S. Navin, *Overview of Diffraction at the LHC*, Conference proceedings ISMD 2010, Antwerp.

[83] K. Pearson, *On the theory of contingency and its relation to association and normal correlation*, Drapers' Co. Memoirs, Biometric Series No. 1, London (1904).

[84] N. D. Gagunashvili, arXiv:physics/0605123, 2006.

[85] H. Cramer, *Mathematical methods of statistics*, Princeton University Press, Princeton (1946).

[86] S. J. Haberman, Biometrics **29** (1973) 205-220.

[87] R. C. Lewton and J. Felenstein, Biometrics **21** (1965) 19-33.